

University of Southampton Research Repository ePrints Soton

Copyright © and Moral Rights for this thesis are retained by the author and/or other copyright owners. A copy can be downloaded for personal non-commercial research or study, without prior permission or charge. This thesis cannot be reproduced or quoted extensively from without first obtaining permission in writing from the copyright holder/s. The content must not be changed in any way or sold commercially in any format or medium without the formal permission of the copyright holders.

When referring to this work, full bibliographic details including the author, title, awarding institution and date of the thesis must be given e.g.

AUTHOR (year of submission) "Full thesis title", University of Southampton, name of the University School or Department, PhD Thesis, pagination

UNIVERSITY OF SOUTHAMPTON

FACULTY OF ENGINEERING AND THE ENVIRONMENT

School of Civil Engineering

**Uncertainty in Terrestrial Laser Scanning for
Measuring Surface Movements
at a Local Scale**

by

Lei Fan

Supervisors:

Professor William Powrie

Dr. Joel Smethurst

Thesis for the degree of Doctor of Philosophy

September 2014

UNIVERSITY OF SOUTHAMPTON

ABSTRACT

FACULTY OF ENGINEERING AND THE ENVIRONMENT

School of Civil Engineering

Thesis for the degree of Doctor of Philosophy

UNCERTAINTY IN TERRESTRIAL LASER SCANNING FOR MEASURING SURFACE MOVEMENTS AT A LOCAL SCALE

Lei Fan

Most railways and roads in the UK are founded on engineered slopes such as embankments and cuttings, or large natural slopes. Slope instability over a considerable part of their length is widely recognised as a threat for railway passengers and road users, and is considered a major hazard by the managing authorities of transport links. Various means can be used to assess slope instability, one of which is to measure slope surface movements.

Terrestrial laser scanning (TLS) is a remote sensing tool that can record a large amount of accurate topographical information with a fine spatial resolution over a short period of time. It has been used increasingly for measuring ground surfaces (i.e. topographical survey) and monitoring surface movements, such as those caused by landslides. However, the capability of this technique in these applications has not been fully explored in the literature, and thus forms the focus of this thesis. A quantitative study has been carried out to investigate the major error sources that affect the accuracy of digital elevation models (DEMs) derived from TLS survey data, and the magnitude of deformation that can be detected by repeated TLS surveys, at a local scale.

In this research, vegetation-induced elevation errors in TLS measurements and the ways in which they can be minimised have been investigated experimentally. The presence of short vegetation was found to be a significant limiting factor for TLS surveys of terrain surfaces, with the average grass-induced elevation error being roughly 65% of the grass height. A finer resolution scan with a lower incidence angle (greater visibility) can effectively reduce vegetation error, as will scanning the same area from multiple scanner locations.

The influence of measurement errors in source data points (or a point cloud) on a triangulated irregular network (TIN) with linear interpolation has been analysed. Based on the law of error

propagation, an analytical solution was derived to calculate the error variance at any location within a TIN model, due to vertical and horizontal errors in source data points. For the special case of equal and independent error variances in source data points, the maximum, average and minimum values of propagated error variance within a TIN were found to be equal to unity, a half and a third respectively of the error variance in source data points.

Errors in DEMs created from the TLS data points representing four terrain surfaces of different characteristics have been quantified using a statistical resampling method. The results show that terrain surface complexity can considerably affect the accuracy of DEMs. The effects of data point density (equivalent point spacing) on the DEM errors have also been analysed. For the data point spacings (35-100 mm) considered in the analyses, the DEM errors increased almost linearly with increasing data point spacing. The results also show that the DEM errors can be decomposed into two parts: a noise-related part and a data-density dependent part.

Repeat TLS surveys of some fixed objects have been carried out, to seek to empirically quantify the georeferencing-induced positional errors involved in repeated TLS surveys. The results indicate that repeated TLS surveys can measure millimetric deformations of smooth surfaces if a high georeferencing accuracy is achieved. The DEM errors, along with the georeferencing-induced positional errors, were used to infer the minimum magnitude of movements that can be measured by multi-temporal TLS surveys of rough terrain surfaces. In the case of the Newbury cutting considered in this study, the minimum level of detection was approximately 20 mm (at a 95% confidence level) for the data point spacing of 35 mm.

The findings in this research can aid in assessing the fitness of TLS surveys of terrain surfaces for a particular project, and thus are of use in the survey planning. The methods presented in this thesis can be applied to analyse errors in DEMs for making more meaningful interpretations of DEMs or surface variations derived from repeated TLS surveys.

Contents

ABSTRACT	i
Contents	iii
List of tables	ix
List of figures	xi
DECLARATION OF AUTHORSHIP	xv
Acknowledgements	xvii
Abbreviations	xix
Chapter 1 : Introduction	1
1.1 Background	1
1.2 Aim and objectives.....	2
1.3 Thesis layout	3
1.4 Terms	4
Chapter 2 : Slope Movement	7
2.1 Introduction.....	7
2.2 Slope stability problems.....	7
2.3 Slope movement.....	9
2.3.1 Pre-failure deformation	9
2.3.2 Post-failure and reactivation deformation	11
2.3.3 Seasonal deformation.....	13
2.4 Slope monitoring.....	14
2.4.1 Geotechnical instruments	14
2.4.2 Engineering surveying	15
2.5 Summary	16
Chapter 3 : Accuracy of Measurement	19
3.1 Introduction.....	19
3.2 TLS systems.....	19
3.3 Factors affecting the accuracy of TLS measurement	21

3.3.1	Instrument errors.....	22
3.3.2	Environment	23
3.3.3	Object surface characteristics	24
3.3.4	Scanning geometry	25
3.3.5	Measurement accuracy reported in the literature.....	25
3.4	Experiments.....	25
3.4.1	Experiment 1: range precision.....	26
3.4.2	Experiment 2: positional accuracy.....	28
3.4.3	Experiment 3: edge effects	35
3.5	Discussion.....	39
3.6	Summary.....	39
Chapter 4	Vegetation Effects	40
4.1	Introduction	40
4.2	Study site and data.....	42
4.2.1	Site.....	42
4.2.2	TLS survey	43
4.2.3	Bare ground survey.....	44
4.2.4	Influence of edge effects.....	44
4.3	Data processing.....	46
4.3.1	Bare ground surface.....	46
4.3.2	Methods to reduce vegetation noise	47
4.3.3	Vegetation surface, height and error.....	49
4.4	Results	50
4.4.1	Total station measurement accuracy.....	50
4.4.2	Registration error.....	51
4.4.3	Vegetation error and factors influencing it.....	51
4.4.4	Other factors affecting vegetation error.....	53
4.4.5	A second experiment	56
4.5	Discussion.....	57

4.6	Summary	58
Chapter 5 : Propagation of Measurement Errors.....		61
5.1	Introduction.....	61
5.2	TIN with linear interpolation	62
5.3	Error propagation	63
5.4	Propagated error variance of source data points	64
5.4.1	Propagation of vertical error	65
5.4.2	Propagation of horizontal error	67
5.5	The parameter M	73
5.6	Validation.....	75
5.6.1	Monte Carlo simulation	75
5.6.2	Experiments	75
5.7	Combination of vertical and horizontal error variance	81
5.8	Discussion	83
5.9	Summary	85
Chapter 6 : DEM Accuracy		87
6.1	Introduction.....	87
6.1.1	Digital elevation models	87
6.1.2	DEM accuracy descriptor.....	89
6.1.3	Knowledge gap	90
6.2	Study data.....	90
6.2.1	An engineered slope.....	90
6.2.2	Other types of surfaces.....	92
6.3	Method	94
6.4	Results.....	98
6.4.1	The engineered slope	98
6.4.2	Other types of surfaces.....	101
6.5	Discussion	102
6.6	Summary	102

Chapter 7 : Georeferencing-induced positional errors and SDM Uncertainty...	105
7.1 Introduction	105
7.2 Multi-temporal TLS surveying	105
7.2.1 Georeferencing	106
7.2.2 Study site	107
7.2.3 Method.....	108
7.2.4 Data processing.....	112
7.2.5 Results	112
7.3 Uncertainty in SDMs for a terrain surface.....	113
7.3.1 Surface deformation models	113
7.3.2 Propagation of DEM errors into SDMs	114
7.4 Discussion.....	115
7.5 Summary.....	116
Chapter 8 : Conclusions.....	117
8.1 Key results	117
8.1.1 Measurement performance of TLS instrument.....	117
8.1.2 Performance of TLS in vegetated surface	117
8.1.3 Accuracy of DEMs	118
8.1.4 Uncertainty in georeferencing	119
8.2 Application of TLS systems to slopes	119
8.2.1 Application to vegetated slopes.....	119
8.2.2 Application to non-vegetated slopes.....	120
8.2.3 Application of TLS systems to other geohazards	121
8.3 Future work.....	121
Appendices.....	123
Appendix 1: Highway earthwork failures during 2000/2001	125
Appendix 2: List of recent railway landslides in press	129
References.....	135
Bibliography	145

Publications.....	147
--------------------------	------------

List of tables

Table 1.1: Measures of bias, precision and accuracy (based on the definitions given in Atkinson and Foody, 2002). Z_{mea} and Z_{ref} represent measured values and reference values for n samples, respectively (the reference number i for each sample is not shown for simplicity); Z_{mea} is the mean of the measured values.....	6
Table 2.1: Risk category of post-failure deformations (HA 48/93, Highways Agency, 1993)....	13
Table 2.2: Deformation behaviour and the possibility of predicting first-failure.	17
Table 3.1: Technical specification for a Leica ScanStation C10 (Leica Geosystems, 2012b).....	26
Table 3.2: The coordinates of the targets (targets 1 – 7: circular targets; targets 8 – 10: square targets) measured by the ScanStation C10 and the total station respectively.	30
Table 3.3: The distances between two successive targets measured by the total station and the ScanStation C10, and their differences.	31
Table 3.4: The horizontal distances between Station A and the targets measured by the total station and the ScanStation C10, and their differences.	32
Table 3.5: The coordinates of the targets measured by the scanner in the total station coordinate system.	34
Table 3.6: The differences between the coordinates measured by the two devices.	34
Table 5.1: Propagated vertical error variance (standard deviation) at geometric centres	79
Table 5.2: Propagated horizontal error variance (standard deviation) at geometric centres	80
Table 6.1: The characteristics of the four surfaces considered.	94
Table 6.2: Data density reduction steps.	97
Table 6.3: The interpolation methods and the associated parameters.....	97
Table 7.1: The apparent movements of the scan objects.	112
Table A1.1: Known cut failures in UK highway network-Area 3 during the winter of 2000/2001 (a summary based on Perry’s survey report, 2001).....	127
Table A1.2: Known embankment failures in UK highway network-Area 3 during the winter of 2000/2001 (a summary based on Perry’s survey report, 2001)	128

List of figures

Figure 2.1: Rainfall and landslide frequency in the UK for 2012 (British Geological Survey, 2013).	8
Figure 2.2: Critical inclinometer element displacements with time for Selborne stability experiment (Cooper et al., 1998).	10
Figure 2.3: Conceptual framework for post-failure deformations.	12
Figure 3.1: The coordinates of a scan point in the scanner coordinate system.	21
Figure 3.2: The precision of range measurements at different distances.	27
Figure 3.3: (a) The point cloud representing the plate placed at a distance of 5.4 m; (b) The precision of range measurements: the bar represents variation of distance measurements from the fitting plane while the curve represents a fitted normal distribution.	27
Figure 3.4: Plan view of the arrangement of Experiment 2 (not to scale).	29
Figure 3.5: Photos of the targets: (a) 6” circular targets used to check the accuracy of ScanStation C10; (b) 3” square targets attached to the wall for georeferencing purpose.	29
Figure 3.6: High resolution scans of Leica HDS circular targets.	30
Figure 3.7: The same point at different coordinate systems.	33
Figure 3.8: Spot sizes at different incidence angles (the two surfaces are at the same distance).	36
Figure 3.9: Reflection of laser signals from discontinuous surfaces and the spot sizes on the front and back surfaces.	36
Figure 3.10: (a) Two white plates separated by a distance of 15 mm; (b) the resulting point cloud.	37
Figure 3.11: Edge effects for larger separations (shown at different scales for different separations)	38
Figure 4.1: (a) Site layout (not to scale) and (b) vegetation features.	42
Figure 4.2: (a) The S1L1 and S1H1 point clouds; (b) bare ground points.	43
Figure 4.3: The scan data of individual grass.	45
Figure 4.4: The bare ground surface elevation above an arbitrary datum-plane.	46
Figure 4.5: The vegetation surface, vegetation height and error.	49
Figure 4.6: (a) The S1H1 point cloud; (b) the post-filtering point cloud (local lowest points) using a 60 mm by 60 mm search window; (c) the lower bound of the vegetation surface created from the local lowest points using natural neighbour interpolation.	50
Figure 4.7: (a) Vegetation height; (b) vegetation error (both derived from the S1H1 point cloud).	52

Figure 4.8: (a) The relation between vegetation height and error shown in Figure 4.7; (b) the variation of the vegetation error with the scan distance for grass of similar height (0.135 m – 0.15 m). 52

Figure 4.9: Elevation differences between the lower bounds for the vegetation surface between: (a) repeat fine-resolution scans (S1H1-S1H2); (b) repeat coarse-resolution scans (S1L1 – S1L2), acquired under the same scan conditions..... 54

Figure 4.10: Difference in the lower bound of vegetation surfaces for coarse- and fine-resolution scans (S1L1 –S1H1). 56

Figure 4.11: Difference in lower bound of vegetation surfaces for fine-resolution scans from different scan stations (S1H1-S2H). 56

Figure 4.12: The relation between vegetation height and error for the second site..... 57

Figure 5.1: TIN model with linear interpolation: survey data points A, B and C are three vertices of a triangle in a TIN model and their coordinates are (x_1, y_1, z_1) , (x_2, y_2, z_2) and (x_3, y_3, z_3) , respectively; Point P is located anywhere within the triangle and its elevation can be calculated by the linear function given in Equation (5.1). 63

Figure 5.2: Elevation error caused by horizontal error of source data points: Points B and C are two terrain surface points to be measured. Assume the measurement of point B is free of error, and the measurement of point C has a horizontal error represented by dotted line CA; Line BC represents the terrain surface without any measurement error (note that modelling error is not considered in this study). Points B and A are actual survey points acquired. Line BA is the actual representation of the terrain surface due to the horizontal measurement error from point C. The rise or fall of point E with respect to point C (the imaginary true terrain point) is equivalent to the rise or fall of point A (the actual survey point) with respect to point D, causing an elevation error (i.e. the elevation difference between line BE and BC). α is the slope angle of line BA and β is the angle of inclination of the terrain surface..... 68

Figure 5.3: A single triangle: (a) a triangle surface created using TIN with linear interpolation based on the three node points; (b) values of m_1 ; (c) The propagated error variance in the case of different error variances at nodes (a one-unit error variance at nodes (1,1,1) and (3,1,3) and a two-unit error variance at node (4,4,4)) ; (d) values of M at different locations. 74

Figure 5.4: (a) TLS data points; (b) histogram of vertical error of TLS data points with normal fit 76

Figure 5.5: (a) The TIN created from the TLS survey data; (b) a fine-resolution raster interpolated linearly from the TIN..... 77

Figure 5.6: Spatial characteristics of propagated vertical error. 78

Figure 5.7: Histogram of propagated vertical error at triangle centroids with normal fit 79

Figure 5.8: (a) experiment layout; (b) spatial characteristics of propagated vertical error; (c) histogram of vertical error of TLS data points with normal fit; (d) histogram of propagated vertical error at triangle centroids with normal fit.	81
Figure 6.1: (a) The point cloud representing the upper part of the Newbury cutting; (b) a visualisation of its surface characteristics.	91
Figure 6.2: (a) The elevation residuals; (b) the histogram of the elevation residuals.	92
Figure 6.3: The point clouds representing: (a) a smooth and flat sandy surface; (b) a part of a rough landslip surface.	93
Figure 6.4: Flowchart of the resampling experiments used to assess DEM accuracy.	96
Figure 6.5: The mean errors for different equivalent point spacings and different interpolation methods.	98
Figure 6.6: The RMSE for various point densities (represented by the number of points per metre square) and different interpolation methods.	99
Figure 6.7: The RMSE for different equivalent data point spacings and different interpolation methods.	99
Figure 6.8: The least-square fit of the RMSE at various point spacings for the TIN model.....	100
Figure 6.9: The RMSE for terrain surfaces of different characteristics (the TIN with linear interpolation was used).	101
Figure 7.1: Photo of the slope and the plates.	108
Figure 7.2: Topologies of survey controls.	109

DECLARATION OF AUTHORSHIP

I, *Lei Fan*, declare that the thesis entitled *Uncertainty in Terrestrial Laser Scanning for Measuring Surface Movements at a Local Scale*, and the work presented in the thesis are both my own, and have been generated by me as the result of my own original research. I confirm that:

- this work was done wholly or mainly while in candidature for a research degree at this University;
- where any part of this thesis has previously been submitted for a degree or any other qualification at this University or any other institution, this has been clearly stated;
- where I have consulted the published work of others, this is always clearly attributed;
- where I have quoted from the work of others, the source is always given. With the exception of such quotations, this thesis is entirely my own work;
- I have acknowledged all main sources of help;
- where the thesis is based on work done by myself jointly with others, I have made clear exactly what was done by others and what I have contributed myself;
- parts of this work have been published as: see the Publications section.

Signed:

Date:

Acknowledgements

There are many individuals who helped me in the past three years. My thank you to everyone and apologies to those I failed to name below.

I wish to thank my primary supervisors Professor William Powrie and Dr. Joel Smethurst for their invaluable feedback, help and encouragement. My deep appreciation goes to Professor Herbert Einstein (MIT) for his supervision and help when I stayed at MIT and his continuous support afterward, and Professor Peter Atkinson for providing constructive feedback and sharing ideas on GIS-related problems. I would also like to thank Professor Trevor Tanton for his useful comments on my nine-month and transfer reports, and the two examiners Professor Jon Mills (Newcastle University) and Dr. Derek Clarke whose comments have led to a great improvement of this thesis.

I am grateful to the Engineering and Physical Sciences Research Council (EPSRC) and the Faculty of Engineering and the Environment for providing funds for the research work and my maintenance.

I would like to thank Liam Riddy and Zhihong Li for their assistance with some of my experiments, Dr. Julian Leyland for useful discussion about laser scanning, Dr. David Brown for advising on total station surveying, Harvey Skinner for providing DGPS training, Aingaa Sellaiya for sharing laser scanning data.

Thank you to my friends Deng Pan, Yue Wu, Lisa Gan, James Rollinson, Lili Yu, He Song, Philip Turner and many others at Southampton. I am grateful to all of you for your help and the amazing experience we shared together.

Finally, I wish to thank my entire family, especially Huxiu Wu, Wei Fan and Yan Tu, for their emotional support and patience. I am forever indebted to you for the sacrifices you made to allow me to complete my PhD degree.

Abbreviations

ALS: Airborne Laser Scanning
DEM: Digital Elevation Model
DEMs: Digital Elevation Models
DGPS: Differential Global Positioning System
FWHH: Full Width Half Height
GIS: Geographic Information System
GPS: Global Positioning System
HDS: High Definition Surveying
ICP: Iterative Closest Point
IDW: Inverse Distance Weighting
LiDAR: Light Detection And Ranging
LPR: Local Polynomial Regression
MA: Moving Average
ME: Mean Error
ppm: parts per million
RMSE: Root Mean Square Error
RTK: Real Time Kinematic
SD: Standard Deviation
SDM: Surface Deformation Model
SDMs: Surface Deformation Models
TIN: Triangulated Irregular Network
TINs: Triangulated Irregular Networks
TLS: Terrestrial Laser Scanning

Chapter 1 :

Introduction

1.1 Background

Most transport links in the UK are supported by or run through large earthworks such as embankments and cuttings. Some were constructed within large natural slopes over some of their length (e.g. Folkestone Warren Railway (Birch and Warren, 2006)). Over the years, there have been numerous recorded incidents of slope instability, causing serviceability problems or ultimate failures (Perry, 1989; Birch and Dewar, 2002; Carder and Barker, 2005; Hughes et al., 2007; Smethurst and Powrie, 2007). The monitoring of these slopes is essential for safety. One of the most effective means to assess the stability of a slope is to measure its displacements over time (e.g. Petley et al., 2002, 2004; Carder and Barker, 2005; Wiczorek and Snyder, 2009), which indicate directly whether the slope is on the move. Various techniques can be used for this purpose, such as inclinometers and extensometers (e.g. Carder and Barker, 2005; Smethurst and Powrie, 2007). These conventional instruments are effective but have several drawbacks. For example, they have to be installed on site intrusively and may be expensive.

Terrestrial laser scanning (TLS) can record a large amount of accurate topographical information with a fine spatial resolution over a short period of time. These characteristics suggest that it has a great deal of potential in detecting surface displacements. For example, several researchers have used this technique for monitoring landslides (Teza et al., 2007; Jaboyedoff et al., 2009; Wang et al., 2011; Barbarella and Fiani, 2013) and earth surface erosion (Rosser et al., 2005; Schürch et al., 2011; Montreuil et al., 2013; Day et al., 2013). In most of these case studies, the surface movements were in the order of hundreds of millimetres or more, well above the level of uncertainty associated with TLS surveying. As a result, the uncertainty was not considered or fully evaluated in deformation analysis. However, there should be a minimum magnitude of deformation that is detectable (i.e. a minimum level of detection) by this technique in these applications, which is not well understood.

Chapter 1. Introduction

In the context of TLS surveys of terrain surfaces, the survey data are essentially a set of topographical data points in some coordinate system and are known as a point cloud. These data points can be used to create a digital terrain surface (known as a digital elevation model (DEM)). For detecting surface movements over time, multi-temporal point clouds representing the same object are required. Although there are point-cloud based methods, the most widely used approach to derive surface deformations consists of two steps: (i) convert survey data points into digital elevation models (DEMs) and (ii) compare two DEMs built from data points acquired at different times to show changes over time. Therefore, to understand the minimum level of detection by TLS, it is essential to have a quantitative insight into errors in DEMs created using TLS data points. In addition to the DEM errors, the minimum level of detection depends on the georeferencing-induced positional errors, which can be minimised by choosing a suitable georeferencing method and implementing it properly.

A sound understanding of errors in DEMs created using TLS data points is beneficial in several respects: (i) it can be used to infer the minimum level of detection, which is useful for determining if TLS surveying is suitable for a given application; (ii) it is essential for making more meaningful interpretations of DEMs and surface changes derived from repeated TLS surveys; (iii) it aids in deciding on more appropriate scan parameters for improving the minimum level of detection.

1.2 Aim and objectives

This research aims to investigate errors in DEMs created using TLS data points, with which to infer the capability of TLS in measuring surface movements at a local scale. The main objectives to achieve these goals are described in the following.

Objective 1: The scanner used in this research is a Leica ScanStation C10. It is appropriate to carry out independent experiments to check its measurement performance against that specified by Leica.

Objective 2: To carry out an empirical experiment to quantify the vegetation-induced elevation error in TLS measurements, and to explore the factors affecting vegetation effects and the ways in which they can be minimised.

Objective 3: To investigate the factors that affect errors in DEMs created using TLS data points, including measurement errors in source data points used to build DEMs, densities of data points, roughness (complexity) of terrain surfaces and digital elevation modelling methods.

Objective 4: To carry out survey experiments to empirically assess the magnitude of the georeferencing-induced positional errors that repeated TLS surveys are likely to cause, and to propose a practical TLS surveying procedure that can increase the chances of achieving a high georeferencing accuracy.

1.3 Thesis layout

Chapter 2: Slope movement

This chapter puts the research in context. The causes of instability of engineered slopes are presented. The characteristics and mechanisms of slope movement at various stages are discussed. Approaches for detecting surface displacements are introduced, along with a brief discussion on their pros and cons.

Chapter 3: Accuracy of measurement

TLS measurement systems are briefly introduced, followed by a discussion on the factors that may affect TLS measurement accuracy. The results of the experiments designed for checking the measurement performance of a Leica ScanStation C10 are reported, and the lessons learnt are discussed. Errors in measurement of the ScanStation C10 at discontinuous edges are also investigated.

Chapter 4: Vegetation effects

The effects of short vegetation (grass) on TLS measurements and the ways of reducing these effects are explored. Experimental data are used to evaluate the magnitude and spatial variation of vegetation-induced elevation error, and to explore the factors influencing it. Its efforts on surface deformation detection are also discussed.

Chapter 5: Propagation of measurement errors

This chapter is focused on how measurement errors in source data points affect the accuracy of DEMs created using a TIN with linear interpolation. Both horizontal and vertical measurement errors in source data points are considered. An analytical method is derived for propagating measurement errors in source data points into any particular location within a TIN. The solution is validated using Monte Carlo simulations and survey data obtained from the ScanStation C10.

Chapter 6: DEM accuracy

Three simple digital elevation modelling methods are introduced. A statistical resampling method is used to quantify the DEM accuracy and the factors affecting it, including characteristics of terrain surfaces, densities of data points and interpolation methods.

Chapter 1. Introduction

Chapter 7: Georeferencing-induced positional errors and SDM uncertainty

This chapter reports the results of four empirical survey experiments carried out to quantify the georeferencing-induced positional errors involved in repeated TLS surveys. The methods to derive a surface deformation model (SDM), and the way in which the DEM errors are propagated into a SDM are introduced. The georeferencing-induced positional errors, along with the DEM errors, are used to discuss the capability of TLS in measuring terrain surface movements.

Chapter 8: Conclusions

Key conclusions are presented and suggestions for further work are made.

1.4 Terms

The use of several of the terms that appear in this thesis is not consistent in the literature. In this section, the meaning of these terms adopted in this thesis is clearly defined.

Uncertainty:

Uncertainty is defined as ‘not known or not known certainly’ in the Oxford English Dictionary. In this thesis, unless clearly specified, uncertainty is synonymous with error. The two terms are treated as being interchangeable.

Error:

An error is defined as the difference between the measured or predicted value and the true value. It is also used loosely for the case where there is an accepted reference value (instead of the true value) usually obtained through another measurement or prediction standard of a higher accuracy, due to the fact that the true value is always unknown in physical measurements.

In the context of surveying observations, there are two types of errors:

- *Systematic errors*: errors that cannot be revealed by repeating the measurements (Taylor, 1982). It is possible to model systematic errors mathematically and therefore correct them. Typical examples of systematic errors in engineering surveying can be found in Schofield and Breach (2007).
- *Random errors*: errors that can be revealed by repeating the measurements (Taylor, 1982). The random error of an individual measurement is unpredictable. However, the

behaviour of a group of random errors can be predicted using a statistical model (e.g. the normal distribution) (Schofield and Breach, 2007)

Blunders are mistakes often resulting from the fatigue or inexperience of surveyors (Schofield and Breach, 2007). As they are often large in magnitude, great care is required to prevent them (Schofield and Breach, 2007). Blunders are sometimes called gross ‘errors’ in engineering survey. However, in scientific measurement, blunders should not be classified as errors (Taylor, 1982; Schofield and Breach, 2007).

The following definitions of bias, precision and accuracy are consistent with those defined in Atkinson and Foody (2002). In Table 1.1, the commonly used quantitative measures of bias, precision and accuracy are given. The root mean square error (RMSE) (if the denominator is taken as $(n - 1)$) is equal to the standard deviation of the error if the mean error is zero.

- *Bias*: the difference between the population mean of measurements or predictions and the true or reference value. Bias is an expectation of systematic under- or overprediction based on statistical models (Atkinson and Foody, 2002). The mean error (ME) is a simple measure of bias and can be either negative or positive (Li, 1988; Atkinson and Foody, 2002; Fisher and Tate, 2006). The larger the ME, the greater the bias.
- *Precision*: a measure of the spread of the measured or predicted values from their mean (i.e. repeatability). A narrow spread means high precision. Precision is characterised by a statistical model fitted to an ensemble of measurements (Atkinson and Foody, 2002). The standard deviation (SD) can be used to quantify precision.
- *Accuracy*: a combination of unbiased (i.e. the opposite of bias) and precision (Atkinson and Foody, 2002). Like precision, accuracy depends on a statistical model and is an expectation of the overall error (Atkinson and Foody, 2002). When reference values are available, the RMSE can be used to estimate the accuracy of measured or predicted values.

Bias	Mean error	$ME = \frac{\sum_{i=1}^n (Z_{\text{mea}} - Z_{\text{ref}})}{n}$	(1.1)
Precision	Standard deviation of measured values	$SD_{\text{measured}} = \sqrt{\frac{\sum_{i=1}^n (Z_{\text{mea}} - \bar{Z}_{\text{mea}})^2}{n - 1}}$	(1.2)
	Standard deviation of error	$SD_{\text{error}} = \sqrt{\frac{\sum_{i=1}^n [(Z_{\text{mea}} - Z_{\text{ref}}) - ME]^2}{n - 1}}$	(1.3)
Accuracy	Root mean square error	$RMSE = \sqrt{\frac{\sum_{i=1}^n (Z_{\text{mea}} - Z_{\text{ref}})^2}{n}}$	(1.4)

Table 1.1: Measures of bias, precision and accuracy (based on the definitions given in Atkinson and Foody, 2002). Z_{mea} and Z_{ref} represent measured values and reference values for n samples, respectively (the reference number i for each sample is not shown for simplicity); \bar{Z}_{mea} is the mean of the measured values.

Chapter 2 :

Slope Movement

2.1 Introduction

Most railways and roads in the UK are founded on engineered slopes such as embankments and cuttings, or large natural slopes. Slope instability over a considerable part of their length is widely recognised as a threat for railway passengers and road users, and is considered a major hazard by the managing authorities of transport links. These slopes need to be monitored and well managed primarily for safety. This chapter aims to place the research in context. The reasons why slope instability remains a problem are presented. Slope movements and signs of slope instability are discussed. The monitoring of slope failure is also discussed.

2.2 Slope stability problems

Most railway embankments in the UK were constructed many decades ago when design standards and construction methods were relatively crude. Some materials would not be acceptable for construction today due to their low strength or stiffness. Weak zones containing failed materials remain in many railway embankments and may cause ongoing movement and damage in the long term. The failure of the high-plasticity clay embankments found in southern England often starts with a softened zone at the toe of the embankment, progresses back through the embankment and eventually reaches the crest (Perry et al., 2009). Old railway cuttings in stiff clay could suffer delayed failure primarily due to slow swelling and pore pressure equilibration and known failures of railway cuttings have been generally deep-seated (Vaughan and Walbancke, 1973; Potts et al., 1997). Although modern highway embankments and cuttings were well designed and properly constructed, degradation of earth structures may happen due to ever-changing external factors, for example, failure of drainage systems, variation of ground water profiles and change in climate, which could eventually lead to slope failure. Like railway cuttings, delayed failure of motorway cuttings in stiff clay may occur in the long term. For clay slopes of high plasticity, seasonal changes in water content can induce a cyclic shrinking and swelling behaviour (Smethurst et al., 2006; Ridley et al., 2004) in the soils near the ground

Chapter 2. Slope Movement

surface. This process may cause the soils to suffer non-recoverable softening, and eventually lead to progressive failures (Kovacevic et al., 2001). Some earthworks are founded on large natural slopes, which may suffer progressive failure and/or have existing weak shear planes, for example, the Jackfield landslide (Skempton, 1964). The performance of these earthworks may also depend on the stability of the associated natural slopes.

It is well known that the failure criterion for soils is shear. The shear strength of soils is mainly provided by friction, which depends on the soil properties and the effective normal stress. If the shear strength is reduced and/or the induced shear stress increases to the instantaneous shear strength, irreversible shear strain is generated. Accumulation of shear strain could eventually lead to slope failure. The shear strength is greatly influenced by pore water pressure, which is why many slope failures occur in wet winters. A list of recorded slope failures in the Area 3 of the UK motorway network during the wet winter 2000/2001 is provided in Appendix 1. Some recent slips along railway corridors are listed in Appendix 2. The incidence of landslides in the UK for 2012 is illustrated in Figure 2.1 (British Geological Survey, 2013). Wet weather in both summer and winter is likely to be a major contributor to the increased incidence of landslides in 2012, which is well above the average between 2006 and 2012.

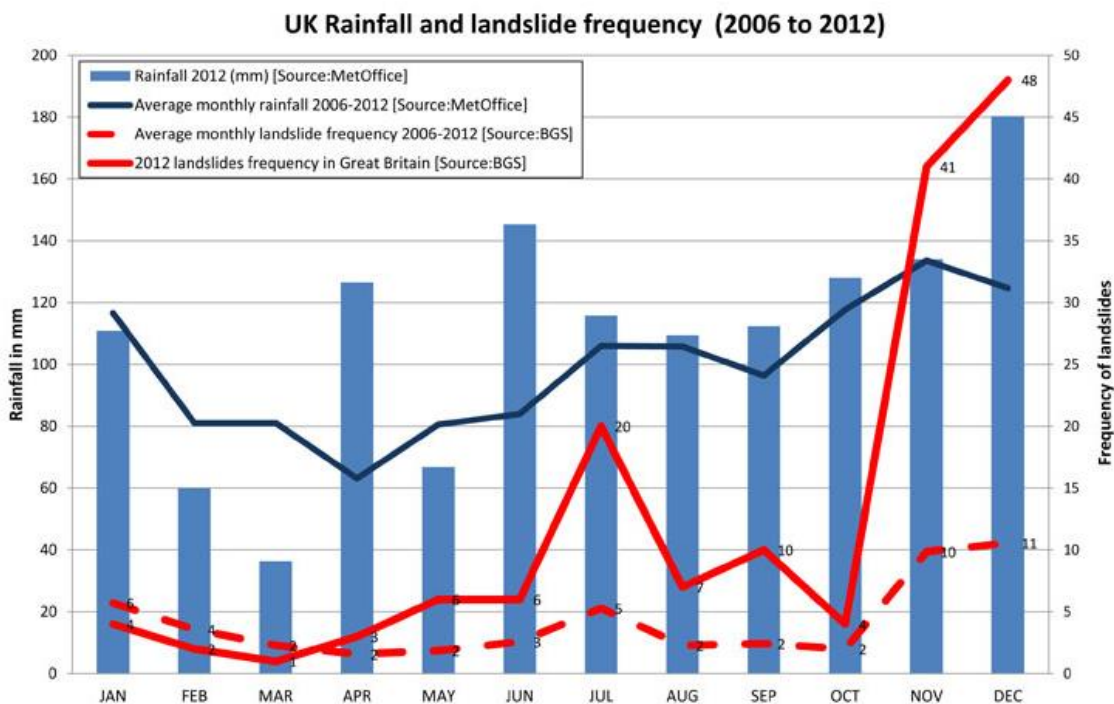


Figure 2.1: Rainfall and landslide frequency in the UK for 2012 (British Geological Survey, 2013).

There have been numerous recorded incidents of slope instability, including some major landslides bringing serious disruption, such as the Flint Hall Farm cut (Davis et al., 2003; Carder and Barker, 2005). Slopes actively on the move also exist, such as Folkestone Warren (Birch and Warren, 2006; Birch and Anderson, 2011). It is now widely accepted that slope instability has become an on-going hazard and a potential source of disruption for some parts of the transport network founded on slopes.

2.3 Slope movement

The most widely used approach to monitor a slope is to measure its displacements, which are essential information for the risk assessment of slope instability. Therefore, an appreciation of slope movement is necessary. Slope movement is a complex result of various parameters acting together, such as slope geometry, geology, soil material properties, pore water pressure and external loads. Since the behaviour of slopes is complex even in the context of relatively homogeneous and continuous materials (Leroueil, 2001), quantitative conclusions about slope movements can be rather difficult to make. Hunter (2003) carried out research on the pre-failure and post-failure deformation behaviour of landslides in cut, fill and natural soil slopes, and considered many recorded landslides and documented case studies. His conclusions about slope deformations are rather qualitative and most are related to the mechanical processes leading to slope failures.

In this section, a qualitative discussion of slope movement is presented. When quantitative data are available in the literature, they are also referred to. Three categories of slope movement are considered. The first two are slope movements at pre-failure stage and after first-failure (including, post-failure and reactivation), while the last is seasonal deformation due to seasonal changes in soil moisture content.

2.3.1 Pre-failure deformation

Leroueil et al. (1996) and Leroueil (2001) defined the pre-failure movement as all the deformation before the formation of a continuous shear surface through the entire soil mass. At pre-failure stage, soils at a local area may reach peak strength before others and hence displacements may be generated locally. The increase of shear strains and displacements in local areas does not necessarily lead to global slope failure. Once the soil has failed in a local zone, the stress will redistribute to the other regions where the mobilised strength is below the critical strength. As a consequence, the stress carried by the soils in the failure zone is reduced and hence the process of deformation may stop. Progressive failure is used to describe the non-uniform mobilisation of shear strength along a potential shear surface, which was recognised a

Chapter 2. Slope Movement

long time ago (Terzaghi and Peck, 1948). The magnitude of pre-failure deformation may vary with the size of a slope.

Few well documented measurement data of pre-failure displacements for engineered slopes can be found in the literature. This is not surprising since a slope that seems stable would usually not be monitored. An exception is the Selborne cut slope stability experiment, in which the cutting was failed deliberately by increasing groundwater level through pore water pressure recharge in the upper aquifer (Cooper et al., 1998). The horizontal movements measured by inclinometers at the shear surface level vary in space. The pre-failure displacement was about 25 mm near the toe and less than 10 mm at other parts of the shear surface (Figure 2.2). It is also interesting to note that the acceleration of deformation occurred within a short period (Figure 2.2) before first-failure. Several researchers (Potts et al., 2000; Ellis and O'Brien, 2007) have also attempted to investigate the deformation behaviour of stiff clay through numerical analysis.

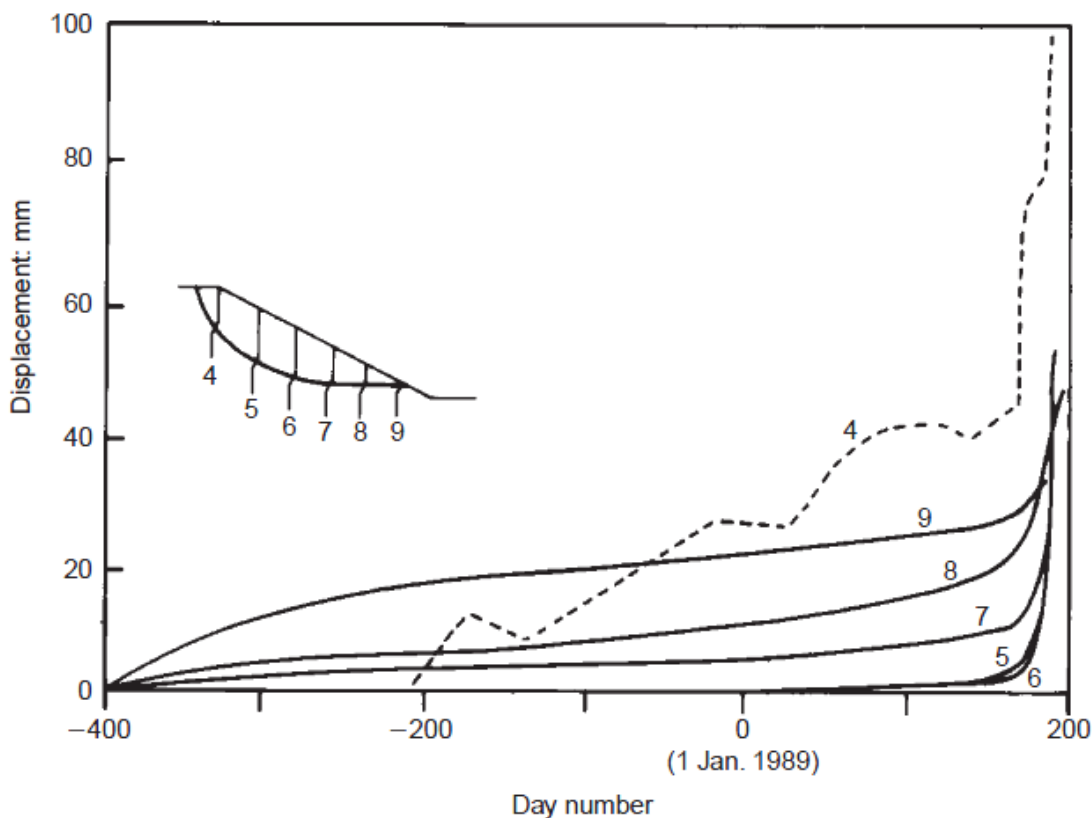


Figure 2.2: Critical inclinometer element displacements with time for Selborne stability experiment (Cooper et al., 1998).

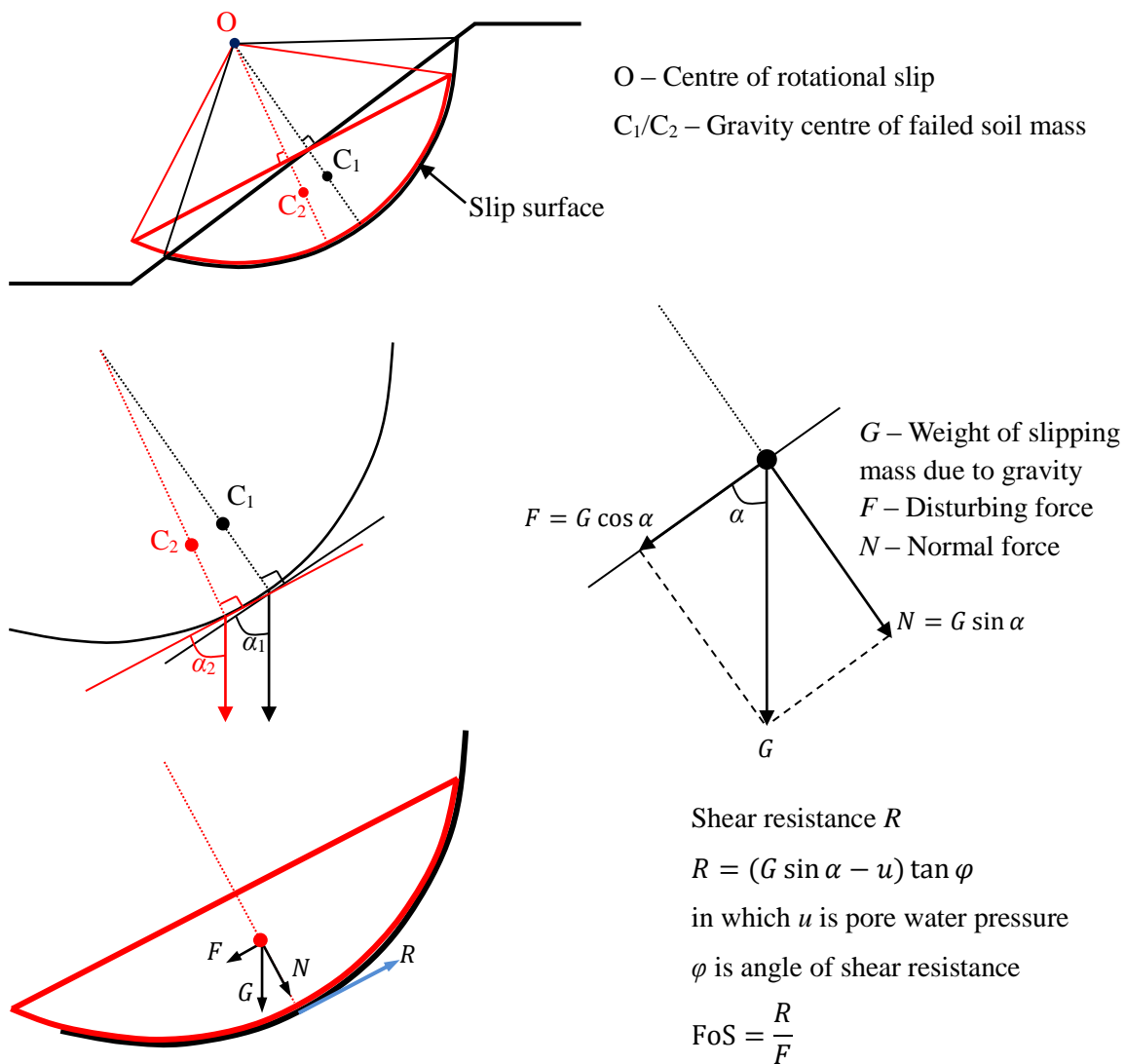
The actual deformation behaviour of slopes often varies from one to the other. For slopes made of brittle soil materials, the pre-failure movement may be very small before sudden collapses.

On the other hand, some slopes may experience continuous movements to a noticeable level before failure. The latter does not necessarily mean gradual failures. This is because slope movement has a time scale in addition to magnitude. Therefore, even if a slope has the potential to deform continuously up to a detectable magnitude before failure, it may still fail suddenly, for example, under abnormal loading conditions. To justify monitoring a slope, it is necessary to know whether the slope is or may be on the move in the first instance. Often, a detailed survey/investigation can be justified only when some information available has suggested that a slope is moving and may become unstable. From the slope monitoring perspective, it is almost impossible to predict the incipient failure of slopes that experience movements of very small magnitude and/or a high deformation rate before first-failure. In these cases, monitoring may not yet have been justified. This is why some landslides occur without any signs of early warning.

For slopes experiencing progressive failure, pre-failure deformation may be relatively large and accumulate over a period of time. For these slopes, there is a chance to predict incipient failure, in particular when the slope exhibits accelerated deformation. A well-understood case of this nature is the delayed collapse of cut slopes in stiff clay, which continue to move for many years due to slow swelling and pore water equilibration. For this particular case, past studies (Cooper et al., 1998; Potts et al., 2000; Ellis et al., 2007) indicate that the toe of a slope usually moves first and suffers the most significant deformation compared with the other parts of the slopes. Several researchers (Saito, 1965; Fukuzono, 1985) attempted to predict slope failures using the creep rupture model (Singh and Mitchell, 1968). However, the successful cases of using this method to predict an actual slope failure are rare. In many cases, this method is used to interpret the temporal pattern of slope deformation after failure.

2.3.2 Post-failure and reactivation deformation

In the post-failure and reactivation stages, a complete shear surface has been formed to make a significant soil mass deform. From the slope monitoring perspective, this stage is very important because the slopes at risk have been identified and are more prone to deform due to reduced strength. A conceptual framework is provided in Figure 2.3. The post-failure movement depends mainly on soil properties and changes in environmental and loading conditions, and its rate can vary significantly. Some slopes move fairly quickly until a stable state is reached while others may experience continuous but slow movements. Leroueil (2001) discussed the movement rates in the post-failure stage from an energy perspective. The rates of movement are determined by the component of potential energy that is not dissipated into friction and disaggregation of the soils.



If the failed soil body moves downward, the angle α will increase (for example, $\alpha_2 > \alpha_1$).

→ Disturbing force (F) will decrease and resisting force (R) may increase.

Therefore, the movement of the soil body will stop at some time.

If F and R (u , φ) change, the balance may be broken and there will be resultant forces (Δf) which will cause the soil body to move further (Occasional reactivation).

Resultant force at time t : $\Delta f_t = F_t - R_t > 0$ (t is time)

Acceleration at time t : $a_t = \frac{\Delta f_t}{m_t}$

Rate of movement at time t : $v_t = v_{t_0} + \int_{t_0}^t a_t dt$

Accumulated movements at time t : $s_t = s_{t_0} + \int_{t_0}^t v_t dt$

Figure 2.3: Conceptual framework for post-failure deformations.

During the post-failure stage, the movement of the landslide body may stop because disturbing force will decrease and become insufficient to move the failed soil body over the slip surface. The pore water pressure may also decrease gradually. As a result, the effective stress increases, and so does the stabilising/resisting force. Subject to further condition changes, occasional reactivation may occur. For example, a reactivation movement of about 200 mm was found within several days of a heavy rainfall at the Flint Hall Farm cut (Davis et al., 2003). Post-failure deformations can be divided into different risk categories based on time to reactivation (Table 2.1).

If a slope is actively on the move after first-failure, continuous monitoring is often required. For example, to monitor the Flint Hall Farm cut after its first failure, post-failure movements were determined by measuring the separation of pairs of wooden pegs at the backscarp and the toe (Davis et al., 2003).

<i>Category</i>	<i>Description</i>	
i	Immediate	Immediate and large movements
ii.1	Weeks	Likely to develop into category i within a few weeks if weather conditions are adverse
ii.2	Months	Likely to be stable for a few weeks but may become unstable within a few months if weather conditions continue to be adverse
ii.3	One year	Tolerable for a year; unlikely to affect third parties
iii	Years	Most unlikely to affect areas outside the slope; will not affect carriageway, services or any property for many years

Table 2.1: Risk category of post-failure deformations (HA 48/93, Highways Agency, 1993).

2.3.3 Seasonal deformation

Clay slopes of high plasticity are vulnerable to seasonal deformation due to seasonal fluctuations in soil moisture content and the associated shrinking and swelling processes (Smethurst et al., 2006, 2012). Evaporation from the clay surface will draw moisture out of the soil profile in the warm summer period, causing shrinkage. Vegetation contributes to the process through transpiration. Evapotranspiration is the sum of soil evaporation and vegetation transpiration, and depends on plant type, climate, soil characteristics and soil water content (Smethurst et al., 2012). During wet winters, the soil swells due to rainfall infiltration. The seasonal variation in soil moisture content may cause up to 50 mm of cyclic movement annually

(Ground Engineering, 1996). The deformation experienced by some high-plasticity clay embankments on the London Underground due to water removal was over 40 mm for a tree-covered clay slope and about 10 mm for a grass-covered slope (Scott et al., 2007). This effect can lead to major serviceability problems, such as excessive vertical displacement of a railway embankment. It could also promote progressive failure of slopes due to cyclic changes in stress (Kovacevic et al., 2001; Take and Bolton, 2011).

2.4 Slope monitoring

In practice, there are various means of monitoring slopes. Visual observation through site visits is a popular method. In fact, almost all condition surveys on Network Rail embankments and cuttings are carried out by trained geotechnical engineers or engineering geologists walking over the earthworks and recording the conditions and any signs of failure. Such signs may include scarp, tension crack, changes in alignment, hummocky ground, toe bulge, subsidence in the upper part of the slope and heave in its lower part, leaning trees and fencing, and damaged or deformed earlier remedial works such as retaining walls.

Another method commonly used is to measure slope surface and/or sub-surface displacements. This approach is normally adopted after the slope shows some signs of instability and is perceived to be at risk of ultimate failure. It is used to check the magnitude of movement and whether there is acceleration. The monitoring results serve as the basis of determining whether strengthening work is required to stop the movement. This approach is effective as it directly suggests whether the slope is moving and how fast. Various methods can be used for this purpose. A crude technique is to install some pegs on slopes and measure the separation of the pegs. Dedicated geotechnical instruments (e.g. inclinometers and extensometers) are widely used for measuring slope movements. Engineering surveying is also a useful means of detecting slope movements.

2.4.1 Geotechnical instruments

Inclinometers are one of most commonly used instruments for measuring slope displacements (e.g. used by Cooper et al., 1998; Carder and Barker, 2005; Smethurst and Powrie, 2007). They can record sub-surface movement and establish changes in displacement by comparison to earlier measurements. The inclinometer casing is either installed in a borehole in the ground or embedded in structural elements, such as piles, diaphragm walls and abutments. The first set of readings is normally used to produce the initial profile of the casing. Subsequent readings are collected and processed regularly to obtain the changes in the casing profile and its rate of change. The advantages of inclinometers include sub-millimetre accuracy, and that the results

are subject to little interference. Once installed, little maintenance is required. Processing the inclinometer measurements is straightforward. However, they have to be installed on site intrusively, which can be time-consuming and expensive. As a result, they are often installed at several specific locations of interest and measure the displacements at only these locations. For some types of inclinometers, a dedicated probe is used to manually record the displacements of the inclinometer tube by a trained geotechnical engineer, which is time consuming. It also means that the temporal resolution of readings is low (typically every few months).

Extensometers, installed in a borehole or along the ground surface, are used to measure the movement between reference points along a single axis. The reference points are normally mechanically linked together using wires, rods or tubes. The displacement is measured using mechanical sensors such as calipers or dial gauges, or electronically using LVDT (linear variable differential transformer) sensors. It can produce accurate measurements and is effective for displacement measurement. However, Cooper et al. (1998) found that wire extensometers were very prone to mechanical disruption although they performed very well over short periods. Hence regular maintenance may be required. Like inclinometers, the installation of extensometers can be time-consuming and expensive. The movements at only several specific locations are measured.

2.4.2 Engineering surveying

A more flexible and cost-effective approach is to carry out engineering surveys. The slope surfaces can be surveyed multiple times and the differences between sequential surveys can be determined. This can be done using a total station or a differential global positioning system (DGPS). Using these devices, however, a surveyor usually has to stay within the slope on the move and travel around for each measurement, which is not ideal from a health and safety perspective. These surveys are generally time-consuming and produce point measurements at a limited number of locations. Also, the data obtained are prone to operator errors.

As an alternative or additional solution, terrestrial laser scanning (TLS) can be considered for monitoring the temporal variation of slope surface. Its main advantages over the geotechnical instruments and the surveying techniques presented above include high speed of measurement, non-contact measurement, survey data of fine details and full coverage of scan scenes. Compared to inclinometers and extensometers, TLS is cost-effective. These advantages suggest that TLS has a great deal of potential in measuring surface movements.

2.5 Summary

Numerous incidents of slope instability suggest that movements and failures of engineered and natural slopes remain a problem and a potential hazard for transport links. To reduce the risk of catastrophic effects caused by slope failures, monitoring plays an important role. One of the most effective means of monitoring slopes is to measure slope deformations. In this chapter, a brief discussion of the common manifestations of slope instability over time has been presented, followed by an exploration of the deformation behaviour of slopes at various stages. The mechanisms of movement were discussed.

The deformation behaviour of slopes is complex, and depends on various factors such as slope geometry, soil material properties, pore water pressure and loads. As a result, common quantitative conclusions about slope movements, in particular at the pre-failure stage, are difficult to make. In general, the pre-failure deformations for many well-constructed earthworks are likely to be small (for example, 20-30 mm for the Selborne cut) and may occur over a relatively long period (for example, several years or longer) before a critical stage is reached. Such small deformations may not give any noticeable signs of potential instability that can be identified to justify a monitoring in practice. Therefore, the prediction of the incipient failure of these engineered slopes, especially from surface movements, remains challenging in practice. Four cases of slope deformation behaviour in the pre-failure stage are summarised in Table 2.2.

For slopes that have already failed, a monitoring plan is justifiable or may be already in place. Some slopes do not suffer an immediate catastrophic failure after first-failure, but experience continuous movement and occasional reactivation. These slopes are more prone to deform due to weak shear planes already formed and the reduced shear resistance. Hence the deformation can be relatively large (for example, 200 mm within several days for the Flint Farm cut), and it is more feasible to monitor the surface movements of these slopes in practice.

Slopes of high plasticity clay may also experience cyclic shrinkage and swell due to seasonal changes in soil water content, which can cause serviceability problems for transport links, and may lead to progressive slope failure.

<i>Pre-failure Deformation</i>	<i>Examples</i>	<i>Prediction of first-failure</i>
Slow and very small for a relatively long period	Sudden failures of slopes of brittle soil materials	Practically impossible
Fast and very small within a very short period	Sudden failures of slopes of brittle soil materials under abnormal loading conditions	Practically impossible
Fast and detectable level within a very short period	Sudden failures due to significant increase of loading and/or decrease of shear resistance	Practically impossible
Slow and detectable level for a relatively long period	Dynamic loading and resistance are well balanced during the deformation process of ductile soil materials, and critical acceleration has not been reached. Movement of stiff clay cut slopes due to slow swelling and the-long-term pore water equilibration	Practically possible

Table 2.2: Deformation behaviour and the possibility of predicting first-failure.

Chapter 3 :

Accuracy of Measurement

3.1 Introduction

This chapter starts with a brief introduction on typical TLS measurement systems in Section 3.2, followed by a discussion on the factors that may affect the accuracy of TLS measurement in Section 3.3. However, a comprehensive review on these is outside the scope of this thesis as its focus is not on the instrument side of TLS. For more detailed information on TLS measurement systems and the factors influencing TLS measurements, readers are referred to Schulz (2007), Reshetyuk (2009) and Beraldin et al. (2010).

Two experiments were carried out to check whether the measurement accuracy of the Leica ScanStation C10 used in this research meets its specification given by Leica. The experimental results are reported in Sections 3.4.1 and 3.4.2, and are used to support the discussions in later parts of this thesis where the scanner measurement accuracy is required. Edge effects occurring at discontinuous edges are investigated in Section 3.4.3, which are essential for understanding vegetation effects detailed in Chapter 4.

3.2 TLS systems

There are three main types of TLS measurement system: time-of-flight (pulsed), phase difference and triangulation. For a time-of-flight scanner, its transmitter sends laser pulses to an object of interest where reflection takes place and a certain amount of energy is backscattered towards the receiving sensors of the scanner. The time delay during this process is used to calculate distance. For phase difference, the magnitude or the frequency of laser beams is modulated (e.g. a sine wave). The emitted laser beam and the received one are compared. The phase difference between their waveforms yields the time delay, which is used to calculate distance. Triangulation exploits the cosine law by constructing a triangle using an illumination direction (angle) aiming at a reflective surface and an observation direction (angle) at a known

Chapter 3: Accuracy of Measurement

baseline from the illumination source. Reshetyuk (2009) and Beraldin et al. (2010) provided a detailed introduction on terrestrial laser scanning measurement systems.

TLS data reported in this thesis were acquired using a time-of-flight or pulsed scanner Leica ScanStation C10. For this type of laser scanners, a distance (r) is obtained by measuring the time interval (t) between transmitted and received signals. The laser travels approximately at the speed of light (c) in air. The range is calculated using Equation (3.1).

$$2r = ct \tag{3.1}$$

An essential part of time-of-flight laser scanners is when their light detector or receiving sensor generates a time-tagged trigger pulse to complete a measurement of time delay. Some typical criteria for this are listed below (Beraldin et al., 2010).

- Peak detection: the maximum amplitude of a returned signal.
- Threshold or leading edge detection: when the rising edge of a return signal exceeds a predefined threshold.
- Constant fraction detection: when a return signal reaches a preset fraction (typically 50%) of its maximum amplitude.

In TLS, scanning an object requires the deflection of laser beams in both the horizontal and the vertical directions. A laser beam deflection unit is used to achieve this, which determines the direction of a scan point with respect to the scanner, i.e. the horizontal and vertical angles. Two common ways of deflecting the laser beams in TLS are summarised below. More information on different deflection systems can be found in Reshetyuk (2009) and Beraldin et al. (2010).

- Beam is deflected horizontally and vertically by two mirrors oscillating about the horizontal and vertical axes of a scanner, respectively. The scanner head remains stationary during the scanning process. The scanners of this nature usually have a limited field of view.
- Beam is deflected vertically by a rotating polygonal mirror, and horizontally by the scanner head rotating in small steps about the scanner standing axis. In this mechanism, the mirror rotates about a horizontal axis to acquire a vertical profile. The scanner head then rotates about the scanner standing axis by a small step, and the next vertical profile is acquired. This process is repeated until the area of interest is scanned. In this way, the

complete object is covered. The scanners utilising this mechanism can have a horizontal field of view of 360° (panoramic).

The coordinates of each scan point is computed using each point's distance and direction relative to the scanner (Figure 3.1). The whole set of scan points acquired forms a point cloud. Based on the geometric relations in Figure 3.1, the formulae (Equation (3.2)) to calculate the coordinates of a scan point can be derived.

$$\begin{aligned}x &= r \cos\theta \cos\varphi \\y &= r \cos\theta \sin\varphi \\z &= r \sin\theta\end{aligned}\tag{3.2}$$

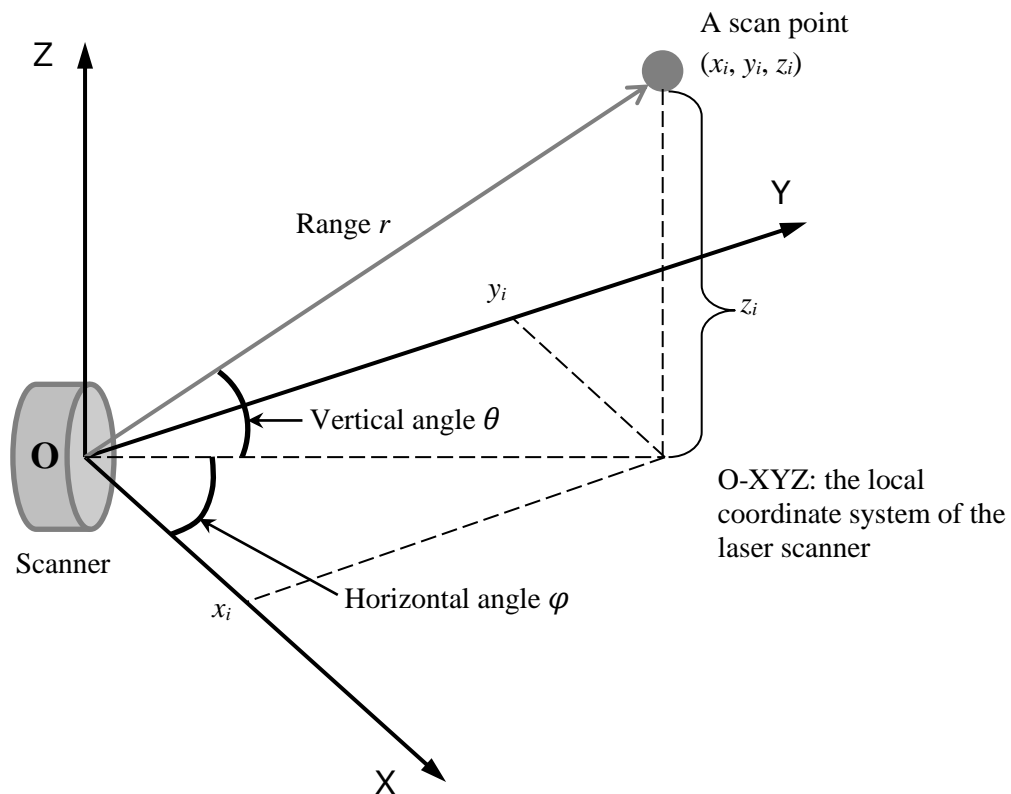


Figure 3.1: The coordinates of a scan point in the scanner coordinate system.

3.3 Factors affecting the accuracy of TLS measurement

Although the TLS measurements are accurate, scan points are subject to measurement errors (Soudarissanane et al., 2011). The coordinates of a scan point are computed using the point's distance and direction relative to the scanner used. Its positional accuracy is influenced mainly

by uncertainties in range and angular measurements. The purpose of this section is briefly to introduce the error sources for individual scan points acquired using a time-of-flight scanner.

3.3.1 Instrument errors

3.3.1.1 *Errors in a laser rangefinder*

For a time-of-flight laser rangefinder, random errors (or precision) in range measurements can be expressed by Equation (3.3) (Beraldin et al., 2010), in which the signal to noise ratio (SNR) depends on: (1) received laser power (affected by transmitted laser power, diameter of the receiver aperture, pulse width, the range to the target and losses) and (2) receiver characteristics (such as detector responsivity at the wavelength to be detected, detectivity, detector size, receiver bandwidth, detector load resistance) (Ready, 1978; Jelalian, 1992; Hebert and Krotkov, 1992; Baltasvias, 1999; Wehr and Lohr, 1999). In addition to random errors, there may be systematic errors in range measurement by a time-of-flight laser rangefinder. Systematic errors can be caused by several factors, such as zero and scale instrumental errors, time walk and range drift. An elaboration on these factors can be found in Reshetyuk (2009). In industry, systematic range errors are sometimes referred to as linearity errors and are specified by some scanner manufacturers.

$$\sigma_r \approx \frac{cT_{\text{rise}}}{2\sqrt{\text{SNR}}} \quad (3.3)$$

where c is the speed of light in air; T_{rise} is the pulse rise time; SNR is the signal to noise ratio.

3.3.1.2 *Errors in the beam deflection unit and angle measurement system*

For most time-of-flight scanners, a laser beam is guided by a beam deflection unit to measure a point (see Section 3.2). This unit, along with an angle measurement system, is used to determine angle measurements. Therefore, the joint performance of these two systems determines the accuracy of angle measurement. The errors in these systems depend on the beam deflection mechanisms, which vary with the types of scanners. In the case of polygonal scanners, the performance of these systems is affected by dynamic track, velocity errors and imbalance of the scanner assembly (Reshetyuk, 2009).

3.3.1.3 *Axes errors*

The inner structures of commercial terrestrial laser scanners are confidential. In terms of their operational principle, they are similar to reflectorless total stations. Therefore, the geometric model of laser scanners is often assumed to be the same as that of total stations (Lichti and

Licht, 2006; Lichti, 2010; Reshetyuk, 2010a). Under this assumption, the following axes can be defined:

- Vertical axis: the axis that allows the rangefinder to move a laser beam horizontally. For a panoramic laser scanner (e.g. ScanStation C10), this is the rotation axis of the scanner head.
- Collimation axis: the axis that passes through the centre of the scanning mirror and the centre of the emitted laser beam (assuming a conical shape beam divergence).
- Horizontal axis: the rotation axis of the scanning mirror

Due to manufacturing imperfection, these axes are not perfectly aligned, which can lead to the following errors (Reshetyuk, 2009):

- Collimation error: angle between the collimation axis and the normal to the horizontal axis, measured in the plane containing the collimation and horizontal axes;
- Horizontal axis error: angle between the horizontal axis and the normal to the vertical axis, measured in the plane containing the horizontal and vertical axes.

The measurement bias of a terrestrial laser scanner largely depends on systematic instrumental errors and axes errors. To remove or minimise them, calibration is required. Sending scanners back to their manufacturers for calibration is probably the most common way for many laser scanner owners. However, in recent years, self-calibration used widely in photogrammetry has been found to be useful for the estimation of systematic errors in terrestrial laser scanners (Reshetyuk, 2010a). In this method, the systematic errors (if any) are treated as unknowns and are included in the calibration model simultaneously with all other system parameters. These unknown systematic errors are then calculated using the data obtained from calibration tests. Researchers (Lichti and Franke, 2005a; Lichti and Licht, 2006; Lichti, 2007, 2008, 2010; Reshetyuk, 2006, 2010a) have reported the successful use of this method to calibrate laser scanners.

3.3.2 Environment

Laser scanning instruments can work properly when the operating temperature is within a certain range. For example, the operating temperature specified for a Leica ScanStation C10 is from 0°C to +40°C (Leica Geosystems, 2012b). It should be noted that the temperature inside the scanner may be higher than the ambient temperature. The variation in temperature during a relatively long scan period may affect the time measurement instrument and hence cause range drift (Reshetyuk, 2009).

Propagating in air, a laser beam can experience attenuation as a result of scattering and absorption (Rüeger, 1996). For a time-of-flight rangefinder, range measurement is affected by the velocity of laser beam propagation in air (Equation (3.1)), which is a function of refractive index of air. The refractive index of air depends on temperature, pressure, relative humidity and CO₂ content (Reshetyuk, 2009), and their effects can be corrected using the method proposed in Ciddor (1996).

TLS users have also noted that dust or rain can influence measurements by reflecting the laser signals back to TLS receivers (Boehler et al., 2003; Reshetyuk, 2009). Although many scanners are advertised as being fully operational between bright sunlight and complete darkness, researchers (Boehler et al., 2003; Pfeifer et al., 2007; Voisin et al., 2007) have reported ambient lighting can affect the accuracy of range measurement. A narrow-band optical interference filter can be used to reduce the amount of interfering radiation (Määttä et al. 1993).

3.3.3 Object surface characteristics

A laser scanner relies on the reflection of its emitted laser signals from a surface to measure the distance. The physical laws of reflection apply. Based on a Lambertian reflectance model, the intensity of a returned laser signal depends on the angle of incidence of the emitted laser beam, backscattering coefficient (reflectance) of the scanned surface and the range to the object surface (Hancock, 1999). As very dark surfaces can absorb most of the visible spectrum, the reflected signal is weak. In this case, the signal to noise ratio is small and thus the accuracy of range measurement may be low. On the other hand, if a surface has very high reflectance, specular reflection is likely to occur. As a result, no data points are recorded or the point being measured is not the one that the laser beam is aiming at.

The reflectivity of an object's surface can affect the power density of returned laser signals and thus the signal to noise ratio. In fact, the range noise is specified for surface materials of various levels of reflectivity by some manufacturers. The effects of the optical properties and the roughness of object surfaces on the accuracy of measurements have been discussed in the literature (Boehler et al., 2003; Pfeifer et al., 2008; Hoefle and Pfeifer, 2007; Kaasalainen et al., 2009).

The temperature of the object surface can also affect range measurements. When the surface of an object is hot, the background radiation by the hot surface reduces the signal to noise ratio and thus the precision of range measurement (Määttä et al. 1993).

3.3.4 Scanning geometry

The positional accuracy of a scan point can be affected by the incidence angle of the laser beam with respect to the object surface. The incidence angle is defined as the angle between a laser beam and the normal vector of the local surface illuminated by the laser beam. According to Lambert's cosine law, an increase in angle of incidence can reduce the intensity of return signals and thus decrease the signal to noise ratio for range measurement. As a result, range measurement noise is likely to increase with increasing incidence angle. This is confirmed by Soudarissanane et al. (2011) who investigated range noise with respect to different incidence angles at various distances. The worst cases considered in their experiment included 50° (incidence angle) at 50 m (scan distance), 60° at 40 m and 70° at 30 m. The range noise for these cases was about 4 mm (1σ).

3.3.5 Measurement accuracy reported in the literature

Over the last decade, researchers have carried out independent evaluations of the performance of terrestrial laser scanners from different manufacturers. A brief summary of key results are presented here.

Boehler et al. (2003) reported that the range accuracy of Leica HDS scanners was better than 3 mm, and discussed a few factors that might influence the scanners' accuracy. Schäfer et al. (2004) investigated the range resolution capability of a Leica HDS2500 and found that the range accuracy was 2.6 mm (at 1σ).

Kersten et al. (2008) investigated the positional accuracy of several scanners. In the tests, Leica scanners (ScanStation 1, ScanStation 2 and HDS6000) and Z+F IMAGER 5006 worked well, with a bias of less than 2 mm and precision of about 4 mm at 1σ . The Faro LS880 and the Trimble GX also achieved good accuracy (3 mm bias and 6 mm precision at 1σ) but a few measurements had relatively large deviations from the mean. The Riegl LMS Z420i had relatively worse performance in terms of bias (7 mm) and precision (6 mm at 1σ). The distance accuracy for all these scanners was found to be better than 6 mm.

3.4 Experiments

As a Leica ScanStation C10 was used in this research, two experiments were carried out to independently check its measurement quality against that specified by Leica. The technical specification of a ScanStation C10 is summarised in Table 3.1 (Leica Geosystems, 2012b). The experiment results support the discussions in later sections where the measurement accuracy of

the ScanStation C10 is concerned. However, a detailed investigation of the instrument accuracy and its calibration is outside the scope of this research. Detailed studies on these aspects can be found in the literature (Reshetyuk, 2009; Lichti, 2007, 2010).

Performance criteria	Performance of ScanStation C10
Operating temperature	0° – 40° C
Field of view	360° (Horizontal) 270° (Vertical)
Maximum range	300m @90% 134m @18%
Scanning speed	Up to 50,000 points/sec
Accuracy of single measurement	Position:4mm (1σ) at 50m Distance:4mm (1σ) at 50m Angle:12" (horizontal and vertical)
Modelled surface precision /noise	2 mm (subject to modelling methodology for modelled surface)
Target acquisition accuracy	2 mm standard deviation
Beam divergence	From 0 to 50m: 4.5mm (FWHH-based) or 7mm (Gaussian-based)
Inclination sensor	Dual axis compensator resolution 1", dynamic range +/- 5', accuracy 1.5"

Table 3.1: Technical specification for a Leica ScanStation C10 (Leica Geosystems, 2012b).

3.4.1 Experiment 1: range precision

In Experiment 1, the scanner was used to scan head-on a vertical white plate of 250 mm by 250 mm, which was attached to a vertical surface of a wooden box fixed on top of a tripod. The tripod was placed sequentially at various distances from the scanner in an outdoor environment. The Southampton weather station recorded the average weather conditions on the day as: temperature 14.5 °C, windspeed 5.1 mph, gustspeed 8.2 mph, barometer 1013.2 mb. Prior to the scans, the scanner was levelled as perfectly as possible using both the external and the electronic levelling. The dual-axis compensator was enabled. The highest scan resolution (horizontal and vertical point spacing at a scan distance of 100 m: 0.02 m × 0.02 m (Leica Geosystem, 2012a)) in the menu of default resolution settings was used to scan the plate.

The point clouds representing the plate were extracted from Leica Cyclone[®] 7.3 and imported into MATLAB[®] (R2012a) where least-squares planes were used to fit the data points. By analysing how far measurement points were away from the fitting plane, the range precision of the scanner was assessed. The results (Figure 3.2) show that the ScanStation C10 had very precise range measurements (approximately 2 mm at 1σ) and exhibited little variation in range precision with the scan distance. The precision was similar to that given in the specification (Table 3.1) of the ScanStation C10. A part of the point cloud representing the plate placed at a distance of 5.4 m is shown in Figure 3.3(a), and the associated analysis results are shown in Figure 3.3(b).

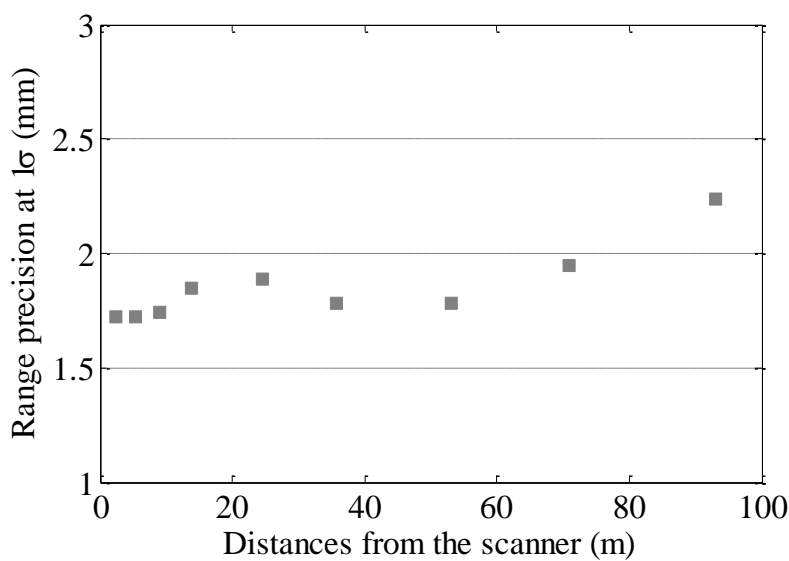


Figure 3.2: The precision of range measurements at different distances.

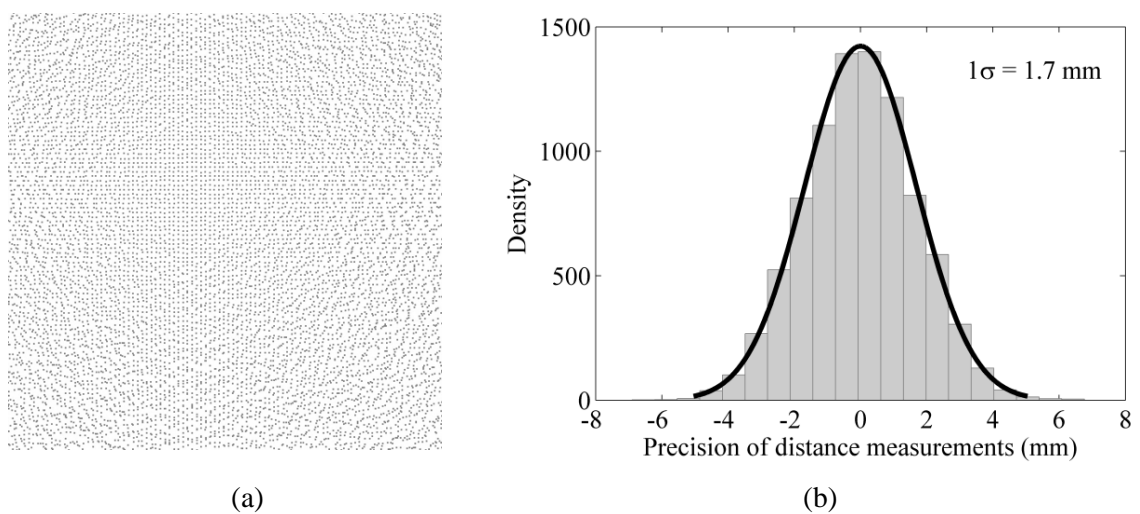


Figure 3.3: (a) The point cloud representing the plate placed at a distance of 5.4 m; (b) The precision of range measurements: the bar represents variation of distance measurements from the fitting plane while the curve represents a fitted normal distribution.

3.4.2 Experiment 2: positional accuracy

Unlike a total station that can be used to measure a particular point repeatedly, the data recording by a ScanStation C10 is automatic. As a result, repeat measurements of the same point would be difficult. In practice, the accuracy of a laser scanner is usually evaluated by measuring dedicated targets. In Experiment 2, a total station was used to produce reference measurements, to which the scanner measurements were compared. The total station used was a Leica FlexLine TS06 hired from SCCS Survey (a UK-based distributor of Leica Geosystems surveying equipment). Its accuracy of distance measurement with and without reflectors was $1.5 \text{ mm} + 2 \text{ ppm}$ and $2 \text{ mm} + 2 \text{ ppm}$, respectively; the accuracy of angle measurement was $5''$. Prior to the delivery, SCCS Survey was asked to check the total station to ensure that its performance met the specification given by Leica.

The layout of Experiment 2 is illustrated in Figure 3.4. The experiment was carried out in an interior space. Seven $6''$ Leica high definition surveying (HDS) circular targets and three $3''$ HDS square targets were used in this experiment. The circular targets were used to investigate the accuracy of the scanner while the square targets were used for transformation of coordinate systems. As the scanner position was reasonably flexible, the scanner was placed at Station A. Two photos showing the circular targets 1-4 and the square targets 8-10 are given in Figure 3.5.

The measurement procedure of Experiment 2 was:

1. The ScanStation C10 was placed on top of the tripod at Station A. The scanner was then levelled and centred to a benchmark point on the floor at Station A. Its dual-axis compensator was enabled.
2. A low resolution scan of the whole interior space of the room was carried out. The low resolution scan data aided in locating the targets for target acquisition scans.
3. High resolution scans of individual targets (circular and square targets) were carried out for deriving the coordinates of their centres.
4. The scanner was removed carefully while the tripod and the tribrach remained at the same location. The total station was then attached to the tribrach, levelled and centred to the same benchmark point on the floor.
5. The total station was used to measure the centres of individual targets to acquire their coordinates. For each target, the measurement was repeated five times.

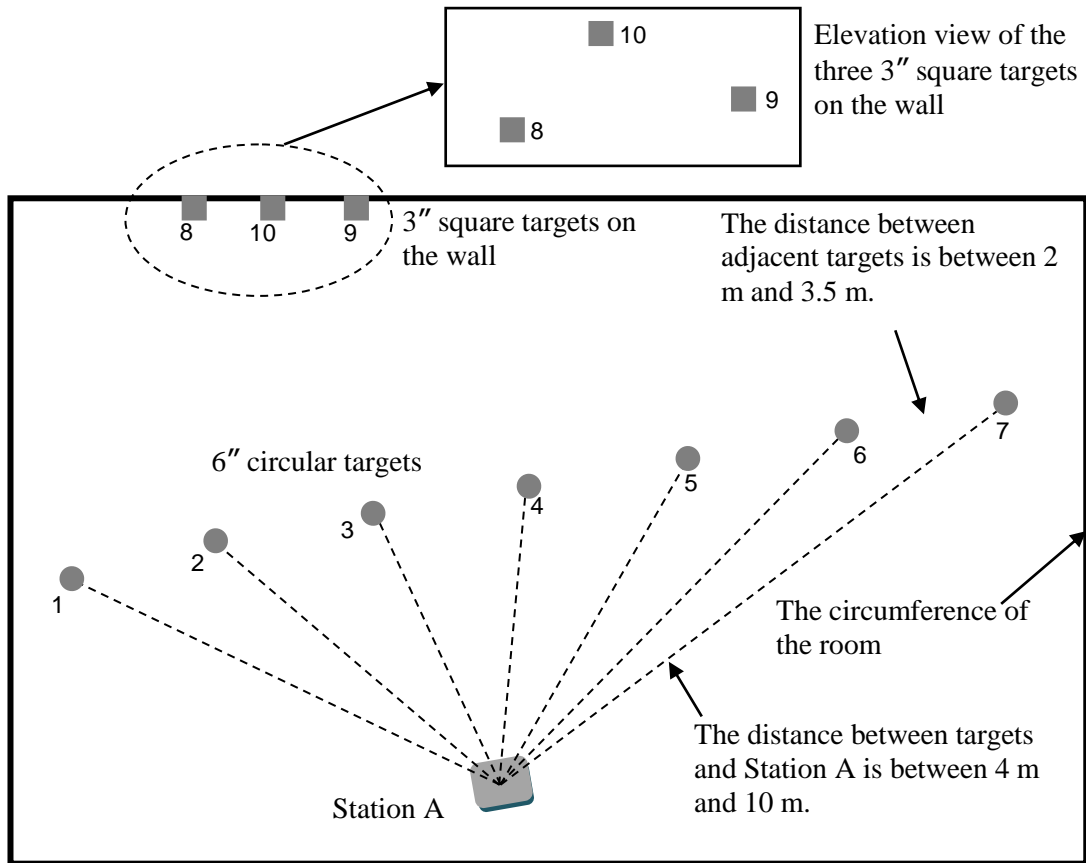


Figure 3.4: Plan view of the arrangement of Experiment 2 (not to scale).

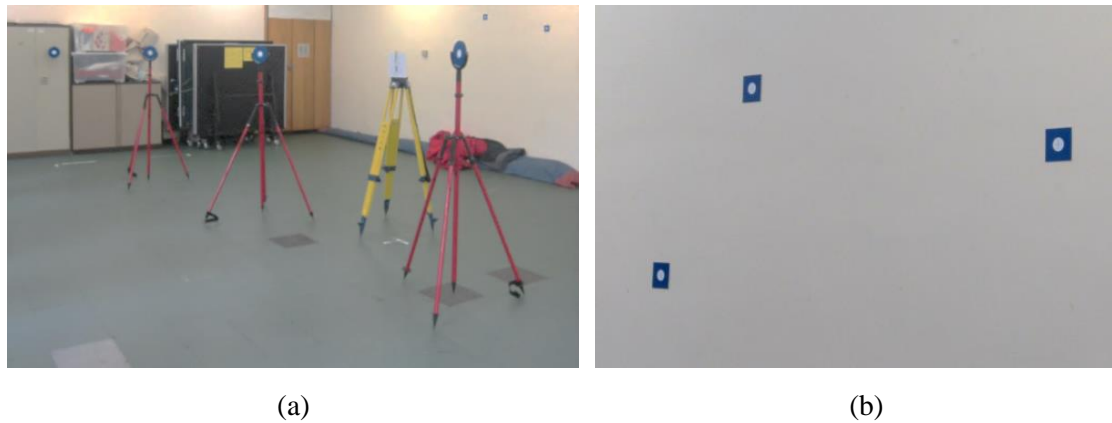


Figure 3.5: Photos of the targets: (a) 6" circular targets used to check the accuracy of ScanStation C10; (b) 3" square targets attached to the wall for georeferencing purpose.

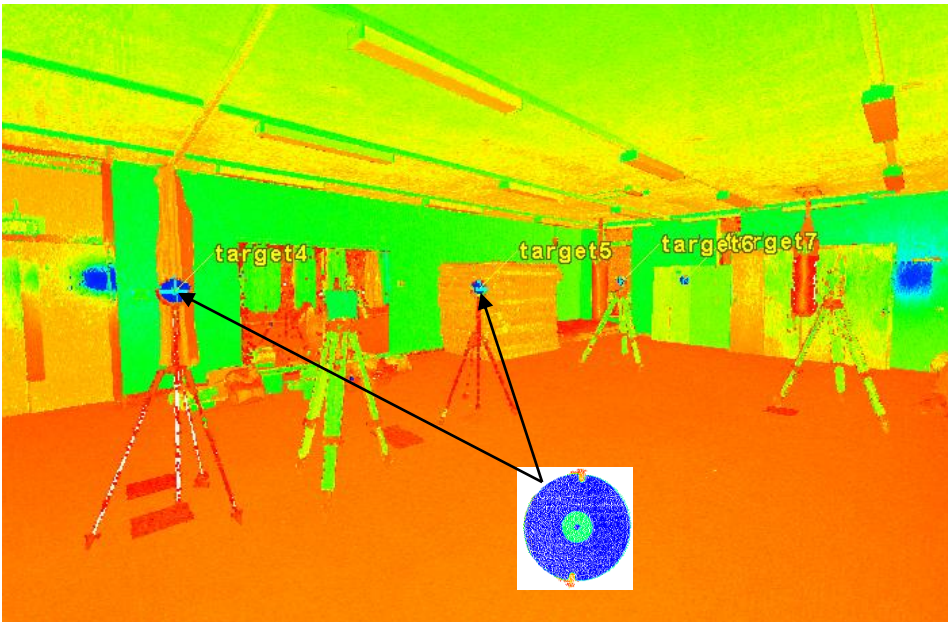


Figure 3.6: High resolution scans of Leica HDS circular targets.

The high resolution scans of the targets are shown in Figure 3.6. The coordinates of each target measured by the two devices are listed in Table 3.2. The coordinates of a target measured by the scanner were different from those of the same target measured by the total station because they were in different coordinate systems.

Targets	Coordinates measured by the ScanStation C10			Coordinates measured by the total station		
	X _{C10} (m)	Y _{C10} (m)	Z _{C10} (m)	X _{TS} (m)	Y _{TS} (m)	Z _{TS} (m)
1	5.190	4.239	-0.102	0.006	6.700	1.494
2	4.506	1.941	-0.098	1.351	4.718	1.497
3	3.867	0.101	-0.101	2.371	3.057	1.495
4	2.676	-2.043	-0.081	3.274	0.777	1.514
5	1.376	-4.443	-0.116	4.309	-1.750	1.480
6	-0.330	-7.392	-0.055	5.510	-4.935	1.541
7	-1.854	-9.975	-0.027	6.545	-7.754	1.568
8	7.784	-0.783	-0.095	5.537	5.530	1.500
9	7.053	-1.960	0.236	5.981	4.215	1.831
10	7.597	-1.082	0.414	5.649	5.195	2.009

Table 3.2: The coordinates of the targets (targets 1 – 7: circular targets; targets 8 – 10: square targets) measured by the ScanStation C10 and the total station respectively.

Prior to comparing the coordinates, it is worth comparing the variables independent of coordinate systems. One of such variables is the distance between the adjacent circular targets, which is determined by their relative positions. As both instruments were levelled and centred to the same benchmark point on the floor, the origins of their coordinate systems matched up in the X and Y directions. Hence the horizontal distance between each target and the benchmark mark is also independent of coordinate systems.

The comparisons about these two variables are provided in Table 3.3 and Table 3.4, showing small differences. The standard deviations of their differences can be calculated using Equation (1.3). These results indicate that the ScanStation C10 had similar measurement performance as the total station.

$$\sigma_L = \pm \sqrt{\frac{\sum_{i=1}^6 (\Delta L_{i,i+1} - \text{ME})^2}{6 - 1}} = 3.1 \text{ mm} \quad (\text{ME} = \frac{1}{6} \sum_{i=1}^6 \Delta L_{i,i+1} = 0.16 \text{ mm})$$

$$\sigma_d = \pm \sqrt{\frac{\sum_{i=1}^7 (\Delta d_{A,i} - \text{ME})^2}{7 - 1}} = 1.6 \text{ mm} \quad (\text{ME} = \frac{1}{7} \sum_{i=1}^7 \Delta d_{A,i} = 0.35 \text{ mm})$$

Two successive targets ($i, i+1$)	Length between two successive targets measured by the total station (m)	Length between two successive targets measured by the ScanStation C10 (m)	Difference in length $\Delta L_{i,i+1}$ (mm)
1 - 2	2.395	2.398	-2.36
2 - 3	1.949	1.948	1.39
3 - 4	2.452	2.453	-0.29
4 - 5	2.731	2.729	1.27
5 - 6	3.403	3.407	-3.93
6 - 7	3.004	2.999	4.86

Table 3.3: The distances between two successive targets measured by the total station and the ScanStation C10, and their differences.

Station A and targets (A, i)	Horizontal distance between targets and Station A measured by the total station (m)	Horizontal distance between targets and Station A measured by the ScanStation C10 (m)	Difference in horizontal distance $\Delta d_{A,i}$ (mm)
A - 1	6.700	6.701	-0.93
A - 2	4.908	4.906	1.59
A - 3	3.869	3.868	0.67
A - 4	3.365	3.367	-1.54
A - 5	4.651	4.651	-0.28
A - 6	7.396	7.399	-3.10
A - 7	10.147	10.146	1.14

Table 3.4: The horizontal distances between Station A and the targets measured by the total station and the ScanStation C10, and their differences.

The following paragraphs describe the process of comparing the coordinates of the 6'' targets measured by the total station and the scanner. To enable the comparison, a coordinate transformation is required, which involves two steps: (1) estimation of the transformation parameters based on control points (square targets) and (2) application of transformation to survey data (circular targets). In the context of TLS surveying, a rigid body transformation (six-parameter transformation) is usually used.

Two sets of coordinates were obtained: the coordinates (X_{TS}, Y_{TS}, Z_{TS}) measured by the total station and those $(X_{C10}, Y_{C10}, Z_{C10})$ determined by the scanner. Equation (3.4) was used to transform the coordinates measured by the ScanStation C10 into the coordinate system of the total station (Figure 3.7).

$$\begin{bmatrix} X \\ Y \\ Z \end{bmatrix} = R(\alpha, \beta, \gamma) \begin{bmatrix} x \\ y \\ z \end{bmatrix} + \begin{bmatrix} \Delta x \\ \Delta y \\ \Delta z \end{bmatrix} \quad (3.4)$$

where (x, y, z) are the coordinates of a point P in the xyz coordinate system; (X, Y, Z) are the coordinates of the same point P in the XYZ coordinate system; $R(\alpha, \beta, \gamma)$ is the rotation matrix and $(\Delta x, \Delta y, \Delta z)$ is the translation vector T .

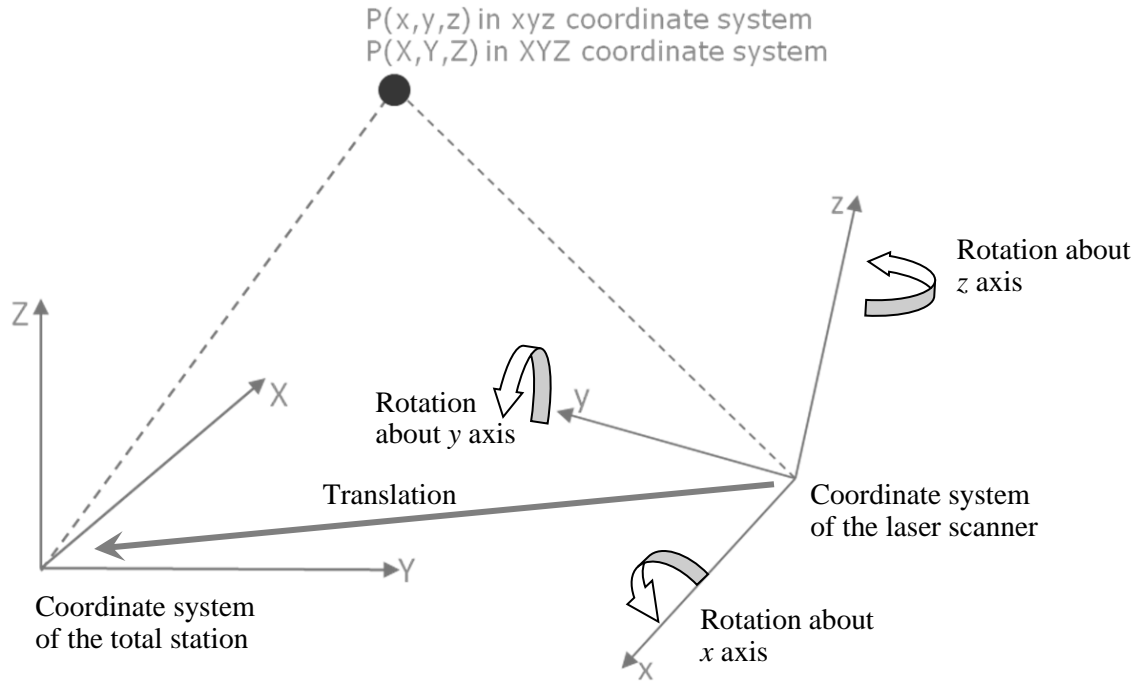


Figure 3.7: The same point at different coordinate systems.

The rotation matrix can be decomposed into three parts, i.e. the rotation about x axis $R_x(\alpha)$, the rotation about y axis $R_y(\beta)$ and the rotation about z axis $R_z(\gamma)$, as shown in Equation (3.5). Note that the rotations given in Equation (3.5) are taken as counterclockwise positive. The least-squares adjustment can be used to find the optimal solutions to the transformation parameters R and T , based on the coordinates of some common points.

$$\begin{aligned}
 R(\alpha, \beta, \gamma) &= R_x(\alpha)R_y(\beta)R_z(\gamma) \\
 &= \begin{bmatrix} 1 & 0 & 0 \\ 0 & \cos \alpha & \sin \alpha \\ 0 & -\sin \alpha & \cos \alpha \end{bmatrix} \begin{bmatrix} \cos \beta & 0 & -\sin \beta \\ 0 & 1 & 0 \\ \sin \beta & 0 & \cos \beta \end{bmatrix} \begin{bmatrix} \cos \gamma & \sin \gamma & 0 \\ -\sin \gamma & \cos \gamma & 0 \\ 0 & 0 & 1 \end{bmatrix} \quad (3.5)
 \end{aligned}$$

In this experiment, the square targets were used to derive the transformation parameters. Once these parameters were obtained, the coordinates (in Table 3.2) of the targets 1-7 measured by the scanner were transformed into the total station coordinate system. The coordinates after the transformation are shown in Table 3.5. The differences between the coordinates of the same targets measured by the two devices are given in Table 3.6.

The results in Table 3.6 show that the ScanStation C10 achieved a high positional accuracy. The largest and mean positional errors were approximately 3 mm and 2 mm, respectively. However, it is important to appreciate that the positional accuracy obtained in this experiment was for the centres of the HDS targets, the coordinates of which are derived from a set of scan points.

Chapter 3: Accuracy of Measurement

Hence the results in Experiments 1 and 2 should be combined to understand the accuracy of individual scan points.

Targets	Coordinates measured by the ScanStation C10 after the transformation into the total station coordinate system		
	X_{C10}^{ts} (m)	Y_{C10}^{ts} (m)	Z_{C10}^{ts} (m)
1	0.006	6.701	1.493
2	1.351	4.716	1.497
3	2.371	3.057	1.494
4	3.276	0.777	1.514
5	4.310	-1.749	1.479
6	5.512	-4.937	1.540
7	6.546	-7.752	1.568

Table 3.5: The coordinates of the targets measured by the scanner in the total station coordinate system.

Targets	The differences in the coordinates measured by the ScanStation C10 and the total station			
	ΔX_{C10-TS} (mm)	ΔY_{C10-TS} (mm)	ΔZ_{C10-TS} (mm)	Mean 3D difference (mm)
1	0	1	-1	1.4
2	0	-2	0	2
3	0	-1	-1	1.4
4	2	0	0	2
5	1	1	-1	1.7
6	2	-2	-1	3
7	1	2	0	2.2

Table 3.6: The differences between the coordinates measured by the two devices.

Some of the experimental steps did not follow best practice in surveying, due to limitation of knowledge at the time the experiments were carried out. These are discussed in the following.

- *Determination of the transformation parameters:* In Experiment 2, only three square control targets were used for estimation of the transformation parameters. This is the

minimum number of targets required for a six-parameter transformation with a marginal redundancy. To increase the possibility of having a higher transformation accuracy, more redundant measurements thus more control targets are required. However, using too many control targets means additional equipment (if a mini-tripod is required for supporting a HDS target) and more workload, which may not be cost-effective in practice. In the context of TLS surveying, using five control targets is likely to be a reasonable trade-off. In Experiment 2, the control targets were arranged close to each other. This can be problematic from a transformation accuracy perspective. In engineering surveying, it is known that the transformation error will increase with distance from the set of control targets. To avoid this extrapolation, the targets should be arranged in such a way that they cover the full volume of a scan scene.

- *Face left and face right observations:* When the total station was used to measure the targets, readings on a single face of the instrument were taken. However, a combination of face left and face right observations can reduce the systematic measurement error caused by non-verticality of the instrument axes (Schofield and Breach, 2007). However, many operations in engineering surveying are carried out on a single face of the instrument, and hence regular checking and calibration are essential (Schofield and Breach, 2007).

Although these best-practice criteria were not met in Experiment 2, the results show very small differences between the measurements by the scanner and those by the total station. Hence Experiment 2 was fit for its purpose. The likely reasons for these results are: (1) the instruments (the scanner and the total station) used were accurate; (2) the dual-axis compensators of both instruments were enabled during the measuring processes, which provided additional constraints to enhance the transformation accuracy; (3) there were no blunders as the experiment was implemented properly and carefully.

3.4.3 Experiment 3: edge effects

The positional accuracy of a scan point may be affected by edge effects. As beams emitted by laser scanners have a small amount of divergence, the laser beam hits a surface across a footprint rather than at a point. This footprint is sometimes referred to as spot size. There are currently two definitions of spot size in industry (Jacobs, 2006). The first type of definition is based on a model of Gaussian distribution of the beam's intensity across its diameter. In this case, the spot size is defined as the diameter of the beam where its intensity is 13.5% of the

maximum intensity at the centre of the beam. The other type is based on the full width half height (FWHH), which is the width of the beam at the half-intensity points (Jacobs, 2006).

When a vertical surface is scanned head-on, the spot size for a ScanStation C10 is 4.5 mm (FWHH-based) or 7 mm (Gaussian-based) at a distance of 50 m (Leica Geosystems, 2012b). The spot size also depends on the angle of incidence of the beam relative to the normal to the surface being illuminated (Soudarissanane et al., 2011). The greater the incidence angle, the larger the spot size (Figure 3.8).

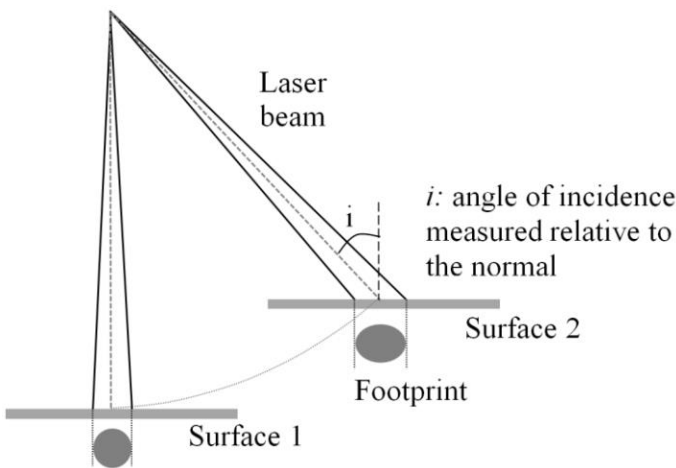


Figure 3.8: Spot sizes at different incidence angles (the two surfaces are at the same distance).

At discontinuous edges, the footprint is divided into parts and multi-returns may be received by the scanner. In Figure 3.9, for example, the laser beam is divided into two parts. The first part is reflected by the front surface while the second part continues to travel and is then reflected by the second surface. Several researchers (Boehler et al., 2003; Tang et al., 2009; Centeno et al., 2010) have investigated edge effects or the spot size of laser beams for a few scanners.

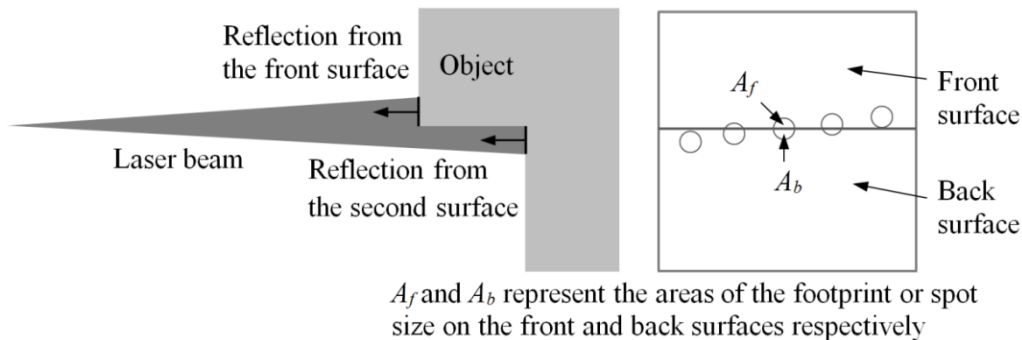


Figure 3.9: Reflection of laser signals from discontinuous surfaces and the spot sizes on the front and back surfaces.

To understand how the ScanStation C10 calculates the distance when edge effects occur, a simple experiment was carried out, in which two white plates at a distance of 5 m from the scanner were scanned head on. The white plates were separated by a 15 mm thick wooden box (Figure 3.10(a)). The point cloud obtained is shown in Figure 3.10(b), which illustrates a transition zone at the discontinuous edges, containing a trail of points. These point locations in the transition zone do not exist on the real surface.

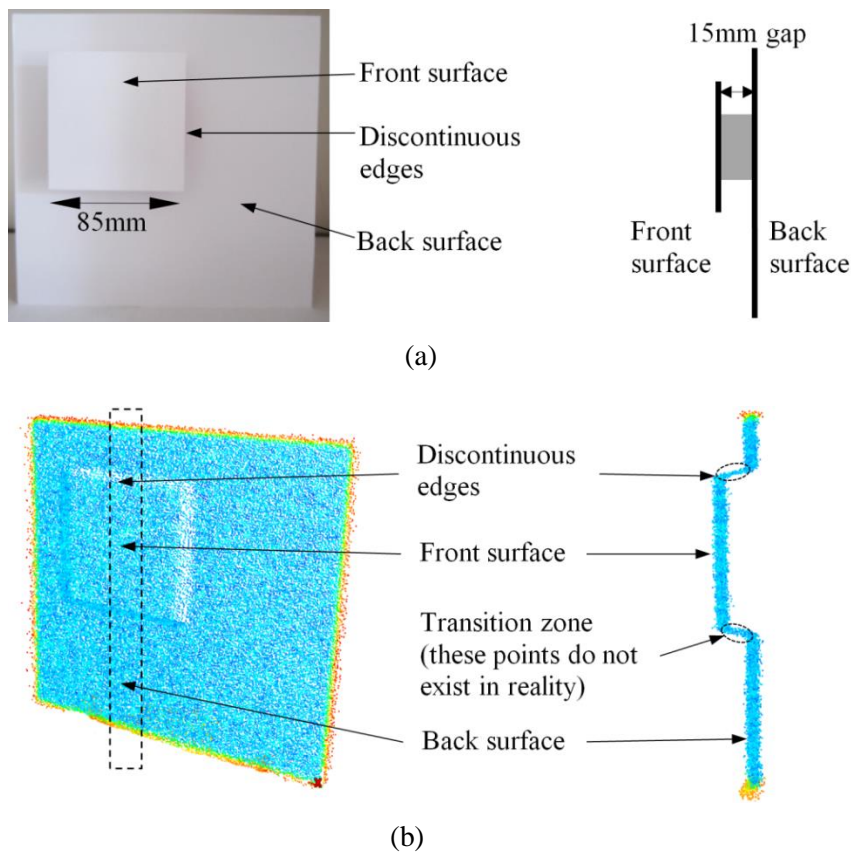


Figure 3.10: (a) Two white plates separated by a distance of 15 mm; (b) the resulting point cloud.

The continuous transition zone suggests that the ScanStation C10 is likely to calculate distances based on the weighted average of the distances of the two surfaces from the scanner, with the weight likely depending on the size of the footprint on each surface. A larger spot size on the front surface and a smaller one on the back surface resulted in a data point that was closer to the front surface. In this case, the surface material of the front and back surfaces were the same and hence the surface reflectance was the same. If the reflectivity were different, the distance calculated by the scanner might also depend on the surface reflectance. In other words, the size of the footprint on each surface and their reflectance may combine to determine the weights used for the range calculation in the transition zone.

Chapter 3: Accuracy of Measurement

In the first experiment, the separation between the two surfaces was small (15 mm). To determine how edge effects change when the separation of the two discontinuous surfaces increases, a second experiment was carried out. In this second experiment, the front surface was fixed in place while the back surface was moved away from the front one in steps of 50 mm. The results in Figure 3.11 (only key separations are given) show that edge effects were still apparent when the separation was increased to 150 mm. However, when the separation was increased to 250 mm the artificial points existed only in a proportion of the transition zone close to the front surface. The proportion decreased with increasing separations between the two surfaces. At a separation of 900 mm, the edge effects had effectively vanished although a few scattered noisy points close to the edge of the front surface were observed. The variation of the length of edge effects with the separation between the two surfaces is also summarised in Figure 3.11.

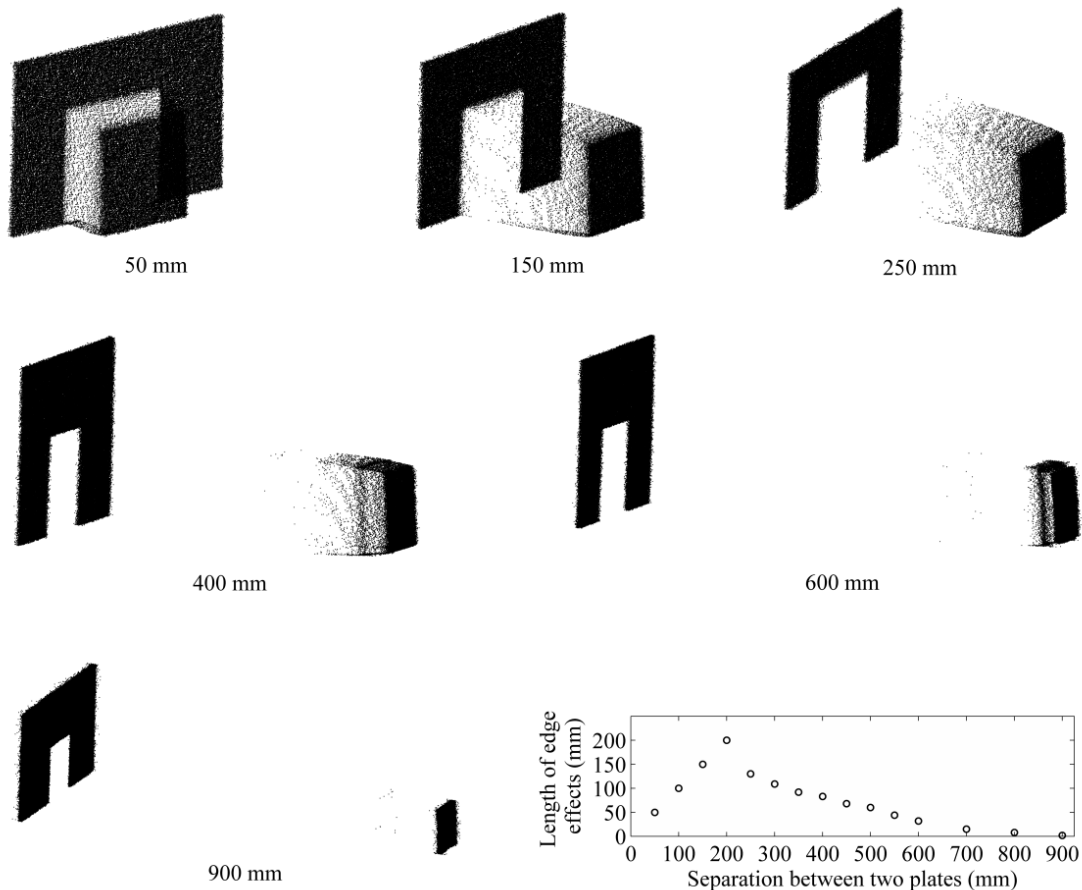


Figure 3.11: Edge effects for larger separations (shown at different scales for different separations)

3.5 Discussion

The results obtained from the experiments in Section 3.4 suggest that the ScanStation C10 can achieve high range precision (2 mm at 1σ) and positional accuracy (2 mm on average) at the given experimental conditions. However, a white paper plate (high reflectivity) and several Leica HDS targets were used in the experiments. The positional errors in individual scan points obtained from a TLS survey of a terrain surface (e.g. an engineered slope) may be larger than those reported in this chapter. This is partly because angle of incidence and surface reflectivity can also influence the positional accuracy of scan points. In addition, a terrain surface is likely to have surface roughness of various scales. As a remote sensing instrument always has a spatial resolution limit, the surface variation within this limit cannot be detailed. In the context of terrestrial laser scanning, the spatial variation within a laser beam footprint is not detectable. Based on the edge effects discussed in Section 3.4.3, the ScanStation C10 used the signals reflected by multiple surfaces for calculating distance (thus coordinates). This may cause an additional positional uncertainty. However, it is difficult to quantify it through experiments. Because of the small footprint of a laser beam at a short range (< 50 m), it may be reasonable to assume that the positional error due to the footprint-scale surface variation is not significant for data points within a short range. To accommodate these additional uncertainties from an engineering perspective, a weight may be applied to the positional error quantified at ideal test conditions.

3.6 Summary

This chapter briefly introduced TLS measurement systems and discussed the factors that may affect the accuracy of TLS measurements. The literature reviewed suggests that many laser scanners are accurate instruments. The performance of a Leica ScanStation C10 was checked against its specification through two experiments. The mean positional error was roughly 2 mm, which was smaller than that specified by Leica. Edge effects were investigated experimentally, which resulted in a trail of data points in the empty space between the two discontinuous surfaces. The length of edge effects depended on the separation between the two discontinuous surfaces.

Chapter 4 :

Vegetation Effects

4.1 Introduction

Recent years have witnessed the increasing use of terrestrial laser scanning (TLS) for various applications, such as topographical survey (Gallay et al., 2013), geology (Buckley et al., 2008) and surface deformation monitoring (Vežočník et al., 2009; Schürch et al., 2011). However, the use of TLS for some applications may be limited by specific environmental factors, such as the presence of vegetation. Laser scanning techniques (in particular Airborne Laser Scanning (ALS)) have been used to capture the characteristics of vegetation such as its structure, height, density and canopy (Lim et al., 2003; Hall et al., 2005; Webster and Kroll, 2006). It is widely recognized that the low oblique angle of transmitted signals from TLS means that it is much more prone to occlusion by vegetation and other objects (such as fencing), which can obstruct TLS signals, than ALS. In vegetated areas, TLS signals may be reflected back to the instrument by vegetation. It is unknown how significantly vegetation affects TLS measurements and the surface changes derived from repeated TLS surveys.

Several researchers (Pfeifer et al., 2001, 2003, 2004; Töyrä et al., 2003; Hodgson and Bresnahan, 2004; Hopkinson et al., 2005) have attempted to evaluate the vegetation-induced errors associated with ALS. Hopkinson et al. (2005) used data from a Boreal wetland environment to estimate land cover (or vegetation class) dependent elevation errors. Real-time DGPS was used to provide reference elevation data for comparison with ALS data. Pfeifer et al. (2004) discussed the influence of vegetation on ALS elevation data and possible corrective approaches.

Few studies have been carried out to investigate the effects of vegetation on TLS surveys. Coveney and Fotheringham (2011) attempted to quantify the vegetation-induced elevation error for an open, large and relatively flat coastal saltmarsh area, fully covered by dense and short vegetation. They found that the elevation error caused solely by vegetation was about five times the arithmetic sum of all other survey-related errors (assuming none of these offset each other).

Guarnieri et al. (2009) carried out research into the retrieval of small-relief marsh morphology from TLS, and found that the vegetation-induced error was in the order of a few centimetres. Day et al. (2013) investigated the use of TLS for measuring bluff erosion and discussed the effect of ground vegetation in this application. These studies were based on relatively large areas and investigated the overall vegetation-induced error.

When TLS is employed to survey a large area, the final survey data are essentially a combination of many sub-scans. In general, TLS is more commonly used to survey or monitor a local and relatively small area (e.g. a slope) because many terrestrial laser scanners have a relatively short useful scan range. Therefore, it is appropriate to carry out a more detailed investigation of the elevation error caused by ground vegetation and its spatial pattern at a local scale, and the associated contributing factors.

Previous research has often focused on the assessment of vegetation-induced elevation error in data acquired from a single survey campaign. For deformation detection over a period of time, multi-temporal data are required. As vegetation-induced error exists in each set of successive survey data, comparison between two sequential datasets may cancel out a proportion of it, resulting in a reduced elevation error. The extent of this reduction is not well understood.

The aim of this chapter is to investigate the effect of short ground vegetation on elevation data from TLS surveys. Several parameters that might affect the vegetation-induced error were investigated, including edge effects, vegetation height, scan resolution, incidence angle and scan distance. The effects of vegetation on the surface deformations derived from repeated TLS surveys are also discussed. The scanner used was a single-return Leica ScanStation C10. The research was undertaken in the context of a local vegetated area.

The vegetation investigated in this chapter is grass, which is one of the most common covers for many engineered slopes. However, very long grass is not investigated as it can result in very large elevation error if the bare ground is the desired information to acquire. In this case, TLS would not fit for purpose. Other tall vegetation such as trees is also not considered for the following reasons. If a dense population of tall vegetation is present, it would be impractical to use TLS to survey the ground surface simply because there are too many obstructions in the scene. If tall vegetation is sparse, obstructions can be overcome by increasing the number of scanner positions.

4.2 Study site and data

4.2.1 Site

For ease of access and mobility, a fairly large area of grass was selected for the experiment, located on the campus of the University of Southampton. The characteristics of the grass were similar to those on some engineered slopes in the UK. The site layout and the detail of the grass are shown in Figure 4.1. The site could be considered to be like a lawn. The grass was green, quite dense and upright, and had moderate tolerance for foot traffic. It was mown regularly, and at the time the experiment was carried out its height generally varied from 70 mm to 140 mm although some individual grass leaves were shorter than 70 mm or longer than 140 mm locally.

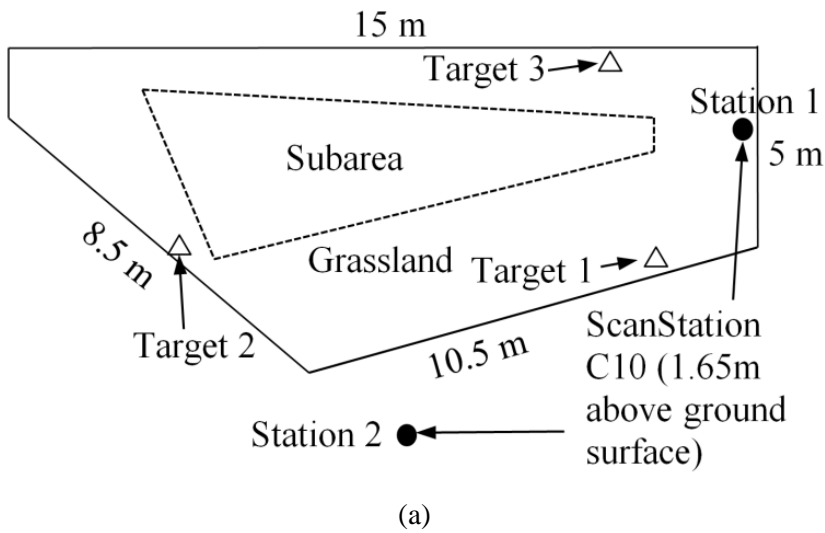


Figure 4.1: (a) Site layout (not to scale) and (b) vegetation features.

4.2.2 TLS survey

The area was scanned using the Leica ScanStation C10 from two different stations (Stations 1 and 2). Three Leica targets were placed in the area to enable registration of the survey data. The scanner was first placed at Station 1 from where the whole grass area was scanned with a coarse spatial resolution (Figure 4.2(a)). Three further scans were then carried out for the subarea with scan resolutions fine, coarse and fine. During this process, the scanner stayed at the same location (Station 1) and height, and in the same orientation. All the resolutions used in this study referred to a scan distance of 100 m. They are defined by Leica and are available in the scan menu (horizontal and vertical spacing at 100 m: $0.2 \text{ m} \times 0.2 \text{ m}$ for low (coarse) resolution; $0.05 \text{ m} \times 0.05 \text{ m}$ for high (fine) resolution) (Leica Geosystems, 2012a). Once the surveys from Station 1 had been completed, the scanner was moved to Station 2 from where the whole area was scanned with coarse and fine scan resolutions. The Leica targets remained in place for data registration and were scanned from both stations.

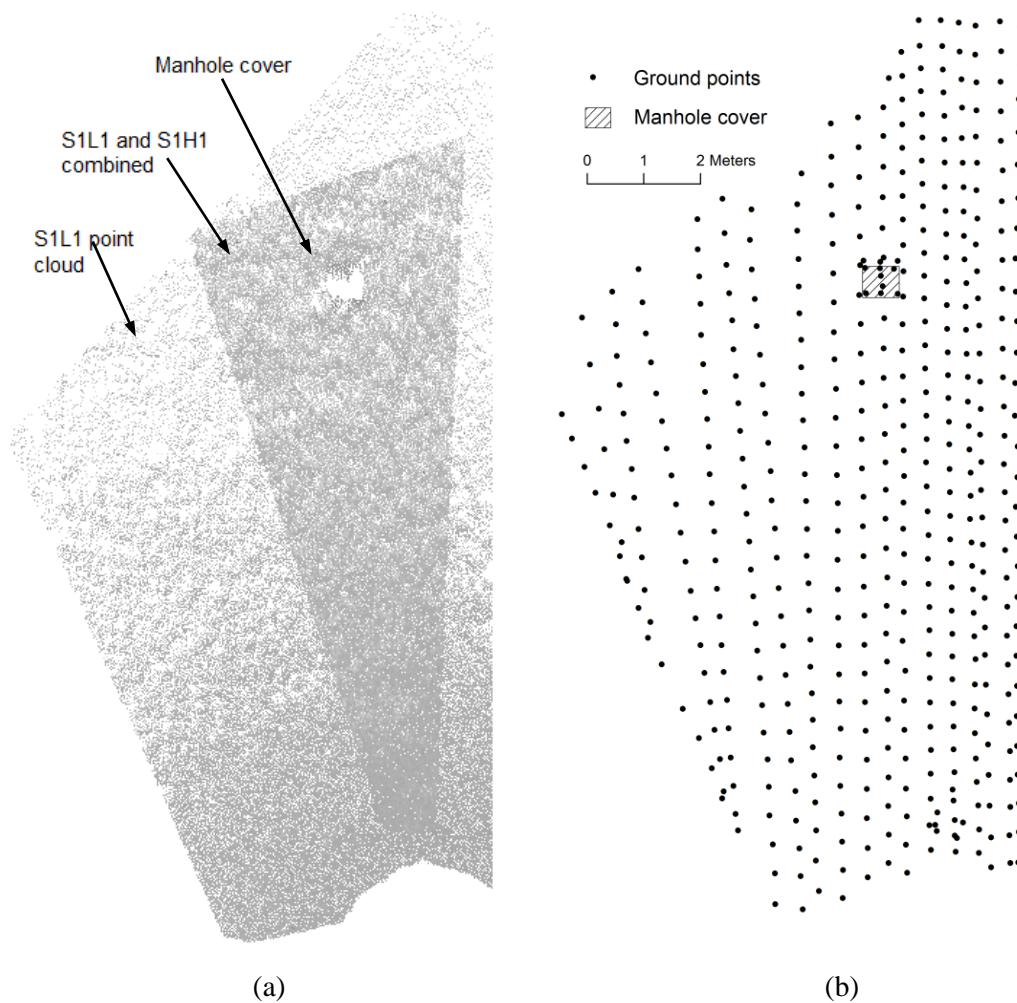


Figure 4.2: (a) The S1L1 and S1H1 point clouds; (b) bare ground points.

Chapter 4. Vegetation Effects

The point clouds acquired in sequence and the associated abbreviations are listed in the following:

- S1L1: The first coarse(low)-resolution scan from Station 1 (the whole area)
- S1H1: The first fine(high)-resolution scan from Station 1 (the sub-area only)
- S1L2: The second coarse(low)-resolution scan from Station 1 (the sub-area only)
- S1H2: The second fine(high)-resolution scan from Station 1 (the sub-area only)
- S2L: The coarse(low)-resolution scan from Station 2 (the whole area)
- S2H: The fine(high)-resolution scan from Station 2 (the sub-area only)

4.2.3 Bare ground survey

A Leica FlexLine TS09 total station (angle measurement accuracy: 1"; accuracy of distance measurement with and without reflector: 1 mm + 1.5 ppm and 2 mm + 2 ppm, respectively) hired from SCCS Survey was used to establish the bare ground surface, measuring a reflective target attached to a pole. The height of the target was known. The pole was held vertically with the aid of a mini-tripod equipped with a bubble level. Care was also taken to ensure that the bottom of the pole just touched the bare ground surface. The Leica targets placed for survey data registration were measured first. This enabled the point clouds to be transformed into the coordinate system of the total station. The target on the vertical pole followed approximately a regular grid and 481 ground points were measured (Figure 4.2(b)).

An existing manhole cover (shown in Figure 4.2(a)) was also surveyed with the scanner and the total station. The survey data associated with this manhole cover were later used to show that the errors from other sources were minimal.

4.2.4 Influence of edge effects

The top surface of vegetated ground is not continuous as gaps are present between individual grass leaves. When a laser beam hits grass, it may be reflected by a grass leaf if the width of an individual leaf is larger than the spot size of the laser beam. Equally, it may interact with the edges of grass leaves, in which case edge effects (investigated in Section 3.4.3) occur. Since the width of an individual grass leaf is usually small, edge effects are likely to occur frequently in a scan of a grass-vegetated area. If a laser beam hits the edge of a grass leaf, a proportion of it may continue to travel to another surface, which could be another leaf or the bare ground surface. The footprint of the remaining signal on the subsequent surface is normally further from the scanner and at a different elevation from that on the surface edge illuminated first. This

implies that many of the data points in a point cloud do not represent the actual positions of grass but lie somewhere between two or several grass leaves (or between grass leaves and the bare ground) that interact with a single laser beam.

To confirm the edge effects for grass leaves, a simple experiment was carried out. An individual grass leaf was positioned 10 mm in front of a plate and then was scanned head on using the ScanStation C10. The scan data are shown in Figure 4.3, and the 10 mm gap between the grass leaf and the plate does not show in the point cloud.

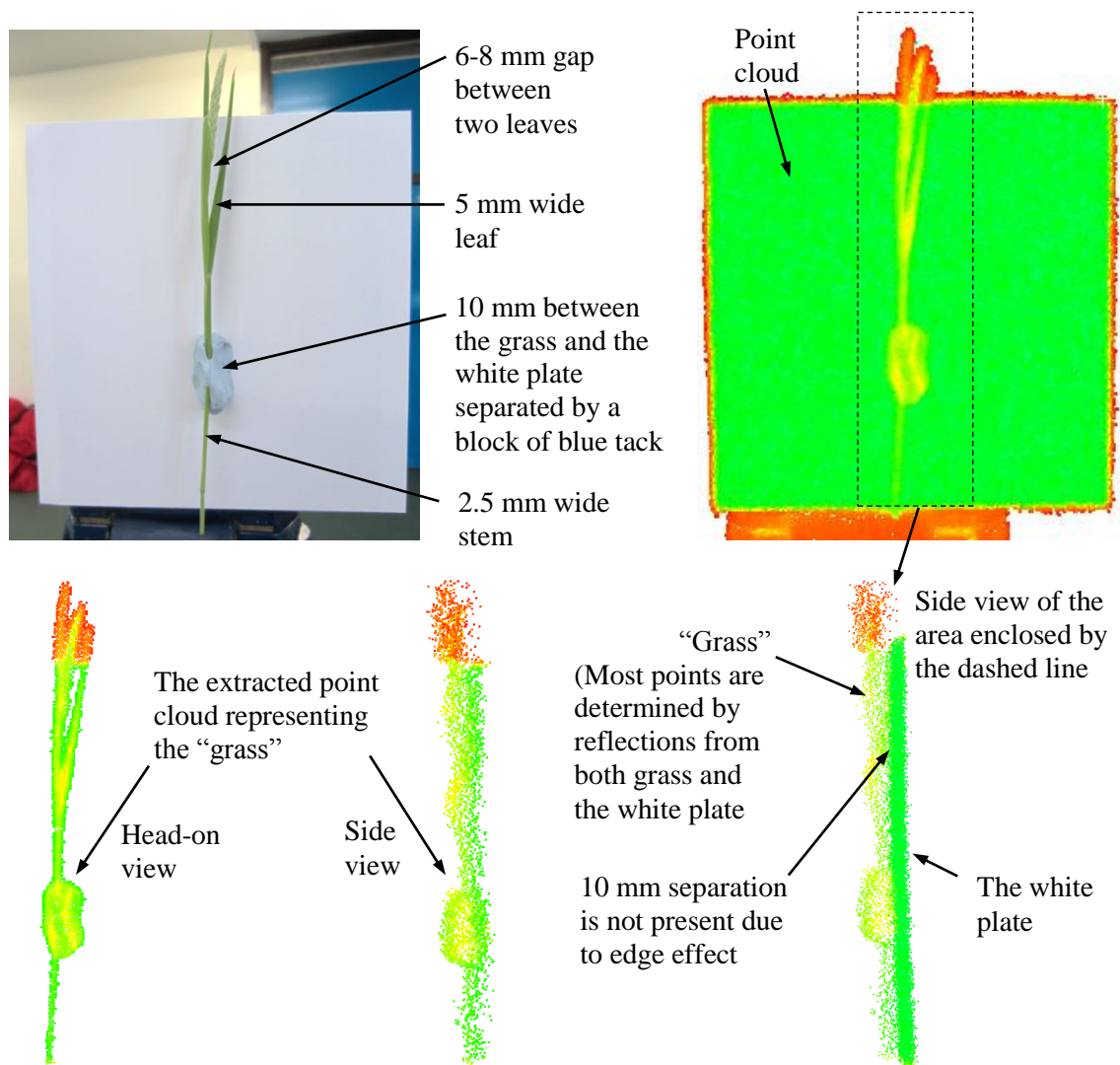


Figure 4.3: The scan data of individual grass.

4.3 Data processing

Data registration (the point clouds from Stations 1 and 2 were registered to the coordinate system of the total station) and initial data processing such as data selection were carried out in the Leica Cyclone® 7.3. Data filtering was implemented in MATLAB® (R2012a), and the post-filtering data exported to ArcMap® 10.0 for surface generation, comparison and visualisation.

4.3.1 Bare ground surface

Based on the bare ground points surveyed, the bare ground surface (Figure 4.4) was generated using the natural neighbour interpolation method developed by Sibson (1981). This method provided a smoother approximation than a linear interpolation and did not require any input parameters apart from the data points. A more complicated interpolation method such as kriging was not necessary for this study since the data density was relatively high and the ground surface was flat. For consistency, the natural neighbour interpolation was used for all the surfaces generated in this study.

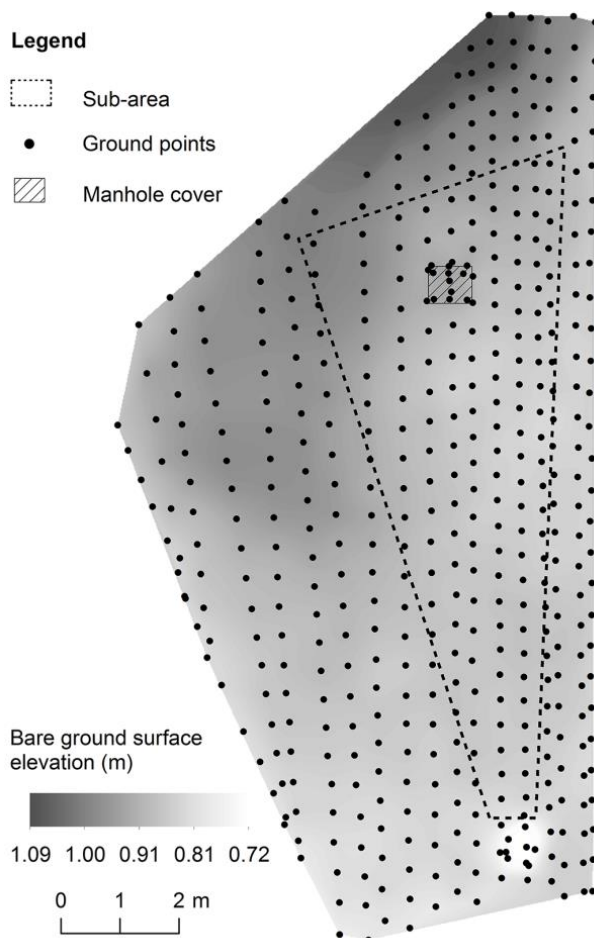


Figure 4.4: The bare ground surface elevation above an arbitrary datum-plane.

4.3.2 Methods to reduce vegetation noise

Ground vegetation results in noisy data if the information desired is the bare ground surface. In this circumstance, the noise needs to be eliminated or reduced. The most direct solution is to remove the grass physically before the laser scans take place. However, this may not always be feasible, in particular for a large area. Instead, filtering methods can be considered.

The literature reports a variety of filtering methods for different applications. In this chapter, a simple local-lowest-point filter was used. A second method, based on the intensity of scan points, is also discussed as being potentially useful in certain cases. As the grass at the study site was dense, the TLS data are likely to represent the vegetation only. Therefore, the second method was not considered suitable for this study.

4.3.2.1 *Local lowest point*

The local-lowest-point filter approach has been used by several researchers to remove or minimize vegetation-induced error (Latypov 2002; Guarnieri et al. 2009; Wang et al. 2009; Coveney and Fotheringham 2011). In this method, a window (usually a square) of a given side length is first defined. The window moves stepwise to select a series of local minimum elevation points. This method works well when the terrain is flat with little variation in elevation. For inclined terrain such as an engineered slope, this method may be less useful since spatial changes in elevation will influence the selection of the local lowest points. In the case of rough hilly terrain, this method can also result in the top of convex-shaped surfaces being removed. Two simple solutions for an inclined surface would be: (i) to detrend the surface and then apply the local-lowest-point method, or (ii) to create a series of local fitting surfaces and choose the point furthest below the fitting surface as the lowest point. Alternatively, other types of filter such as linear prediction (Kraus and Pfeifer, 1998; Pfeifer, et al., 2001) and TIN densification (Axelsson, 1999) may be considered.

For a survey dataset already obtained, the local lowest points represent the best results that can be achieved. The only parameter affecting the selection of the lowest points is the size of the moving window. There are no standards for determining the size of the search window. In general, a larger search window is likely to capture a point closer to the bare ground, and hence reduces the overall vegetation-induced elevation error. However, a larger window will lead to data of coarser spatial resolution.

In this study, the window size was fixed to 60 mm by 60 mm, based on the following considerations: (i) the search window should preserve the systematic elevation error caused by the vegetation and its spatial characteristics; (ii) the vegetation height estimated by local highest

Chapter 4. Vegetation Effects

points should match approximately the actual grass heights (the moving-window approach was also used to choose local highest points for the estimation of local vegetation height.).

The step size of the window movement was also 60 mm, leading to a grid of non-overlapping cells each 60 mm by 60 mm. In each grid cell, one local lowest point and one local highest point were selected. The use of the same window size over the whole survey area can cause a relative bias if scan data densities vary spatially. This bias can be used to assess the dependence of vegetation error on data density.

4.3.2.2 *Intensity method*

In addition to the xyz coordinates, the intensity of each scan point is also recorded, which represents the power density of the reflected laser light. The intensity depends on the surface reflectance; different surface materials in a scan scene may result in different intensities. Such a distinction in intensity can be considered for data classification or filtering. In the context of vegetated ground, the intensity of grass is different from that of soils for the same scan conditions and survey geometry. However, the intensity also depends on other parameters such as scan distance and angle of incidence of the beam relative to the normal to the surface being illuminated. Several researchers (Kaasalainen et al. 2005 and 2009; Hofle and Pfeifer 2007; Pfeifer et al. 2007; Jutzi and Gross 2009; Errington et al. 2011) have investigated the effects of surface reflectance, incidence angle and scan distance on intensity and tried to find relations between intensity and these parameters.

However, such relations are unlikely to hold for actual scans since many parameters combine to determine the actual intensity. In the context of vegetated ground surfaces, the intensity may also be affected by edge effects. Nield et al. (2011) found that the moisture content of soils affected the intensity of the survey data acquired in a beach environment. Thus it is difficult to identify a general algorithm that can identify different types of materials based solely on the intensity recorded by the TLS. Nevertheless, the intensity data may aid in the classification of different objects in a particular case. For example, Guarnieri et al. (2009) reported on the use of intensity to classify objects presented in a marsh land, including vegetation, bare soil and water.

The vegetation investigated in this study was green grass. In physics, it is well known that the colour of an object depends on two factors: the light source for the object and the wavelengths of light the object reflects. The light source for the grass in this case study is the sunlight, which emits visible light of all wavelengths. Green grass suggests that its capability of reflecting green light is much stronger than that for other visible light. The laser emitted by the ScanStation C10 is a green pulse of wavelength of 532 nm (Leica Geosystems, 2012b). Compared to lasers of

other colours, a green laser on green grass results in the laser being reflected strongly by the grass. Hence a high intensity of a returned signal is expected.

4.3.3 Vegetation surface, height and error

To avoid confusion, some of the terms used in the rest of this chapter are defined in this section, with the aid of the illustration shown in Figure 4.5.

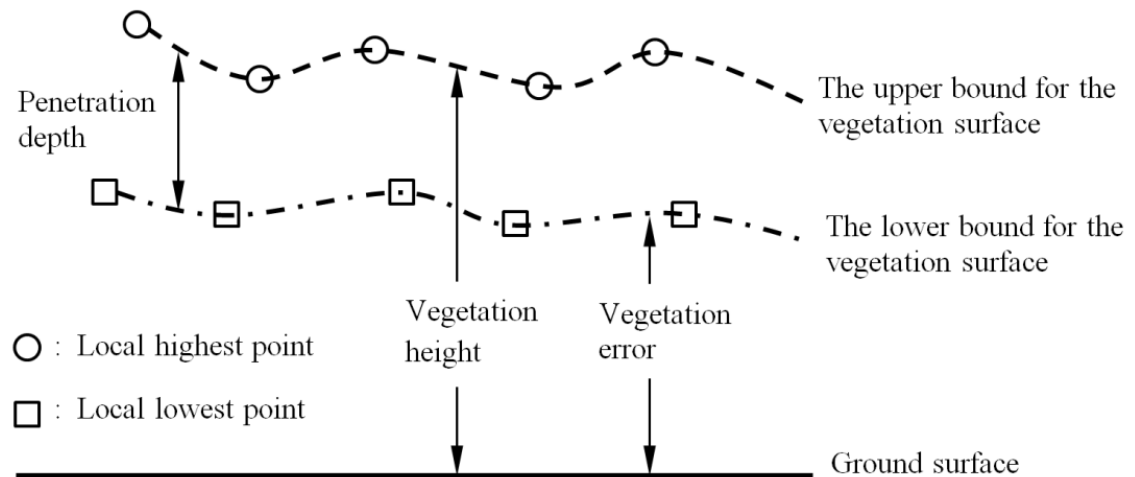


Figure 4.5: The vegetation surface, vegetation height and error.

4.3.3.1 The lower/upper bound for the vegetation surface

A series of local lowest/highest points were selected using the moving window described in Section 4.3.2. Based on these points, the lower/upper bounds for the vegetation surface were created using natural neighbour interpolation.

4.3.3.2 Vegetation error

The vegetation error was defined as the elevation difference between the post-filtering point cloud and the bare ground. To show its spatial characteristics, the lower bound for the vegetation surface was used in this chapter. Hence the vegetation error was represented by the elevation difference between the lower bound for the vegetation surface and the bare ground surface. Note that the term vegetation error is used loosely to refer to the elevation error caused by ground vegetation in the following discussion.

4.3.3.3 Vegetation height

It was assumed that the local highest points gave a reasonable representation of the top surface of the vegetation. The vegetation height was represented by the difference between the upper bound for the vegetation surface and the bare ground surface.

4.3.3.4 Penetration depth

The penetration depth was defined as the elevation difference between the upper and lower bounds for the vegetation surface.

The process from the selection of local lowest and highest points to the creation of lower and upper bounds for the vegetation surface is illustrated in Figure 4.6. Taking the S1H1 point cloud, for example, the number of data points (Figure 4.6(a)) was 0.76 million. The original point cloud was thinned using a 60 mm by 60 mm search window. The post-filtering point cloud (Figure 4.6(b)) had 8348 data points. The lower-bound of the vegetation surface is shown in Figure 4.6(c).

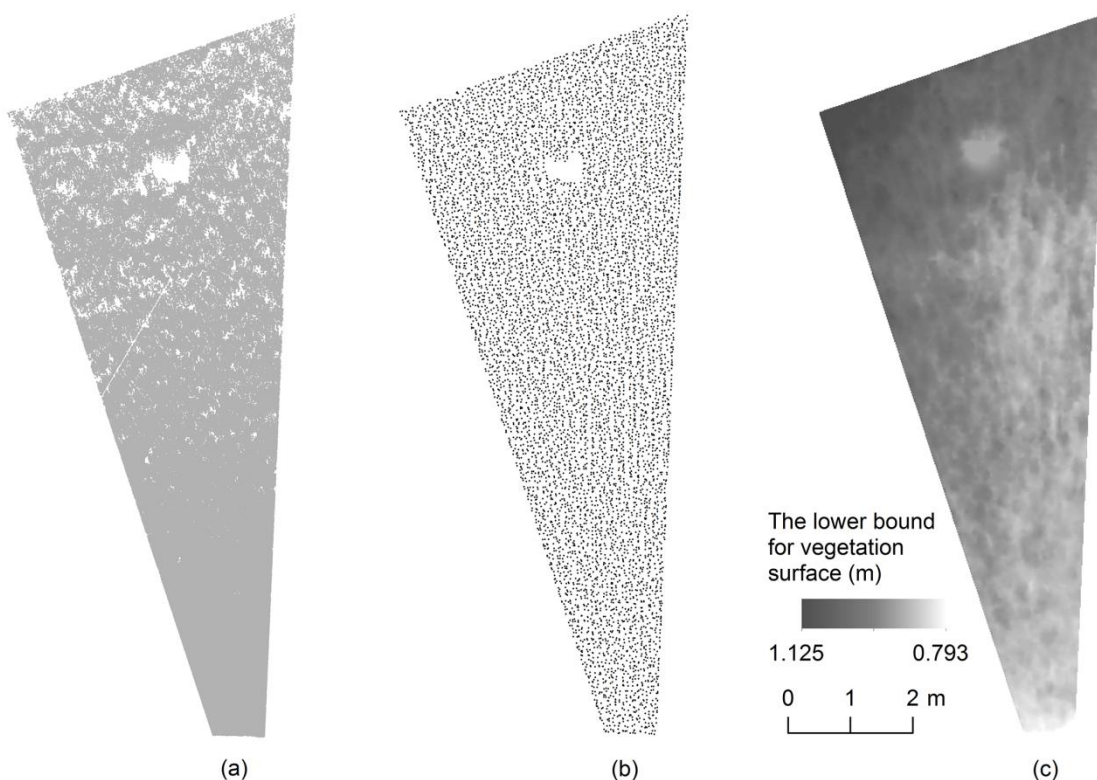


Figure 4.6: (a) The S1H1point cloud; (b) the post-filtering point cloud (local lowest points) using a 60 mm by 60 mm search window; (c) the lower bound of the vegetation surface created from the local lowest points using natural neighbour interpolation.

4.4 Results

4.4.1 Total station measurement accuracy

The total station had a very high range and angular accuracy. The pole supporting the target was held vertically with the aid of a mini-tripod, and the ground points were within 15 m of the total station. Thus the accuracy of individual measurements was expected to be better than +/- 3 mm.

The interpolation error of the bare ground surface was also small because the ground was relatively flat and a dense sample of ground points was acquired. Thus the ground surface was an accurate representation of the actual terrain surface.

4.4.2 Registration error

All of the survey data were registered to the coordinate system of the total station. Registration was carried out using Cyclone[®] 7.3 and the maximum registration error was approximately 2 mm. An adjacent building was also recorded by the scanner from different scan locations. The scan data representing the building facade confirmed a registration accuracy of better than ± 2 mm. As this is very small, it is not considered separately in the following discussion on the vegetation error.

4.4.3 Vegetation error and factors influencing it

The vegetation height and error maps for the S1H1 point cloud are shown in Figure 4.7 (a) and (b), respectively. The vegetation height and error at the manhole cover were both about $\pm 2-3$ mm. This suggests that the measurement (total station and laser scanner) and registration errors had small effects on the assessment of the vegetation error.

There is a large positive correlation between the two datasets (Figure 4.7 (a) and (b)) in most areas. In general, greater vegetation errors occurred where the grass was longer. However, the vegetation error was relatively small for the area close to Station 1 despite relatively long grass being present. Two main factors might have caused this. One is the density of scan points, which tended to decrease with the scan distance. The other is the incidence angle (the angle formed by the laser beam and the normal to the surface being illuminated). Ground visibility decreased as the incidence angle increased. Smaller incidence angles for closer ground areas meant that it was easier for laser beams to penetrate through the grass and reach a lower level.

To confirm these points, the spatial data shown in Figure 4.7 are visualised differently in Figure 4.8. In Figure 4.8(a), the vegetation error is plotted against the vegetation height, giving a line of least-squares fit of having a slope of 0.65. This value can change with the size of the search window adopted. Interestingly, the fitted line passes through the origin, i.e. there is no vegetation error if the vegetation height is zero. Hence the *average* vegetation error was about 65% of the vegetation height. This linear relation indicates that the growth of grass would increase the vegetation error in TLS survey data. The variation of the data from the fitted lines in Figure 4.8(a) was relatively large. This was because several parameters combined to influence the vegetation error, such as incidence angle, data density and edge effects.

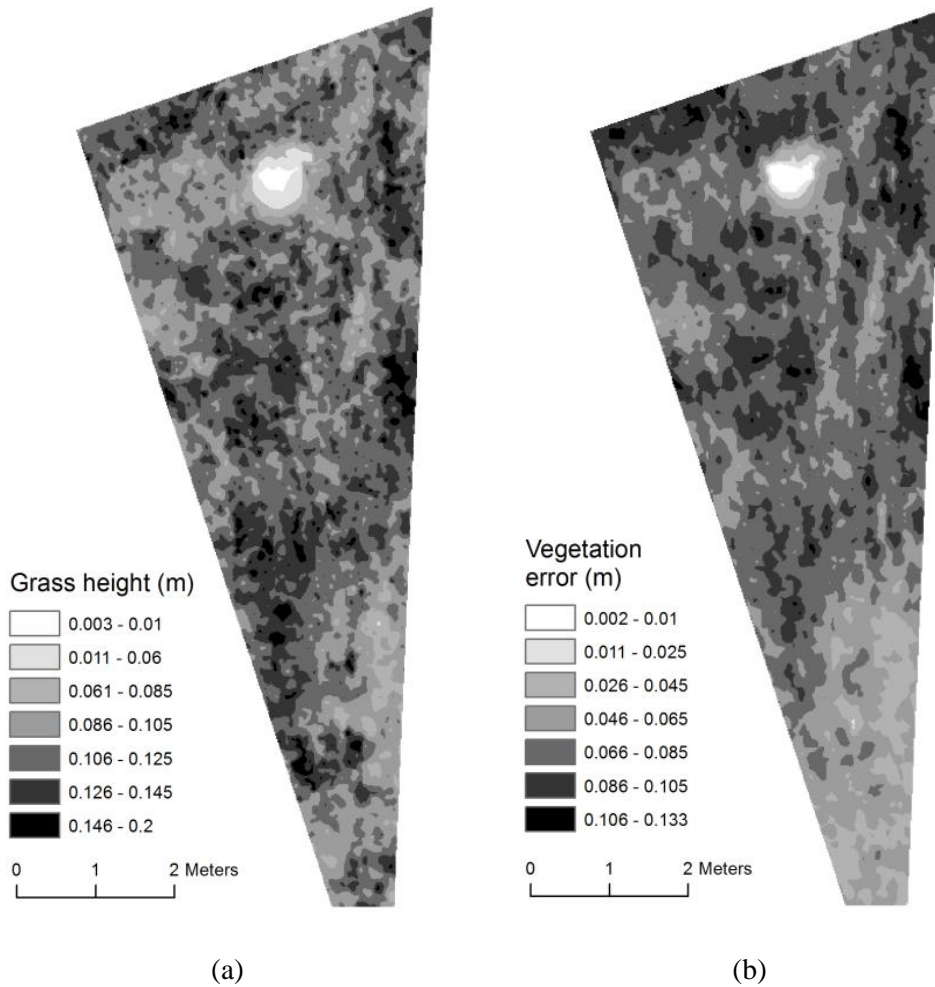


Figure 4.7: (a) Vegetation height; (b) vegetation error (both derived from the S1H1 point cloud).

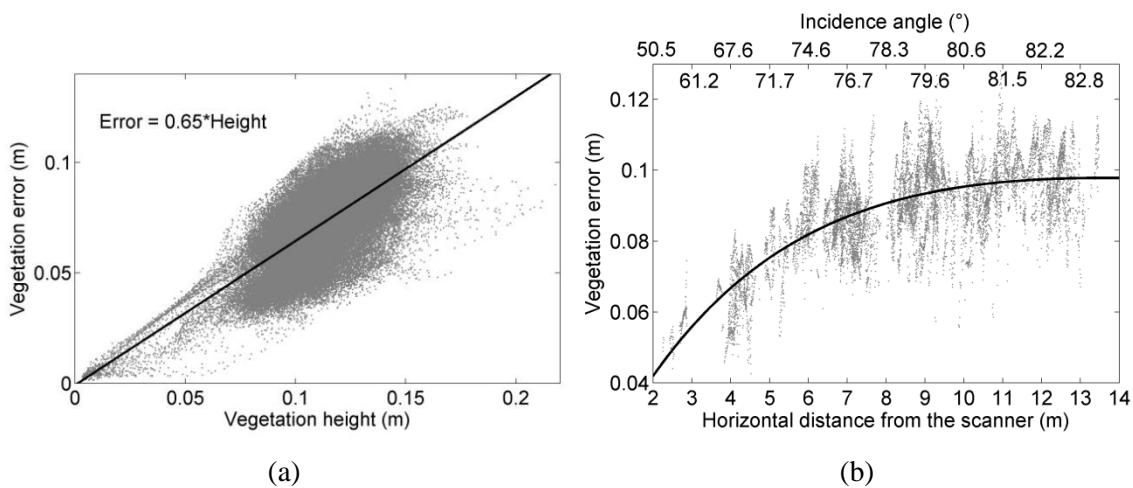


Figure 4.8: (a) The relation between vegetation height and error shown in Figure 4.7; (b) the variation of the vegetation error with the scan distance for grass of similar height (0.135 m – 0.15 m).

To investigate how the vegetation error varies with the scan distance, data points representing vegetation heights between 0.135 m and 0.15 m were selected. The horizontal distances between the individual data points selected and the scanner were then calculated. The variation in vegetation error with scan distance (and incidence angle) is shown in Figure 4.8(b). For grass of similar heights (0.135 m – 0.15 m), the vegetation error increased gradually with scan distance and then plateaued. The rate of change in incidence angle decreased quickly and its influence vanished for distant areas (Figure 4.8(b)). The data density, which decreased with the scan distance, was also a major contributing factor. The variability of the data in Figure 4.8(b) was likely due to the variation of the actual grass height within each individual search window.

Figure 4.5 shows that the penetration depth is equivalent to the difference between the estimated grass height and vegetation error. Based on the linear relation shown in Figure 4.8(a), the average penetration depth was about 35% ($= 1 - 0.65$) of the grass height. Its dependence on the vegetation height was most likely due to the variation of vegetation density along its depth. At the study site, it was observed that short grass was generally denser than longer grass. However, it is important to appreciate that the penetration depth was affected by other factors such as the incidence angle. Hence it varied spatially for vegetation of the same height but with different incidence angles.

4.4.4 Other factors affecting vegetation error

The vegetation error reported in Section 4.4.3 was based on a single scan (S1H1). The vegetation error derived from the survey data obtained in another scan situation may be different. The differences and associated contributing factors are investigated in this section.

The S1H1 point cloud served as the reference TLS dataset. The point cloud obtained at another scan situation was compared with the reference one to produce the relative vegetation error, which was used for the following discussion. An advantage of using the relative error is that it shows the extent to which the vegetation effect may be reduced in surface deformations derived from repeated surveys of the same area. As the same bare ground surface was used to derive the vegetation error, the relative vegetation error is equivalent to the difference between the lower bounds for the vegetation surface of the two TLS datasets compared.

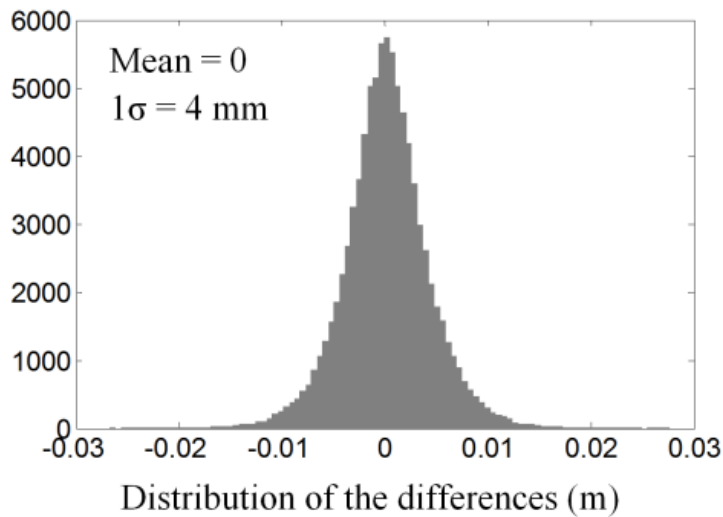
4.4.4.1 Repeatability

Although many terrestrial laser scanners record data points in a regular pattern (defined by horizontal and vertical scan resolutions), there are random elements in the laser scanning process. The selection of initial scan angles may be different in repeat scans. There are also random errors in the direction of a laser beam. In addition, the grass can sway in the wind and

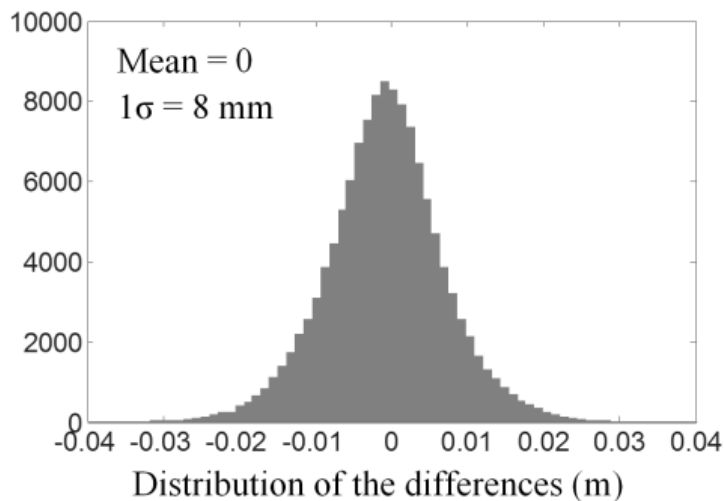
Chapter 4. Vegetation Effects

hence edge effects may vary from one scan to another. In a vegetated environment, these random uncertainties combine to affect the repeatability.

The lower bound for the vegetation surface was derived for the point clouds S1H1 and S1H2. These lower bounds were then compared and the difference is shown in Figure 4.9(a). The result for two successive coarse-resolution scans (S1L1 and S1L2) is shown in Figure 4.9(b).



(a)



(b)

Figure 4.9: Elevation differences between the lower bounds for the vegetation surface between: (a) repeat fine-resolution scans (S1H1-S1H2); (b) repeat coarse-resolution scans (S1L1 – S1L2), acquired under the same scan conditions.

There is no systematic difference in either case. The standard deviation of the differences for repeat fine-resolution scans was 4 mm. In addition to the random uncertainties described earlier, measurement errors could also contribute to this difference. Since this difference was not great, it is reasonable to argue that repeat fine-resolution scans are not sensitive to random errors. The difference for repeat coarse-resolution scans was 8 mm (at 1σ). Thus random uncertainties have a greater influence on repeatability for coarse-resolution surveys.

4.4.4.2 *Different scan resolutions*

Figure 4.10 shows the difference in the relative vegetation error between the point clouds S1H1 and S1L1. The distribution of the differences shows a bias of about 11 mm. This suggests that in general a finer scan resolution is likely to reduce the vegetation error. However, the point cloud of the coarse resolution had smaller vegetation errors at a limited number of locations. The magnitude of vegetation error depends largely on the depth that the laser signals can travel to. The actual depth reached by an individual laser beam does not depend on the scan resolution. However, a finer resolution produces more laser beams within a given area. This will increase the overall chances of laser beams reaching a lower depth.

The reduction in vegetation error using a finer scan resolution was less obvious for the area adjacent to Station 1. In this case, it is likely that the density of the grass played a major role. As the grass was quite dense, the space between grass blades was limited. Meanwhile, the point density for a coarse-resolution scan was also relatively high in the area adjacent to the scanner. There might be a limit beyond which further increases in scan resolution would not reduce the vegetation error. This was because the edge-effect weighting (Section 4.2.4) was limited by the spot size relative to the gap between grass leaves.

4.4.4.3 *Different scan locations*

The same area was scanned from two different locations (Station 1 and Station 2), both with fine scan resolution. The relative vegetation error is illustrated in Figure 4.11 and its distribution shows a wide dispersion. The bias was 5 mm and the standard deviation 15 mm. In addition to the random errors discussed in Section 4.4.4.1, several factors led to these differences. The point densities and incidence angles over the scan area were different because the scan distances from Stations 1 and 2 were generally different. Variations in vegetation characteristics (e.g. leaf orientation) from different view directions may have also contributed. For the small area close to Station 1, the vegetation error in S1H1 was smaller than that in S2H, because of the higher point density and smaller incidence angle for this area. The positive and negative differences were about the same in the distribution plot (Figure 4.11). This suggests that scanning the same area in multiple directions may reduce the overall vegetation error.

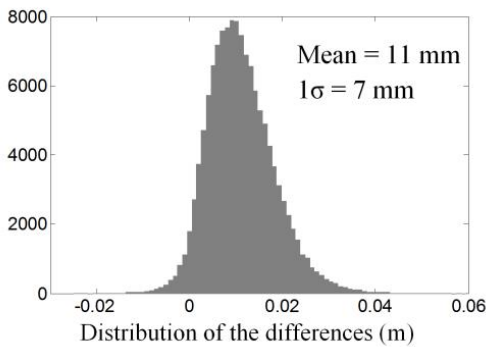
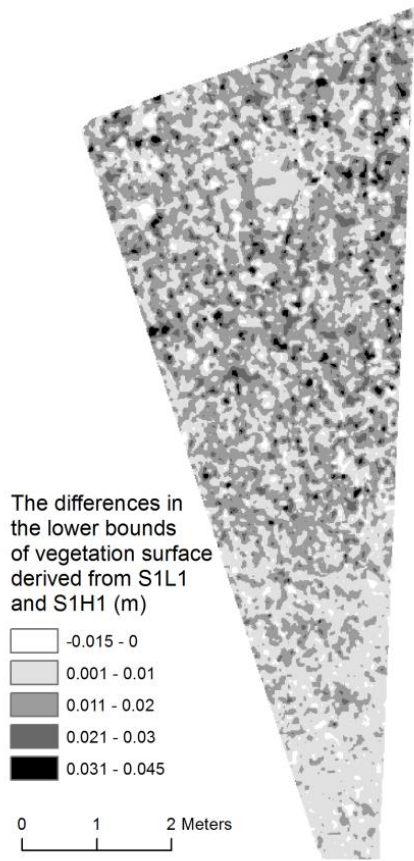


Figure 4.10: Difference in the lower bound of vegetation surfaces for coarse- and fine-resolution scans (S1L1 –S1H1).

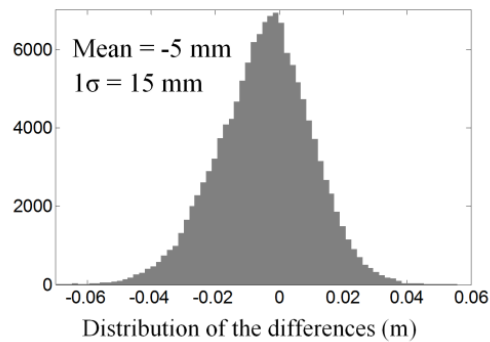
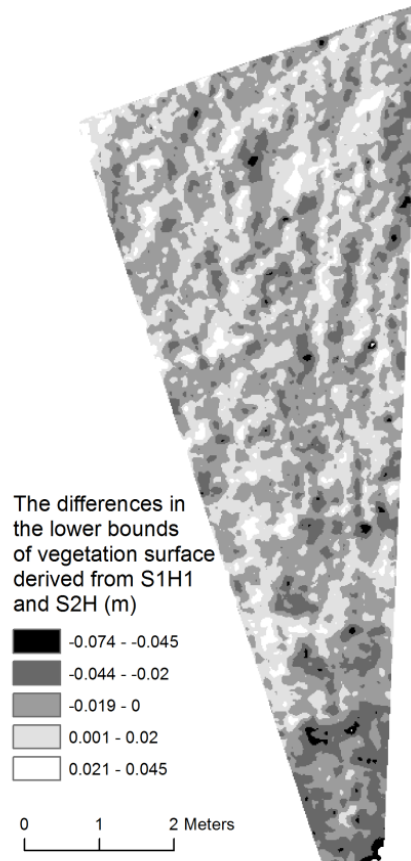


Figure 4.11: Difference in lower bound of vegetation surfaces for fine-resolution scans from different scan stations (S1H1-S2H).

4.4.5 A second experiment

A second experiment was carried out at another vegetated site located on the campus of the University of Southampton. The grass was green, upright, and had moderate tolerance for foot traffic. The grass was shorter (mostly 35 mm - 80 mm) and slightly less dense than that at the first site described in Section 4.2.1. This second experiment was carried out only to explore the relation between vegetation height and error. The experimental methods were similar to those stated in Section 4.2. The selection of local lowest and highest points was based on a search

window size of 60 mm by 60 mm. The data processing was the same as that described in Section 4.3. The results showed similar behaviour to that discussed in Section 4.4.3. However, the average vegetation error was found to be approximately 60% of the grass height (Figure 4.12), slightly smaller than that (65%) for the first site. The difference is reasonable and can be seen as some evidence of generalizability, as the grass at the two sites had different characteristics.

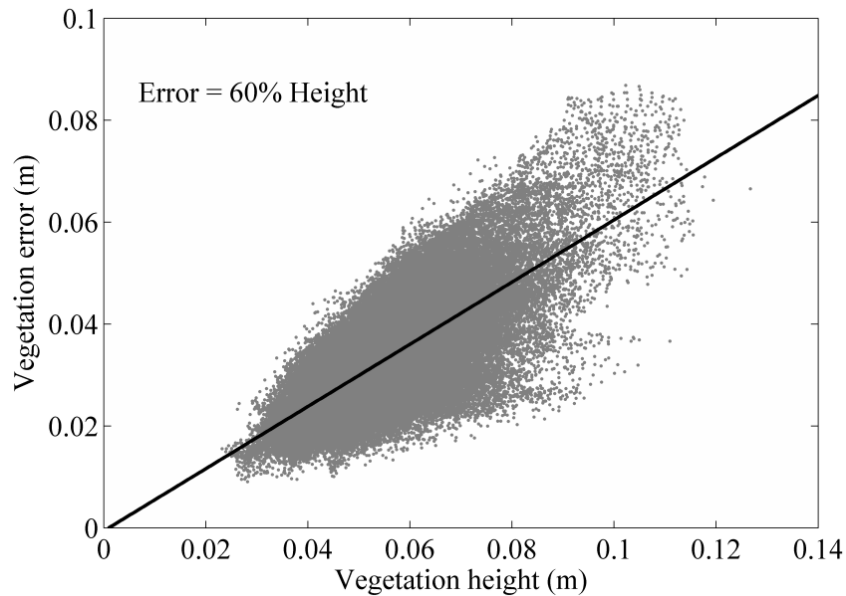


Figure 4.12: The relation between vegetation height and error for the second site.

The results of the two experiments reported in this chapter suggest that the relation between vegetation error and grass height is likely to depend on grass types and densities. Further research is required to confirm this.

4.5 Discussion

The study results confirm that lower incidence angle can reduce vegetation error. This reduction is quite effective for the dense vegetation in this case study. Hence it would be better to place a scanner at a lower level to scan an area of a vegetated slope at a higher level. In practice, however, it could be difficult to identify a favourable scan direction along which the vegetation error is the smallest. Therefore, a combination of scans of the same area in different directions could potentially reduce the overall vegetation error.

The average vegetation error in the TLS data representing a densely vegetated area is reasonably large. In this case study, it was about 65% of vegetation height. Digital elevation models created

Chapter 4. Vegetation Effects

from these TLS data may not be fit for purpose for some applications, depending on the requirements of accuracy. In cases where a high accuracy is essential and the sites to be surveyed are relatively small (e.g. engineered slopes), it would be better to remove vegetation before scans are carried out.

For surface deformation detection, repeat scans at a certain time interval are needed. A vegetation error is present in each individual scan and a proportion of it can be cancelled out when multi-temporal TLS data are compared. The results in this case study suggest that repeatedly surveying a vegetated area from the same multiple locations and with the same scan parameters (fine resolution is preferred) is likely to reduce the vegetation error in the measured surface deformations. Another problem for monitoring the vegetated terrain surfaces is the growth or die back of vegetation over time, which can cause a systematic elevation error in surface deformations. This error can be estimated if the relation between vegetation error and height for a particular type of grass can be established.

A larger search window generally leads to lower data points and hence reduces the overall vegetation error. However, the price of using a larger search window is the loss of point density in the final data set. The spatial characteristics of the terrain surface may also disappear. These factors have to be balanced when a search window size is selected.

The average penetration depth was about 35% of the grass height. A potential use of this relation is to estimate the grass height from the penetration depth, defined simply as the difference between the upper and lower bounds for the vegetation surface. The grass heights estimated and the upper bound for the vegetation surface could then be used to infer the bare ground surface. However, it is important to appreciate that this value (35%) represents an average level of penetration. The penetration depth varied spatially, mainly depending on grass characteristics (including, height), incidence angle and scan resolutions. Additional experimental data are required to confirm this approach.

4.6 Summary

In a TLS survey, the elevation error due to ground vegetation is affected by a variety of parameters, principally the vegetation height and density, scan distance, scan resolution and incidence angle. Edge effects can lead to a smaller vegetation error by recording a scan point lying somewhere between the first surface encountered and a more distant surface. For the fine-resolution scan considered in this study, the vegetation error was about 65% of the grass height

for a 60 mm by 60 mm filter window. A larger search window could further reduce the vegetation error by selecting lower points, but topographical detail would be lost.

A fine-resolution scan can reduce vegetation error but is less so for dense grass. Using lower incidence angles (greater visibility) can also reduce vegetation error, as will scanning the same area from multiple locations.

For detecting deformations, vegetation errors in data from sequential surveys will cancel out to some extent, especially for the multi-temporal datasets acquired from the same multiple locations and with the same scan parameters. These errors, and the ways in which they can be minimised, must be taken into account when using TLS surveying in an attempt to detect ground movements.

Chapter 5 :

Propagation of Measurement Errors

5.1 Introduction

A point cloud obtained from TLS surveying consists of scattered topographical points, which can be used as source data points for building DEMs. Source data points can also come from other point measurement techniques, such as DGPS and light detection and ranging (LiDAR). The accuracy of DEMs is inevitably affected by measurement errors in individual source data points. The positional errors in TLS scan points have been discussed in Chapter 3. This chapter aims to give an insight into how errors in source data points affect DEM accuracy.

The digital elevation modelling method considered in this chapter is a TIN with linear interpolation. Unlike many of other modelling methods, TINs do not require any model parameters such as the number of neighbouring data points and search radius, thus simplifying the modelling process. It is common for GIS designers to use relatively simple and straightforward modelling methods to speed up execution and simplify the decision process for users (Kyriakidis and Goodchild, 2006). In fact, TINs are widely used in practice. For example, the Ordnance Survey in the UK uses TINs in the production process for orthorectified digital imagery and a range of height products. Researchers (Rumsby et al., 2008; Heritage et al., 2009; Wheaton et al., 2010; Day et al., 2013) have used TINs derived from topographical survey data for detecting surface deformations.

Previous studies on how errors in source data points affect the DEM accuracy have mainly focused on vertical error propagation. Zhu et al. (2005) reported that the average elevation error variance of a triangular surface was half the vertical error variance at node points, based on the assumption that the error variance of node points is identical and independent. Shi et al. (2005) estimated the propagated error variance from source data into DEMs created through higher-order interpolation (biquadratic and bicubic). Aguilar et al. (2006) studied the accuracy of grid DEMs linearly constructed from scattered sample data. Only the average error variance for a TIN model was evaluated in these studies (i.e. Zhu et al., 2005; Shi et al., 2005; Aguilar et al.,

2006). Kyriakidis and Goodchild (2006) also investigated the average error variance of three linear interpolation methods (line linear, TIN linear and bilinear), and the propagation of vertical error variance at node points into a generic point using the geostatistics framework. Hu et al. (2009) approximated a complex function using functions to assess the accuracy of DEMs, including TIN. They found that for each triangular surface the propagated error variance at any point within the triangular surface was bounded by the largest error at the triangle vertices. There may also be a lower bound dictating that the propagated error variance at any point is greater than a given value. In these studies, no survey data were used to validate the error variance propagated.

In previous research, the propagation of errors in the planimetric or horizontal direction was not considered. This may be reasonable for the assessment of an existing DEM since it is known that horizontal error will cause vertical error. The assessment can be carried out either by evaluating the elevation differences at a number of check points measured using another instrument, or by comparing the DEM with a benchmark DEM created using higher accuracy measurements. However, for most topographical point measurement data, the positional error has a horizontal component. The propagation of horizontal error variance directly from the topographical data points to DEMs has drawn little attention.

A propagation solution can be quite useful, in particular when quantitative information on the errors in topographical point measurements is available or can be assessed. When point measurements are used to create a DEM, the associated horizontal and vertical errors will be propagated into the DEM. The focus of this chapter is on the propagation of error variance from individual source data points into any point of interest in a TIN model. Both horizontal and vertical errors in the source data are considered, and an analytical approach is introduced. To test the method, Monte Carlo simulations and laser scanning experiments were carried out.

5.2 TIN with linear interpolation

TIN is a popular means of representing a terrain surface in digital elevation modelling. In this method, the optimal Delaunay triangulation is commonly used for the selection of data points and formation of triangles. The triangles are created in such a way that no data point is inside the circumcircle of any triangle and their edges are not intersected by each other. All the triangle-shaped surfaces over the spatial extent of the data points constitute a complete and continuous surface. Within each triangle, the surface can be expressed by a plane (Equation (5.1)) determined from the three vertices of the triangle (Figure 5.1). The elevation of a

particular point within a given triangle is determined by the linear function (i.e. linear interpolation):

$$z(x, y) = ax + by + c \quad (5.1)$$

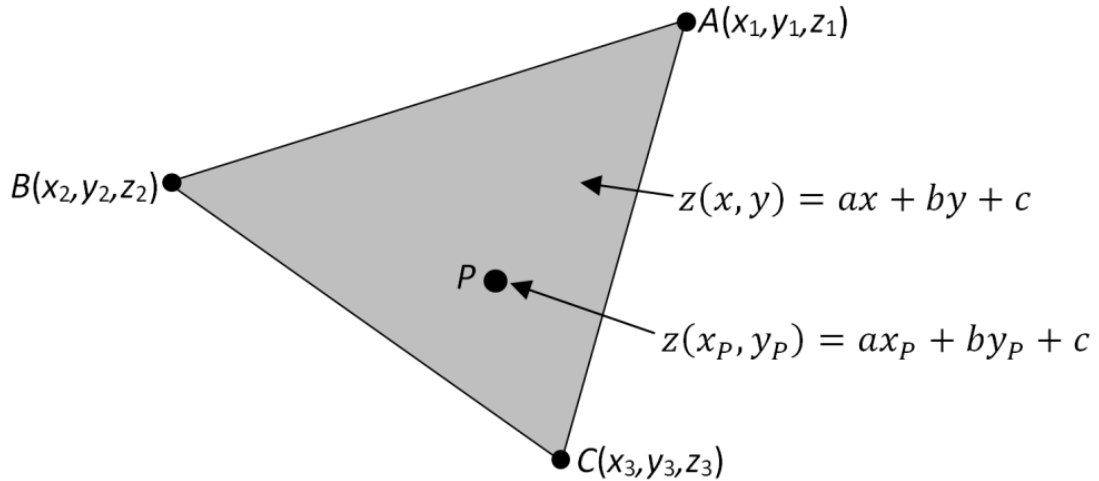


Figure 5.1: TIN model with linear interpolation: survey data points A, B and C are three vertices of a triangle in a TIN model and their coordinates are (x_1, y_1, z_1) , (x_2, y_2, z_2) and (x_3, y_3, z_3) , respectively; Point P is located anywhere within the triangle and its elevation can be calculated by the linear function given in Equation (5.1).

Linear algebra gives the solutions for a , b and c in the format of determinants:

$$a = \frac{\begin{vmatrix} z_1 & y_1 & 1 \\ z_2 & y_2 & 1 \\ z_3 & y_3 & 1 \end{vmatrix}}{\begin{vmatrix} x_1 & y_1 & 1 \\ x_2 & y_2 & 1 \\ x_3 & y_3 & 1 \end{vmatrix}} \quad b = \frac{\begin{vmatrix} x_1 & z_1 & 1 \\ x_2 & z_2 & 1 \\ x_3 & z_3 & 1 \end{vmatrix}}{\begin{vmatrix} x_1 & y_1 & 1 \\ x_2 & y_2 & 1 \\ x_3 & y_3 & 1 \end{vmatrix}} \quad c = \frac{\begin{vmatrix} x_1 & y_1 & z_1 \\ x_2 & y_2 & z_2 \\ x_3 & y_3 & z_3 \end{vmatrix}}{\begin{vmatrix} x_1 & y_1 & 1 \\ x_2 & y_2 & 1 \\ x_3 & y_3 & 1 \end{vmatrix}} \quad (5.2)$$

5.3 Error propagation

The law of propagation of uncertainty has been used widely in the field of measurement science, and is based on a Taylor series expansion. The error propagation law for a multivariate model is used in this study without proof. A detailed guide on uncertainty evaluation and propagation can be found in Taylor (1982) and Cox and Harris (2006).

A DEM is created from a set of data points. In mathematical terms, the DEM is an output quantity while the data points are input quantities. The relationship between the output quantity

and the input quantities is the model, which can be a mathematical function or a stepwise algorithm. For N input quantities denoted by $\mathbf{I} = (I_1, \dots, I_N)$, the output quantity O can be expressed as:

$$O = f(\mathbf{I}) = f(I_1, \dots, I_N) \quad (5.3)$$

where f is a mathematical function. There may be more than one output quantity (say M in number), $\mathbf{O} = (O_1, \dots, O_M)$. In this case, the output quantities are:

$$\mathbf{O} = \mathbf{F}(\mathbf{I}) = \mathbf{F}(I_1, \dots, I_N) = (f_1(I_1, \dots, I_N), \dots, f_M(I_1, \dots, I_N)) \quad (5.4)$$

The law of uncertainty propagation for a multivariate model is expressed in Equation (5.5),

$$\mathbf{C}_O = \mathbf{J}_I \mathbf{C}_I \mathbf{J}_I^T \quad (5.5)$$

or equivalently in matrix form,

$$\begin{bmatrix} \sigma_{O_1}^2 & \sigma_{O_1 O_2} & \dots & \sigma_{O_1 O_M} \\ \sigma_{O_2 O_1} & \sigma_{O_2}^2 & \dots & \sigma_{O_2 O_M} \\ \vdots & \vdots & \ddots & \vdots \\ \sigma_{O_M O_1} & \sigma_{O_M O_2} & \dots & \sigma_{O_M}^2 \end{bmatrix} = \begin{bmatrix} \frac{\partial f_1(\mathbf{I})}{\partial I_1} & \dots & \frac{\partial f_1(\mathbf{I})}{\partial I_N} \\ \vdots & \ddots & \vdots \\ \frac{\partial f_M(\mathbf{I})}{\partial I_1} & \dots & \frac{\partial f_M(\mathbf{I})}{\partial I_N} \end{bmatrix} \begin{bmatrix} \sigma_{I_1}^2 & \sigma_{I_1 I_2} & \dots & \sigma_{I_1 I_N} \\ \sigma_{I_2 I_1} & \sigma_{I_2}^2 & \dots & \sigma_{I_2 I_N} \\ \vdots & \vdots & \ddots & \vdots \\ \sigma_{I_N I_1} & \sigma_{I_N I_2} & \dots & \sigma_{I_N}^2 \end{bmatrix} \begin{bmatrix} \frac{\partial f_1(\mathbf{I})}{\partial I_1} & \dots & \frac{\partial f_1(\mathbf{I})}{\partial I_N} \\ \vdots & \ddots & \vdots \\ \frac{\partial f_M(\mathbf{I})}{\partial I_1} & \dots & \frac{\partial f_M(\mathbf{I})}{\partial I_N} \end{bmatrix}^T \quad (5.6)$$

in which, $\sigma_{I_i}^2$ ($i = 1, \dots, N$) is the variance of input variables; $\sigma_{O_j}^2$ ($j = 1, \dots, M$) is the variance of output variables; $\sigma_{I_i I_k}$ ($i, k = 1, \dots, N; i \neq k$) is the covariance of input variables; $\sigma_{O_j O_l}$ ($j, l = 1, \dots, M; j \neq l$) is the covariance of output variables; $\frac{\partial f_i(\mathbf{I})}{\partial I_j}$ is the partial difference of the system of equations.

5.4 Propagated error variance of source data points

As it is difficult to consider the propagation of vertical and horizontal error variances simultaneously, they are considered separately and then combined in this chapter. In Section 5.4, the analytical solutions for propagation of error variance are derived, based on a

location-dependent parameter M . This parameter is then quantified in Section 5.5. The analytical solutions are validated using Monte Carlo simulations and two simple survey experiments in Section 5.6.

5.4.1 Propagation of vertical error

It is assumed that the horizontal uncertainty of the source data points is zero (i.e. they are error free). Therefore, only the vertical errors are propagated. An analytical solution is derived to compute the error variance at any point of interest in a TIN model. The solutions given in Equation (5.2) can be written in a linear format and rearranged as shown in Equation (5.7). This operation aims to distinguish the elevation variable z from the location variables x and y .

$$a = \frac{(y_2 - y_3)z_1 + (y_3 - y_1)z_2 + (y_1 - y_2)z_3}{x_1y_2 + x_3y_1 + x_2y_3 - x_3y_2 - x_1y_3 - x_2y_1} = a_1z_1 + a_2z_2 + a_3z_3$$

$$b = \frac{(x_3 - x_2)z_1 + (x_1 - x_3)z_2 + (x_2 - x_1)z_3}{x_1y_2 + x_3y_1 + x_2y_3 - x_3y_2 - x_1y_3 - x_2y_1} = b_1z_1 + b_2z_2 + b_3z_3 \quad (5.7)$$

$$c = \frac{(x_2y_3 - x_3y_2)z_1 + (x_3y_1 - x_1y_3)z_2 + (x_1y_2 - x_2y_1)z_3}{x_1y_2 + x_3y_1 + x_2y_3 - x_3y_2 - x_1y_3 - x_2y_1} = c_1z_1 + c_2z_2 + c_3z_3$$

in which, $a_1 = \frac{y_2 - y_3}{L}$; $a_2 = \frac{y_3 - y_1}{L}$; $a_3 = \frac{y_1 - y_2}{L}$, and $L = x_1y_2 + x_3y_1 + x_2y_3 - x_3y_2 - x_1y_3 - x_2y_1$; the same applies to b_1, b_2, b_3, c_1, c_2 and c_3 , the expressions for which are not listed here.

By substituting a, b and c in Equation (5.1) with the expressions in Equation (5.7), the elevation z_P of the point $P(x_P, y_P)$ in the TIN model can be calculated (Equation (5.8)).

$$z_P = ax_P + by_P + c$$

$$= (a_1z_1 + a_2z_2 + a_3z_3)x_P + (b_1z_1 + b_2z_2 + b_3z_3)y_P + (c_1z_1 + c_2z_2 + c_3z_3) \quad (5.8)$$

$$= (a_1x_P + b_1y_P + c_1)z_1 + (a_2x_P + b_2y_P + c_2)z_2 + (a_3x_P + b_3y_P + c_3)z_3$$

Rewriting Equation (5.8) in matrix form:

$$z_p = \begin{bmatrix} x_p \\ y_p \\ 1 \end{bmatrix}^T \begin{bmatrix} a_1 & a_2 & a_3 \\ b_1 & b_2 & b_3 \\ c_1 & c_2 & c_3 \end{bmatrix} \begin{bmatrix} z_1 \\ z_2 \\ z_3 \end{bmatrix} \quad (5.9)$$

On the right hand side of Equation (5.9), the first vector represents the location of the point P , the elevation of which is to be estimated (z_p). The second matrix is determined by the locations of the three vertices of a triangle. Recall that their positional errors are not considered at this stage. Therefore, the second term is a matrix of constants for a given triangle. The last vector represents the elevations of the three vertices of the triangle. Equation (5.9) shows that the elevation accuracy of the point P depends not only on the vertical accuracy of the survey data points but also its position (x_p, y_p).

Equation (5.9) can be expressed as:

$$z_p = m_1 z_1 + m_2 z_2 + m_3 z_3 \quad (5.10)$$

in which,
$$\begin{bmatrix} m_1 \\ m_2 \\ m_3 \end{bmatrix}^T = \begin{bmatrix} x_p \\ y_p \\ 1 \end{bmatrix}^T \begin{bmatrix} a_1 & a_2 & a_3 \\ b_1 & b_2 & b_3 \\ c_1 & c_2 & c_3 \end{bmatrix}$$

For a given triangle and a known interpolation location (x_p, y_p) within the triangle, m_1, m_2 and m_3 can be calculated. It is known that there are errors associated with z_1, z_2 and z_3 . The remaining question is how to propagate the vertical errors of data points into the elevation predicted at the location P .

Based on Equation (5.6) the error variance $\sigma_{z_p}^2$ of a particular point can be calculated as:

$$\begin{aligned} \sigma_{z_p}^2 = & m_1^2 \sigma_{z_1}^2 + m_2^2 \sigma_{z_2}^2 + m_3^2 \sigma_{z_3}^2 + 2m_1 m_2 \sigma_{z_1 z_2} + 2m_1 m_3 \sigma_{z_1 z_3} \\ & + 2m_2 m_3 \sigma_{z_2 z_3} \end{aligned} \quad (5.11)$$

in which, $\sigma_{z_1}^2, \sigma_{z_2}^2$ and $\sigma_{z_3}^2$ are the error variances of the three node points; $\sigma_{z_1 z_2}, \sigma_{z_1 z_3}$ and $\sigma_{z_2 z_3}$ are the covariances between the three node points.

It should be noted that Kyriakidis and Goodchild (2006) obtained a solution similar to Equation (5.11), based on the proportion (weight) of the areas of sub-triangles formed by triangle vertices

and a prediction location, to the total area of a TIN element. The weight was derived using a geostatistical formulation. Our study shows that the solution can also be obtained with error propagation directly through the linear function for a triangular surface. In addition, the dependence of the weight (m_i) on the prediction location and the spatial distribution of propagated measurement error variance are both investigated.

If the random errors in the elevations of node points (z_1 , z_2 and z_3) are independent of each other, Equation (5.12) can be used to propagate the error variances into the point P .

$$\sigma_{z_p}^2 = m_1^2 \sigma_{z_1}^2 + m_2^2 \sigma_{z_2}^2 + m_3^2 \sigma_{z_3}^2 \quad (5.12)$$

If the random errors are identical ($\sigma_{z_{node}}$) for all node points, Equation (5.12) can be further simplified to Equation (5.13).

$$\begin{aligned} \sigma_{z_p}^2 &= (m_1^2 + m_2^2 + m_3^2) \sigma_{z_{node}}^2 \\ &= M \sigma_{z_{node}}^2 \end{aligned} \quad (5.13)$$

M is a location-dependent parameter. The value of M depends on the actual location of the point of interest. This is demonstrated in Section 5.5.

5.4.2 Propagation of horizontal error

The horizontal error of a measurement does not affect its elevation component. However, if the terrain surface is inclined, the horizontal error will generate an elevation error during digital elevation modelling. Several researchers (Hodgson and Bresnahan, 2004; Su and Bork, 2006; Spaete et al., 2011) have reported that terrain slope influenced the accuracy of DEMs created from topographical survey data.

5.4.2.1 Geometric relation method

A straightforward way of investigating the effect of horizontal errors on elevation is to use the geometric relation. To simplify the demonstration, a 2D case is illustrated in Figure 5.2. It is also valid for a triangular surface in a TIN model. The horizontal error will generate an elevation error (from a DEM accuracy perspective) if the surface is inclined. The effect of the horizontal error (line AC) on DEM accuracy is equivalent to that of a vertical error (line AD), $|AD| = |AC| \tan \beta$. The angle β can be estimated from a slope map using a variety of means suggested in the literature. Alternatively, $|AD|$ can be approximated by $|EC|$ ($|EC| = |AC| \tan \alpha$), if the horizontal error $|AC|$ is small compared with the data point spacing. α

represents the angle of line BA , and is a known variable (because points B and A are measured and their coordinates are known). In the context of a triangular surface in a TIN model, α (in both X and Y axes) can be derived directly from Equation (5.1). In this approach, a separate slope map is not required, hence simplifying the work process. The following discussion is based on the second approach.

Based on the above, Equation (5.14) can be used to estimate the equivalent elevation error caused by the horizontal measurement error. The slope angle is derived from individual triangular surfaces in a TIN model, and may vary from one triangular surface to another.

$$\delta_{z_x} = \delta_x \tan \alpha_x \tag{5.14}$$

in which, δ_x is the horizontal error; α_x is the angle of inclination of the surface with respect to the X axis; δ_{z_x} is the equivalent vertical error caused by δ_x .

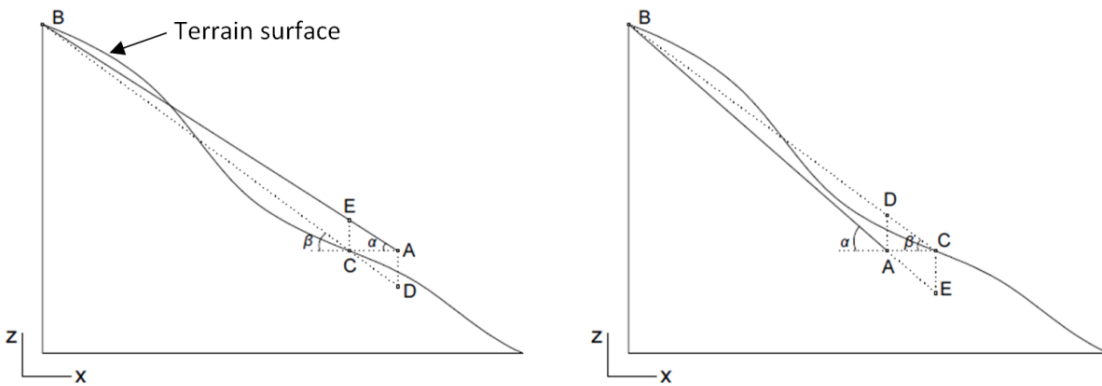


Figure 5.2: Elevation error caused by horizontal error of source data points: Points B and C are two terrain surface points to be measured. Assume the measurement of point B is free of error, and the measurement of point C has a horizontal error represented by dotted line CA ; Line BC represents the terrain surface without any measurement error (note that modelling error is not considered in this study). Points B and A are actual survey points acquired. Line BA is the actual representation of the terrain surface due to the horizontal measurement error from point C . The rise or fall of point E with respect to point C (the imaginary true terrain point) is equivalent to the rise or fall of point A (the actual survey point) with respect to point D , causing an elevation error (i.e. the elevation difference between line BE and BC). α is the slope angle of line BA and β is the angle of inclination of the terrain surface.

Once δ_{z_x} has been obtained, the problem is converted into the case discussed in Section 5.4.1, i.e. the propagation of vertical error variances. Therefore, Equation (5.11) can also be used to propagate the horizontal error. In the special case of the random horizontal error being

independent and identical ($\sigma_{x_{\text{node}}}^2$) for all three node points of a triangular surface, the vertical error variance $\sigma_{z_p}^2$ of a particular point due to the horizontal error is given by:

$$\begin{aligned}\sigma_{z_p}^2 &= M\sigma_{z_x}^2 = M(\sigma_{x_{\text{node}}} \tan \alpha_x)^2 \\ &= M(\tan \alpha_x)^2 \sigma_{x_{\text{node}}}^2\end{aligned}\quad (5.15)$$

in which $\sigma_{x_{\text{node}}}^2$ is the error variance of node points in the X axis.

5.4.2.2 Error propagation method

It is also possible to use the law of uncertainty propagation (Equation (5.6)) to solve the horizontal error propagation problem. To use this method, the measurement error was assumed to be small compared with the data point spacing (i.e. the second approach to derive slope angles in Section 5.4.2.1). Only the horizontal error component in the X axis is considered (it is the same for the Y axis). Equation (5.2) is rearranged so that the x_i ($i = 1,2,3$) are separated from the other components y_i and z_i ($i = 1,2,3$). Equation (5.16) is then obtained, which aims to emphasize that only x_i ($i = 1,2,3$) are random variables having uncertainty and the other components are constants if the three node points are known.

$$\begin{aligned}a &= \frac{(z_3 - z_2)y_1 + (z_1 - z_3)y_2 + (z_2 - z_1)y_3}{(y_2 - y_3)x_1 + (y_3 - y_1)x_2 + (y_1 - y_2)x_3} \\ b &= \frac{(z_2 - z_3)x_1 + (z_3 - z_1)x_2 + (z_1 - z_2)x_3}{(y_2 - y_3)x_1 + (y_3 - y_1)x_2 + (y_1 - y_2)x_3} \\ c &= \frac{(y_2z_3 - y_3z_2)x_1 + (y_3z_1 - y_1z_3)x_2 + (y_1z_2 - y_2z_1)x_3}{(y_2 - y_3)x_1 + (y_3 - y_1)x_2 + (y_1 - y_2)x_3}\end{aligned}\quad (5.16)$$

The expressions for a , b and c in Equation (5.16) are substituted into Equation (5.1). As this will make Equation (5.1) complex, the following expressions are used to simplify the equation after substitution.

$$\begin{aligned}r_0 &= x_p [(z_3 - z_2)y_1 + (z_1 - z_3)y_2 + (z_2 - z_1)y_3] \\ r_1 &= y_p z_2 - y_p z_3 + y_2 z_3 - y_3 z_2 \\ r_2 &= y_p z_3 - y_p z_1 + y_3 z_1 - y_1 z_3 \\ r_3 &= y_p z_1 - y_p z_2 + y_1 z_2 - y_2 z_1 \\ r_4 &= y_2 - y_3 \\ r_5 &= y_3 - y_1 \\ r_6 &= y_1 - y_2\end{aligned}$$

Giving:

$$z_p = \frac{r_1x_1 + r_2x_2 + r_3x_3 + r_0}{r_4x_1 + r_5x_2 + r_6x_3} \quad (5.17)$$

As only the horizontal error in the X direction is considered, it is assumed that there are no uncertainties associated with y_i and $z_i (i = 1,2,3)$. The point (x_p, y_p) is an interpolation location and does not have any uncertainty. Therefore, for a given triangle, $r_i (i = 4,5,6)$ are constants across the whole triangle while $r_i (i = 0,1,2,3)$ are location-dependent constants (i.e. they depend on the location of the point P).

Now the propagation of measurement errors in the X direction has been converted into a mathematical problem. Based on Equation (5.17), the original error propagation problem can be stated mathematically. It is known that $r_i (i = 1:7)$ are constants and $x_i (i = 1,2,3)$ are random variables with uncertainty. If the variances of $x_i (i = 1,2,3)$ and their covariances are known, what is the variance of z_p ?

It is not easy to calculate the partial differences for x_1, x_2 and x_3 in Equation (5.17). To avoid this, Equation (5.17) is further simplified as Equation (5.18).

$$z_p = \frac{n_1}{n_2} : F(n_1, n_2) \quad (5.18)$$

in which,

$$\begin{aligned} n_1 &= r_1x_1 + r_2x_2 + r_3x_3 + r_0 & : f_1(x_1, x_2, x_3) \\ n_2 &= r_4x_1 + r_5x_2 + r_6x_3 & : f_2(x_1, x_2, x_3) \end{aligned} \quad (5.19)$$

n_1 and n_2 are two new input variables and z_p is the output variable. This simplification will make the partial differences easier to calculate, but introduces two new variables that are correlated with each other, owing to the presence of common variables in the expressions for n_1 and n_2 . This should not be a problem since the covariance of n_1 and n_2 can be calculated using Equation (5.6).

Applying Equation (5.6) for this case:

$$\begin{bmatrix} \sigma_{n_1}^2 & \sigma_{n_1 n_2} \\ \sigma_{n_2 n_1} & \sigma_{n_2}^2 \end{bmatrix} = \begin{bmatrix} \frac{\partial f_1}{\partial x_1} & \frac{\partial f_1}{\partial x_2} & \frac{\partial f_1}{\partial x_3} \\ \frac{\partial f_2}{\partial x_1} & \frac{\partial f_2}{\partial x_2} & \frac{\partial f_2}{\partial x_3} \end{bmatrix} \begin{bmatrix} \sigma_{x_1}^2 & \sigma_{x_1 x_2} & \sigma_{x_1 x_3} \\ \sigma_{x_2 x_1} & \sigma_{x_2}^2 & \sigma_{x_2 x_3} \\ \sigma_{x_3 x_1} & \sigma_{x_3 x_2} & \sigma_{x_3}^2 \end{bmatrix} \begin{bmatrix} \frac{\partial f_1}{\partial x_1} & \frac{\partial f_2}{\partial x_1} \\ \frac{\partial f_1}{\partial x_2} & \frac{\partial f_2}{\partial x_2} \\ \frac{\partial f_1}{\partial x_3} & \frac{\partial f_2}{\partial x_3} \end{bmatrix} \quad (5.20)$$

Equation (5.20) is a generic solution, which can account for any given error variances (e.g. different error variances: $\sigma_{x_1}^2 \neq \sigma_{x_2}^2 \neq \sigma_{x_3}^2$) and correlations (i.e. $\sigma_{x_i x_j}$ ($i, j = 1, 2, 3$ & $i \neq j$) $\neq 0$) in the error propagation. However, in the following discussion, the special case of zero covariance and equal variances ($\sigma_{x_1}^2 = \sigma_{x_2}^2 = \sigma_{x_3}^2 = \sigma_x^2$) is considered in detail. There are cases where covariances are assumed to be zero, either because the error in source data is believed to be independent, or because no information on covariances is available (Kyriakidis and Goodchild, 2006). Some researchers (Li, 1993; Huang, 2000; Aguilar et al., 2006) have adopted this assumption (independent and identical) for propagating error variances of node points into DEM. In some cases, error in data points acquired by some instruments may be independent. For example, Hodge (2010) investigated random positional error of terrestrial laser scanning data points.

The partial differences with respect to x_i ($i = 1, 2, 3$) are:

$$\begin{aligned} \frac{\partial f_1}{\partial x_1} &= r_1 & \frac{\partial f_1}{\partial x_2} &= r_2 & \frac{\partial f_1}{\partial x_3} &= r_3 \\ \frac{\partial f_2}{\partial x_1} &= r_4 & \frac{\partial f_2}{\partial x_2} &= r_5 & \frac{\partial f_2}{\partial x_3} &= r_6 \end{aligned} \quad (5.21)$$

Substituting these partial differences into Equation (5.20):

$$\begin{aligned} \begin{bmatrix} \sigma_{n_1}^2 & \sigma_{n_1 n_2} \\ \sigma_{n_2 n_1} & \sigma_{n_2}^2 \end{bmatrix} &= \begin{bmatrix} r_1 & r_2 & r_3 \\ r_4 & r_5 & r_6 \end{bmatrix} \begin{bmatrix} \sigma_x^2 & 0 & 0 \\ 0 & \sigma_x^2 & 0 \\ 0 & 0 & \sigma_x^2 \end{bmatrix} \begin{bmatrix} r_1 & r_4 \\ r_2 & r_5 \\ r_3 & r_6 \end{bmatrix} \\ &= \begin{bmatrix} (r_1^2 + r_2^2 + r_3^2)\sigma_x^2 & (r_1 r_4 + r_2 r_5 + r_3 r_6)\sigma_x^2 \\ (r_1 r_4 + r_2 r_5 + r_3 r_6)\sigma_x^2 & (r_4^2 + r_5^2 + r_6^2)\sigma_x^2 \end{bmatrix} \end{aligned} \quad (5.22)$$

Chapter 5. Propagation of Measurement Errors

The variances and covariance of n_1 and n_2 are now obtained.

$$\begin{aligned}\sigma_{n_1}^2 &= (r_1^2 + r_2^2 + r_3^2)\sigma_x^2 \\ \sigma_{n_2}^2 &= (r_4^2 + r_5^2 + r_6^2)\sigma_x^2 \\ \text{cov}(n_1, n_2) &= \sigma_{n_1 n_2} \text{ or } \sigma_{n_2 n_1} = (r_1 r_4 + r_2 r_5 + r_3 r_6)\sigma_x^2\end{aligned}\quad (5.23)$$

Recall that the problem to be solved is Equation (5.18). This is relatively simple as the variances and covariance of the input variables n_1 and n_2 are already known.

Now, applying Equation (5.6) to Equation (5.18) (there are two input variables and only one output variable) to obtain:

$$\sigma_{z_p}^2 = \left(\frac{\partial F}{\partial n_1}\right)^2 \sigma_{n_1}^2 + \left(\frac{\partial F}{\partial n_2}\right)^2 \sigma_{n_2}^2 + 2 \frac{\partial F}{\partial n_1} \frac{\partial F}{\partial n_2} \text{cov}(n_1, n_2) \quad (5.24)$$

Calculating the partial differences:

$$\frac{\partial F}{\partial n_1} = \frac{1}{n_2}; \quad \frac{\partial F}{\partial n_2} = -\frac{n_1}{n_2^2}$$

Substituting the partial differences in Equation (5.24) and, rearranging to have:

$$\sigma_{z_p}^2 = \frac{n_1^2}{n_2^2} \left(\left(\frac{\sigma_{n_1}}{n_1}\right)^2 + \left(\frac{\sigma_{n_2}}{n_2}\right)^2 - \frac{2\text{cov}(n_1, n_2)}{n_1 n_2} \right) \quad (5.25)$$

Substituting the variances and covariances (in Equation (5.23)) into Equation (5.25):

$$\begin{aligned}\sigma_{z_p}^2 &= \frac{n_1^2}{n_2^2} \left(\frac{(r_1^2 + r_2^2 + r_3^2)\sigma_x^2}{n_1^2} + \frac{(r_4^2 + r_5^2 + r_6^2)\sigma_x^2}{n_2^2} \right. \\ &\quad \left. - \frac{2(r_1 r_4 + r_2 r_5 + r_3 r_6)\sigma_x^2}{n_1 n_2} \right) \\ &= \frac{n_1^2}{n_2^2} \underbrace{\left(\left(\frac{r_1}{n_1} - \frac{r_4}{n_2}\right)^2 + \left(\frac{r_2}{n_1} - \frac{r_5}{n_2}\right)^2 + \left(\frac{r_3}{n_1} - \frac{r_6}{n_2}\right)^2 \right)}_{M_x} \sigma_x^2\end{aligned}\quad (5.26)$$

Based on the assumption that the variances of the node points in the X direction are identical and independent of each other (although any correlation can be included in Equation (5.20)), the propagated error variance at the point P can be expressed in a similar way as for Equation

(5.13). By considering several triangular surfaces, it is found that $M_x = M(\tan \alpha_x)^2$. This is exactly the same as the solution (Equation (5.15)) derived from the geometric relation.

$$\sigma_{z_p}^2 = M_x \sigma_{x_{node}}^2 = M(\tan \alpha_x)^2 \sigma_{x_{node}}^2 = M(\tan \alpha_x \sigma_{x_{node}})^2 \quad (5.27)$$

5.5 The parameter M

It is known from Section 5.4.1 that the propagation of error variance depends on the parameters m_i ($i = 1,2,3$), which represent the influence of the error variances at each node point on the propagated error variance. For independent and identical error variances at node points, a location-dependent parameter M ($= m_1^2 + m_2^2 + m_3^2$) was derived, which combines the effects of error variances at three node points. These parameters are further explored in this section. To understand how the propagated error variance changes with location, a single triangular surface is considered. Only the propagation of vertical error variance at node points is considered since the same M is used for the propagation of horizontal error variance.

Suppose that three data points being used to build a triangular surface and their coordinates are (1,1,1), (3,1,3) and (4,4,4) (Figure 5.3(a)). The units are not given because it is not relevant to the analysis. The relative location of a particular point with respect to node points is of interest. About 10000 points, regularly distributed on the triangle surface, were considered in this analysis. The method introduced in Sections 5.4.1 was used to propagate the error variances at the nodes into points at different locations within the triangle. A single node point (i.e. (1,1,1)) was considered first. Figure 5.3(b) shows that the value of m_1 was maximal (=1) at this node point, and gradually decreased to zero with a pattern parallel to the opposite side of the triangle. It also shows the dependence of the weight m_1 on the prediction location. The actual error variance propagated into a particular point was a combination of the error variances at three node points. In the case of independent and different error variances at nodes, Equation (5.12) can be used. For a one-unit error variance at two nodes and a two-unit error variance at the third, the propagated error variance is shown in Figure 5.3(c), and is bounded by the maximum error variance at the node points (consistent with Hu et al., 2009).

In the case of independent and identical error variance, the parameter M was derived. The value of M is shown in Figure 5.3(d). The analysis showed that the minimum value of M was about 1/3 and its maximum value was about 1. The value of M reached a maximum when the point of interest was located at a node point, and was minimal when the point was at the geometric centre of the triangle. It was thought that 10000 points can reasonably represent the whole

triangle surface. On this basis, the mean value of M for the whole triangle surface was also calculated as $1/2$, which is consistent with the value given by Zhu et al. (2005). This suggested that the mean error variance ($0.5\sigma_{z_{node}}^2$) of a triangle surface could also be derived through the simple experimental method presented here. The average error variance is likely to underestimate or overestimate the error of a particular point. For a simple estimation, it is more conservative to assume that the propagated elevation error at any point in a TIN model is the same as that of the node points, namely $M = 1$. Alternatively, the procedure introduced in Section 5.4 should be used to find the exact value of M for each point of interest.

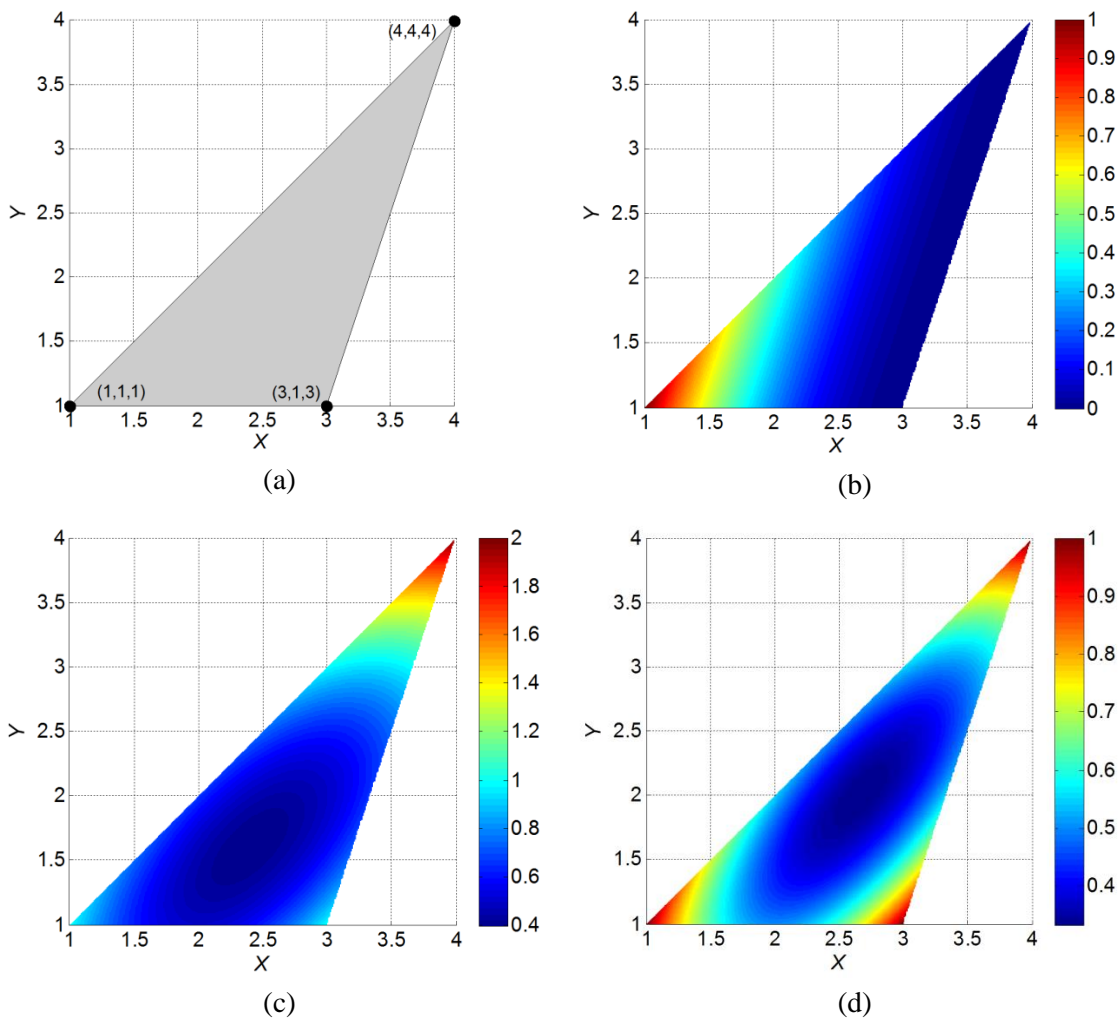


Figure 5.3: A single triangle: (a) a triangle surface created using TIN with linear interpolation based on the three node points; (b) values of m_1 ; (c) The propagated error variance in the case of different error variances at nodes (a one-unit error variance at nodes $(1,1,1)$ and $(3,1,3)$ and a two-unit error variance at node $(4,4,4)$) ; (d) values of M at different locations.

5.6 Validation

5.6.1 Monte Carlo simulation

Monte Carlo simulations were carried out to validate the results given in Sections 5.4 and 5.5. Only the cases of independent and identical error variance (represented by Equations (5.13) and (5.27)) were simulated. The 10000 points considered in Section 5.5, regularly spaced over the triangular surface, were used. In the Monte Carlo simulation, a realization of propagated errors at 10000 check points was created, by adding at each node (of a triangular surface) a random error drawn from a normal distribution. This realization was stored and this process was repeated 10000 times. For each check point, an error distribution (10000 realizations) was formed, which was then used to calculate error variances at each check point. These were carried out separately for the propagation of vertical and horizontal error variances.

It was found that the distribution of M was the same as that shown in Figure 5.3(d), with minimum, average and maximum values of about 1/3, 1/2 and 1, respectively. These results validated Equation (5.13). The simulation results also showed that the propagated horizontal error variance was almost the same as that predicted by Equation (5.27).

5.6.2 Experiments

Two experiments were carried out to further support the analytical solutions. In these experiments, the vertical and horizontal errors in the actual survey data, obtained using a terrestrial laser scanner, were considered separately. The Leica ScanStation C10 was used. The data processing and visualisation were carried out in MATLAB® (2012a) and ArcMap® 10.0

A clarification concerning the use of the survey data obtained is made here. The Leica ScanStation C10 is a short-range scanner with a high positional accuracy of a few millimetres within its useful scan range. In addition, the survey conditions were favourable (i.e. a short scan distance, sound reflectance and smooth surface of the object scanned). Therefore, the survey data obtained had an accuracy of better than 2 mm at 1σ (detailed in the following sub-sections). The survey data obtained in other cases (e.g. a long-range scan over 1 km) or from other devices (e.g. airborne LiDAR and DGPS) may have much larger positional errors. For example, the positional accuracy of individual data points obtained using long-range terrestrial scanners (over 1km) is in the magnitude of several centimetres, varying with the actual scanning distance (Leica Geosystems, 2013 and RIEGEL, 2013). The accuracy of DGPS measurements is usually about 10 - 20 mm. In this study, the ScanStation C10 was used, partly because the instrument was available.

5.6.2.1 Experiment 1: propagation of vertical error variance

A thick wooden plate was placed over an area of flat ground and levelled to avoid the effect of the horizontal measurement error on error propagation. The scanner was used to scan the plate. The data points (1237 points) acquired are shown in Figure 5.4(a). The top surface of the plate was taken as the datum-plane, i.e. zero elevation. The distribution of the elevations (i.e. vertical error) of the data points is shown in Figure 5.4(b), with one standard deviation of 1.48 mm and variance of 2.19 mm². It approximately follows the fitted normal distribution. This suggests that the vertical errors in these data points were likely to be random.

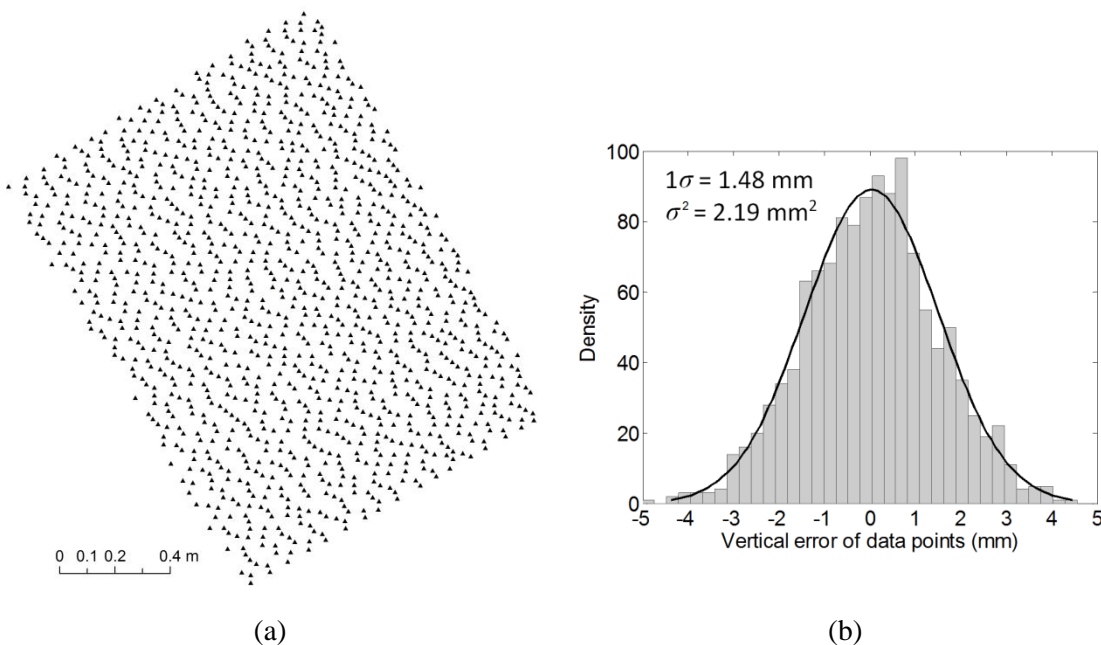
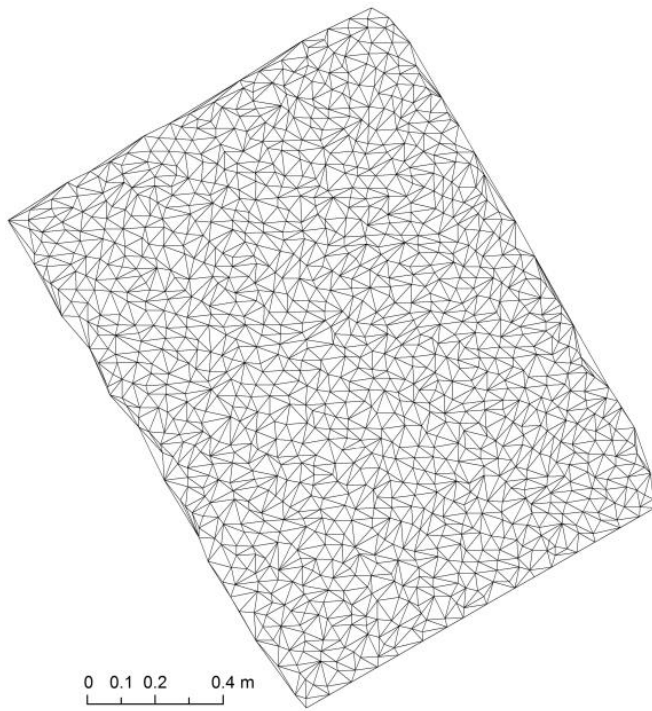
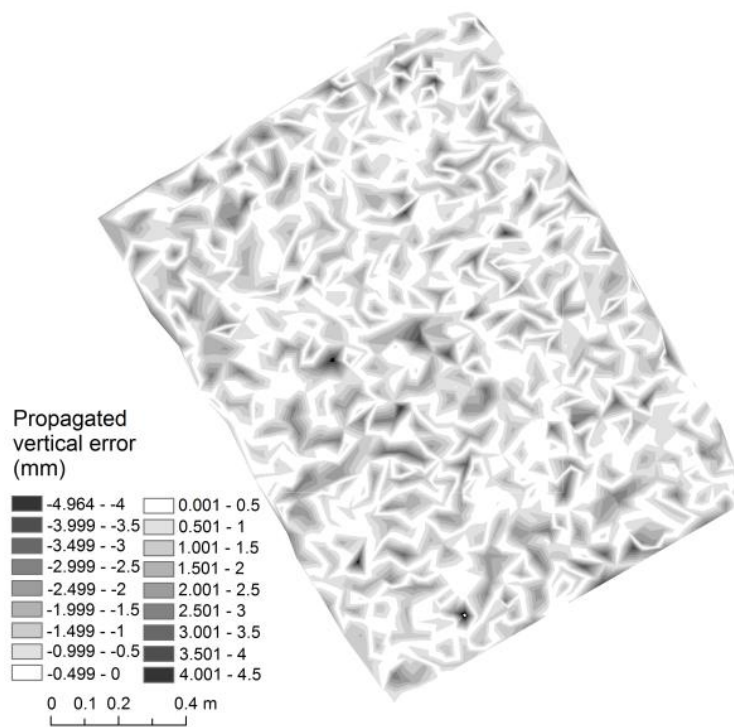


Figure 5.4: (a) TLS data points; (b) histogram of vertical error of TLS data points with normal fit

The TLS data points were used to generate a TIN (Figure 5.5(a)), which was then used to derive a fine resolution raster (2 mm) by linear interpolation. Such a fine resolution was used to show the spatial pattern of propagated error in this study. The DEMs created for practical use would not have so fine a resolution. There was no modelling error because the plate scanned was a plane. Also, as the plate was levelled, the horizontal measurement error did not affect the elevation in the DEM. Thus, the raster (Figure 5.5(b)) was a representation of propagated vertical measurement error.



(a)



(b)

Figure 5.5: (a) The TIN created from the TLS survey data; (b) a fine-resolution raster interpolated linearly from the TIN.

Chapter 5. Propagation of Measurement Errors

Figure 5.6 shows the spatial characteristics of the propagated vertical error. To better visualise the data, only a sub-area is shown in detail. The propagated vertical error varied and tended to be larger around node points. This suggests that for a grid-DEM a grid point closer to node points had a larger propagated measurement error variance. The mean error and variance of propagated error at all grid points were 0 and 1.14 mm^2 , respectively. Given that the variance of node points was 2.19 mm^2 , the average value of $M = 1.14/2.19 = 0.52$, almost the same as that (0.5) derived in Section 5.5.

It was also known from Section 5.5 that the value of M was $1/3$ at the geometric centres of triangular surfaces. The propagated vertical errors at all centroids (black dots in Figure 5.6) were extracted from the raster. The distribution of these is shown in Figure 5.7, with the standard deviation of 0.89 mm . The actual error variance and that derived using the analytical method are compared in Table 5.1. The small difference in 1σ (between the analytical method and the experiment) was probably a result of the limited number of data points used.

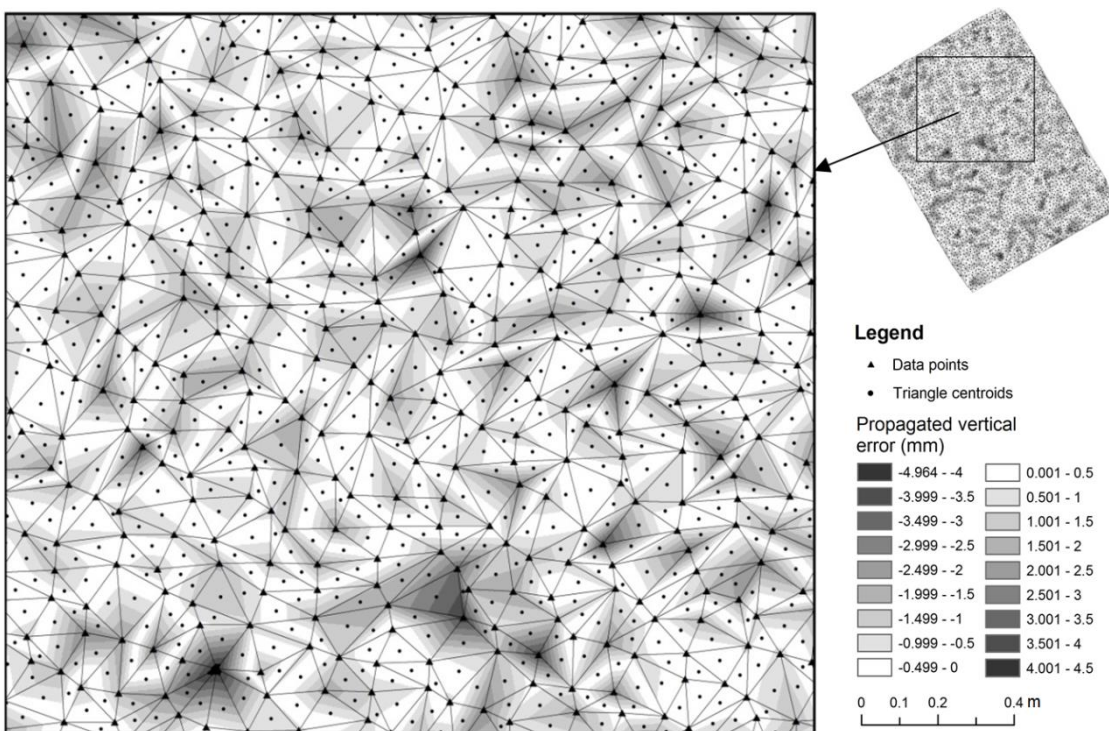


Figure 5.6: Spatial characteristics of propagated vertical error.

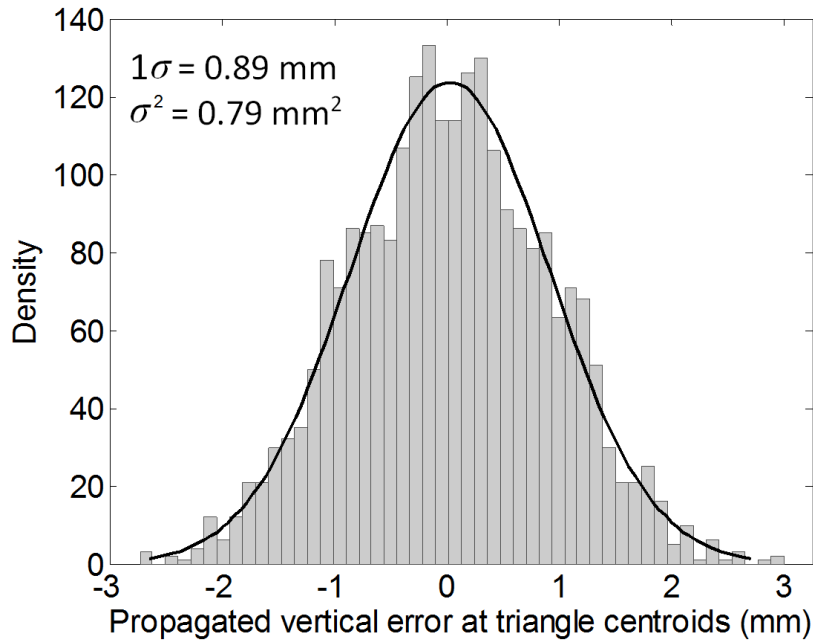


Figure 5.7: Histogram of propagated vertical error at triangle centroids with normal fit

1σ of vertical error at all node points ($1\sigma_{z_{\text{node}}}$):	1.48 mm (Figure 5.4(b))
1σ of elevation error at triangle centroids ($1\sigma_{\text{cen}}$) derived using the analytical solution (Equation (5.13)):	$\sqrt{M\sigma_{z_{\text{node}}}^2} = \sqrt{\frac{1}{3}1.48^2} = 0.86$ mm ($M = 1/3$ for triangle centroids)
1σ of elevation error at all triangle geometric centres ($1\sigma'_{\text{cen}}$) in Experiment 1:	0.89 mm (Figure 5.7)
The percentage that the values at triangle centroids in Experiment 1 lie between confidence intervals:	63.9% $[-1\sqrt{M}\sigma_{z_{\text{node}}}, 1\sqrt{M}\sigma_{z_{\text{node}}}]$; 95.4% $[-2\sqrt{M}\sigma_{z_{\text{node}}}, 2\sqrt{M}\sigma_{z_{\text{node}}}]$

Table 5.1: Propagated vertical error variance (standard deviation) at geometric centres

5.6.2.2 Experiment 2: propagation of horizontal error variance

The horizontal measurement error will cause an elevation error when the terrain surface surveyed is inclined. To investigate this, a plate with an inclination angle should be scanned. In this case, however, it is impossible to obtain the horizontal error since it cannot be separated from the vertical error. A different approach was adopted in this experiment (Figure 5.8(a)). A plate was held vertically at about the same height as the scanner. The Y axis of the laser scanner was set up by orientating the scanner to the centre of the plate. As the scanner was levelled, the

Chapter 5. Propagation of Measurement Errors

vertical direction was the Z axis. The plate was then scanned head-on. As the plate was vertical, the vertical measurement error would not cause data points to move off the plate surface in the Y direction. A plane was fitted to all data points. The distances (residuals) from the data points to the fitting plane represent the horizontal measurement error in the Y direction.

In the next step, the best fitting plane was artificially rotated to an angle of 30° with the Y axis in MATLAB[®] (2012a). The residuals (i.e. the horizontal errors) were then added back to the projected locations of the data points on the fitting plane. This process generated a new data set, which had error in the Y direction only. This new data set was used to create a TIN model, which was then interpolated into a raster (Figure 5.8(b)). Subsequent data processing was the same as for Experiment 1. It was found that $M_y = M(\tan \alpha_y)^2$. The minimum, mean and maximum values of M were $1/3$, $1/2$ and 1 . Some results are shown in Figure 5.8 and Table 5.2. The interpretation of these results is not repeated here as it is similar to that for Experiment 1.

1σ of horizontal (Y axis) error at all node points ($1\sigma_y$):	1.76 mm (Figure 5.8(c))
1σ of elevation error at triangle centroids ($1\sigma_{cen}$) derived using the analytical solution (Equation (5.27)):	$= \sqrt{M_y \sigma_y^2} = \sqrt{M(\tan \alpha_y \sigma_{y_{node}})^2} =$ $\sqrt{\frac{1}{3} \times (\tan 30^\circ \times 1.76)^2} = 0.59 \text{ mm}$
1σ of elevation error at all triangle geometric centres ($1\sigma'_{cen}$) in Experiment 2:	0.6 mm (Figure 5.8(d))
The percentage that the values at triangle centroids in Experiment 2 lie between confidence intervals:	67.4% $[-1\sqrt{M_y}\sigma_y, 1\sqrt{M_y}\sigma_y]$; 95.1% $[-2\sqrt{M_y}\sigma_y, 2\sqrt{M_y}\sigma_y]$

Table 5.2: Propagated horizontal error variance (standard deviation) at geometric centres

The results from Monte Carlo simulations and survey experiments were the same as those derived from the analytical solutions. Therefore, the analytical method proposed for vertical and horizontal error propagation was validated.

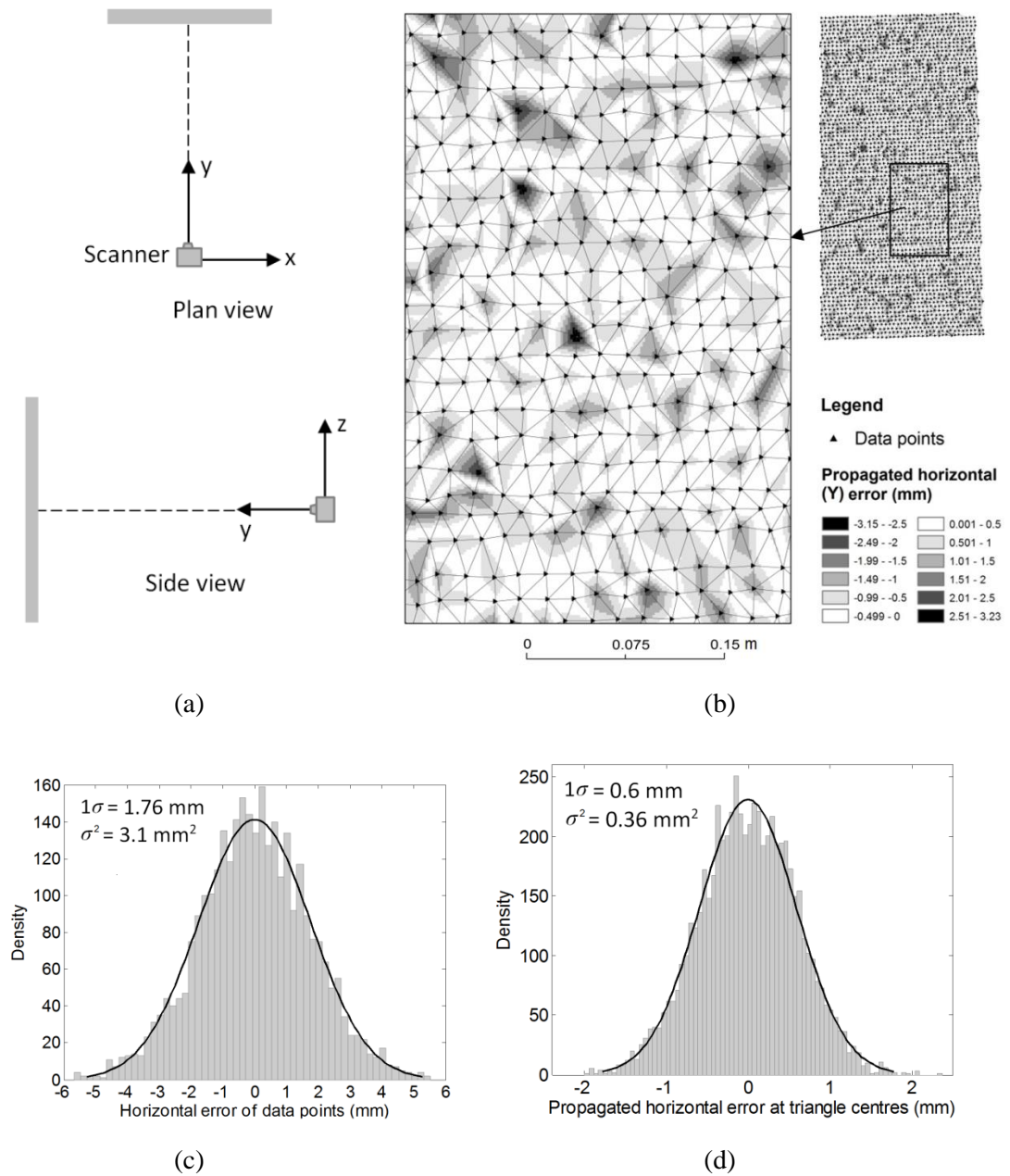


Figure 5.8: (a) experiment layout; (b) spatial characteristics of propagated vertical error; (c) histogram of vertical error of TLS data points with normal fit; (d) histogram of propagated vertical error at triangle centroids with normal fit.

5.7 Combination of vertical and horizontal error variance

In previous sections, the propagation of vertical and horizontal error variances from node points into a TIN model was studied separately. In this section, the combination of these effects is discussed. Based on the discussion in Sections 5.4.1 and 5.4.2, the propagated error variances on a TIN model are:

Effect of vertical error variance:	$M\sigma_{z_{\text{node}}}^2$
Effect of horizontal error variance in X direction:	$M(\tan \alpha_x)^2 \sigma_{x_{\text{node}}}^2$
Effect of horizontal error variance in Y direction:	$M(\tan \alpha_y)^2 \sigma_{y_{\text{node}}}^2$

These results are based on identical and independent vertical or horizontal error variances at three node points. General cases involving correlation between node points can also be considered (using Equations (5.11) and (5.20)), but are not detailed here. However, it is important to appreciate that the errors in the X, Y and Z coordinates of a single data point are likely to be correlated. This is because the coordinates (X, Y, Z) of an individual measurement point are derived from common variables, i.e. distance and angle.

There are two different ways of combining the effects of vertical and horizontal source data errors on a TIN model, depending on how these errors are assessed. An empirical approach is to compare the elevation data obtained with benchmark elevations of higher accuracy at check points. The benchmark elevations are usually acquired with another instrument of higher accuracy. A distribution of the elevation differences at these check points can then be established, which is a measure of the elevation errors at the data points. Such errors have already combined the effects of vertical and horizontal measurement errors. In this case, these errors can be regarded as “vertical” errors, and propagated into a TIN model using the propagation of vertical error variance method presented in Section 5.4.1. This approach avoids the consideration of the correlation between X, Y and Z coordinates of a single data point.

Another possibility is that the positional (vertical and horizontal) errors of measurements are already known from a technical specification, theoretical calculation or control experiments. In this case, the propagation of horizontal and vertical source data errors is required. The correlation between X, Y and Z coordinates of a single data point needs to be assessed. The actual correlation may vary from one case to the other, depending on how a data point is derived, and may not be zero. For example, the X, Y and Z coordinates of a data point obtained from a terrestrial laser scanner are calculated from the range and angle measurements. Therefore, these coordinates are correlated. If the error variances are assumed to be independent of each other (unlikely to be the case in practice), the error variance at a particular point *P* can be expressed as:

$$\sigma_{z_p}^2 = M \left(\sigma_{z_{\text{node}}}^2 + (\tan \alpha_x)^2 \sigma_{x_{\text{node}}}^2 + (\tan \alpha_y)^2 \sigma_{y_{\text{node}}}^2 \right) \quad (5.28)$$

$$(1/3 \leq M \leq 1)$$

If the correlation is known or can be assessed, Equation (5.28) should be modified to include the influence of the correlation. A detailed discussion of this is outside the scope of this chapter as the nature of the correlation depends on the techniques used to acquire data points. However, it is possible to determine the correlation between X , Y and Z coordinates if the algorithm used to derive these coordinates is known. Alternatively, the error propagation can be based on the worst case scenario, which depends on the significance of the influence of the error variance in each direction.

5.8 Discussion

Error propagation reflects the effect of uncertainties in input variables on the uncertainty of an output variable based on some functions of the inputs. The well-known error propagation method has been used to derive the analytical solution. The weight m_i represents the influence of the error variance of an individual node point on the propagated error variance at a particular point. Its value gradually decreases from one at the i^{th} node point to zero on the opposite side of the triangle surface. In the case of identical and independent error variances at nodes, Equations (5.13) and (5.27) were derived to calculate the propagated error variance at any particular points. It was found that the propagated error variance of a particular point varied with its relative location to the node points enclosing it. This variation depended on the parameter M introduced, which was essentially the location-dependent weighting for error variances at node points. The value of M for a point other than the geometric centre and nodes lay between $1/3$ and 1 . A greater propagated measurement error variance resulted when the point was closer to either of the three node points. This is consistent with the classical statistical theory, in which the propagation of measurement error at all points is a weighted average of the errors at node points.

Some GIS operations (e.g. a comparison of multi-temporal DEMs) require interpolation at particular points. In such cases, the uncertainty of a particular point should be considered. The method introduced in this study provides a means of assessing the elevation error of any point propagated from node points. On this basis, the elevation error variances at the grid points of a raster DEM can be evaluated. The analysis in this study suggests that the average error variance is likely to be an under- or over-estimate of the actual error variance at a particular point. If an error propagation analysis is not carried out, it is more conservative to assume that the error variance in a TIN model is the maximum error variance of node points.

Chapter 5. Propagation of Measurement Errors

The horizontal errors at node points were studied. Their effects on the elevation at a particular point were found to depend on the slope angles with respect to the X and Y axes. The larger the slope angles, the greater the propagated error variances. When the slope angle is greater than 45° , the effect of the horizontal errors of source data points on the predicted elevation of a particular point P is greater than that of a vertical error of the same magnitude. The slope angle can either be determined by a slope map or from triangular surfaces directly.

In cases where data points are extremely dense and the point spacing approaches the horizontal error of data points, the interpolation point is relatively likely to lie within a different triangular facet. Because of discontinuities in slope along the sides of these facets, error in the interpolated height could be greater than if the interpolation point occurs within the same facet. As the horizontal error in real survey data points is usually much smaller than the point spacing, this is considered a minor issue in practice, and is beyond the scope of this chapter.

Although a special case of equal error variances and zero covariance is discussed in detail, a generic solution (Equation (5.11)) has been derived for propagation of vertical error variance. Also, a generic solution for propagation of horizontal error variance can readily be derived from Equation (5.20) (simply following the same procedure as Equations (5.22)-(5.25)), by using appropriately different error variances and covariances between node points. Therefore, the solutions provided in this chapter can be used to assess the propagated source data errors at a particular point when the uncertainties at node points are different and dependent.

Two approaches to combine the effects of vertical and horizontal measurement errors were presented. These errors can be combined as an elevation error through empirical assessment at check points. If these elevation errors are regarded as a representative of the measurement error at node points, only the method proposed for propagation of vertical error is required. If the horizontal and vertical errors at node points can be evaluated separately or are known from specifications, an understanding of their correlation is required.

The results of the survey experiments carried out in this study show that the method is of practical application to topographical survey data. If the error variances at data points are known, the error propagation can be implemented in the following main steps: (i) generate a TIN with a reference number assigned to each triangle formed in the triangulation process; (ii) identify points of interest within the TIN model, i.e. the particular points described in earlier sections. These can be the grid points of a raster-based DEM; (iii) match each point of interest to the relevant triangle which encloses the point (there are several ways (e.g. Hormann and

Agathos, 2001) to determine whether a point is within a triangle); (iv) apply the analytical solution.

5.9 Summary

In this chapter, an analytical solution was derived to calculate the error variance of any point within a linearly interpolated TIN model due to vertical and horizontal error variances in the source data (node points). The solution was validated against real survey data obtained using a terrestrial laser scanner. The propagated error variance depended on its relative location with respect to the relevant three node points that form a triangular surface. For the error variance of a single node point, its effect was maximal at this node point and gradually decreased to zero with a unique pattern (parallel to the opposite side of the triangle surface).

The error propagation solutions in Equations (5.13) and (5.27) were based on identical and independent error variances at node points. A location-dependent parameter M was derived. The maximum, average and minimum values of M were 1 (when the point was at one of node points), $1/2$ and $1/3$ (when the point was at the geometric centre of a triangle). The average error variance ($0.5\sigma_{z_{\text{node}}}^2$) overestimated or underestimated the actual propagated error variance at a particular point (except for the case where the error variance at some points was just half that at node points). The propagated error variances were greater when the particular point was closer to one of the node points. This was consistent with the expectation using classical statistics. More general cases can be considered, in which the error variances at node points are different and dependent (see discussion in Section 5.8).

The effect of horizontal error at node points depended on the actual slope angles with respect to the X and Y axes. The propagation of horizontal error variance can be carried out in a similar way to the vertical error variance.

This chapter, as its title suggests, addresses the propagation of error variances from source data points; it does not address interpolation uncertainty. However, the accuracy of a DEM also depends on interpolation uncertainty, which reflects how well the interpolated elevation model approximates the real physiography (Shortridge, 2001; Fisher and Tate, 2006). The interpolation errors are discussed in Chapter 6.

Chapter 6 :

DEM Accuracy

6.1 Introduction

Although it is possible to compare multi-temporal point clouds directly for deriving surface deformations, it is common practice to compare multi-temporal digital elevation models (DEMs) constructed from point clouds. This chapter provides a brief introduction on how to create a digital elevation model (DEM). The method of evaluating DEM accuracy is presented and discussed. The main factors affecting DEM accuracy are investigated, including interpolation methods, data densities and the roughness of terrain surfaces.

6.1.1 Digital elevation models

A DEM is a digital representation of a part of the Earth's surface. It forms a basic input to many GIS-related tasks and has a wide variety of applications, such as mapping, terrain analysis and environmental modelling (Webster et al., 2006; Chen and Zhou, 2013; Brunori et al., 2013). Two major categories of DEMs are used widely to represent a terrain surface, i.e. vector-based DEMs and grid-based DEMs (Zhu, et al., 2005). The former usually refers to a triangulated irregular network (TIN). The grid-based DEMs represent elevations in a raster or grid framework, which can be used to calculate many elevation surface variables such as slope and flow direction (Wechsler and Kroll, 2006). An important difference between a TIN and a grid DEM is that the former preserves the original source data.

Historically, the source data used for the generation of DEMs have most frequently come from contour lines, paper maps and imagery such as stereo aerial photographs (Fisher and Tate, 2006, Zhu et al., 2005). Imagery from various platforms still represents a popular source of data with which to construct DEMs (e.g. Gessesse et al., 2010; Fonstad et al., 2013). Point measurements acquired directly from land surveying were less frequently used to create DEMs in the past (Fisher and Tate, 2006). However, point measurement sources have become increasingly

popular in recent years since DGPS and laser scanning systems (Lloyd and Atkinson, 2006; Negishi et al., 2012; Gallay et al., 2013) have come to be used widely.

To create a grid-based DEM or predict the elevations at the locations where no source data are available, spatial interpolation is commonly used. A wide variety of interpolation methods are available, which are either deterministic or geostatistical. In addition to a TIN with linear interpolation described in Section 5.2, this section introduces another three simple interpolation methods: inverse distance weighting (IDW), moving average (MA) and global/local polynomial regression. It is common for GIS designers to use relatively simple and straightforward interpolation methods to speed up execution and simplify the decision process for users (Kyriakidis and Goodchild, 2006). When the density of the source data is high, there is little justification for employing a more complex interpolation method (Lloyd and Atkinson, 2006).

Inverse distance weighting (IDW)

IDW predicts a value for an unmeasured location using a weighted average of its neighbouring data points, with the weight dependent on the distances from the neighbouring data points to the prediction location. A general form of the IDW method is given below:

$$z(x) = \frac{\sum_{i=1}^N w_i(x)z_i}{\sum_{j=1}^N w_j(x)}$$

A simple definition of the weight w_i is:

$$w_i(x) = \frac{1}{\text{dis}(x, x_i)^p}$$

where $z(x)$ is the elevation predicted at an unmeasured location x based on its neighbouring data points $z_i = z(x_i)$ for $i = 1, 2, \dots, N$ (the number of data points); $\text{dis}(x, x_i)$ is the distance from the i th data point to the interpolated location; p is the weight/power parameter.

Moving average (MA)

The elevation interpolated at an unmeasured location is set to equal the arithmetic mean of the elevations of its neighbouring data points selected by a search window. In other words, the same weight is assigned to every data point. It is a special case of the IDW method (when the power $p = 0$).

Global or local polynomial regression (GPR/LPR)

Global polynomial regression fits a smooth surface to all the data points over the domain of interest. The surface is defined by a polynomial function. Local polynomial regression operates in the same way but fits to the data points within a local area determined by a search radius. To represent the whole surface, a separate polynomial function is required for each local area. The global or local polynomial functions are used to interpolate the elevation at an unmeasured location. The general forms of linear and quadratic polynomial functions are given below.

$$F(x, y) = a + bx + cy \quad \text{– Linear (1st order polynomial)}$$

$$F(x, y) = a + bx + cy + dxy + ex^2 + fy^2 \quad \text{– Quadratic (2nd order polynomial)}$$

where (x, y) is the location of data points; a, b, c, d, e and f are polynomial coefficients.

6.1.2 DEM accuracy descriptor

Evaluation of the accuracy of a DEM is an essential part of DEM production. There are two error components associated with DEMs. These are: (i) errors in the individual data points that are used to build digital elevation models, and (ii) interpolation errors. A combination of these two components gives a measure of DEM accuracy. The uncertainty in grid points of a DEM can be represented by the following equation.

$$\delta Z = Z_{\text{DEM}} - Z_{\text{true}}$$

where Z_{DEM} represents the elevation measured from the DEM; Z_{true} represents the true elevation on the terrain surface; δZ is the error.

However, it is impossible to quantify the error (δZ), as the true elevation (Z_{true}) is unknown. In practice, the benchmark (reference) elevations obtained with another instrument of higher accuracy (than those measured from DEMs) are usually used (e.g. Hodgson and Bresnahan, 2004; Su and Bork, 2006; Heritage et al., 2009). Also, it is not practical to obtain the benchmark elevations at every location of a DEM. Hence a limited number of check points are used.

The most commonly used measure of DEM accuracy is the root mean square error (RMSE) (Li, 1988; Desmet, 1997; Hunter and Goodchild, 1997). It is a single global statistic per DEM based on comparison with some reference points (Fisher and Tate, 2006). The mean error (ME) can be used to check if systematic under- or overestimation of elevations exists in DEMs. If the ME is

Chapter 6. DEM Accuracy

(or is assumed to be) zero, the RMSE is equal to the standard deviation of the error (SD). The formulae of these statistical descriptors are given in Table 1.1.

DEM accuracy is influenced by several factors, such as the characteristics of a terrain surface, the density of survey points, and interpolation methods. Much research has been carried out to assess the quality of a DEM and investigate the effects of different factors on its accuracy (e.g. Kyriakidis et al., 1999; Lloyd and Atkinson, 2002; Aguilar et al., 2005; Erdogan 2009; Bater and Coops, 2009; Hu et al. 2009; Heritage et al., 2009). The effects of DEM accuracy on other GIS variables (e.g. slope and aspect) were also investigated (Oksanen and Sarjakoski, 2005; Wechsler and Kroll, 2006). A comprehensive overview of the causes and consequences of error in DEMs can be found in Fisher and Tate (2006).

6.1.3 Knowledge gap

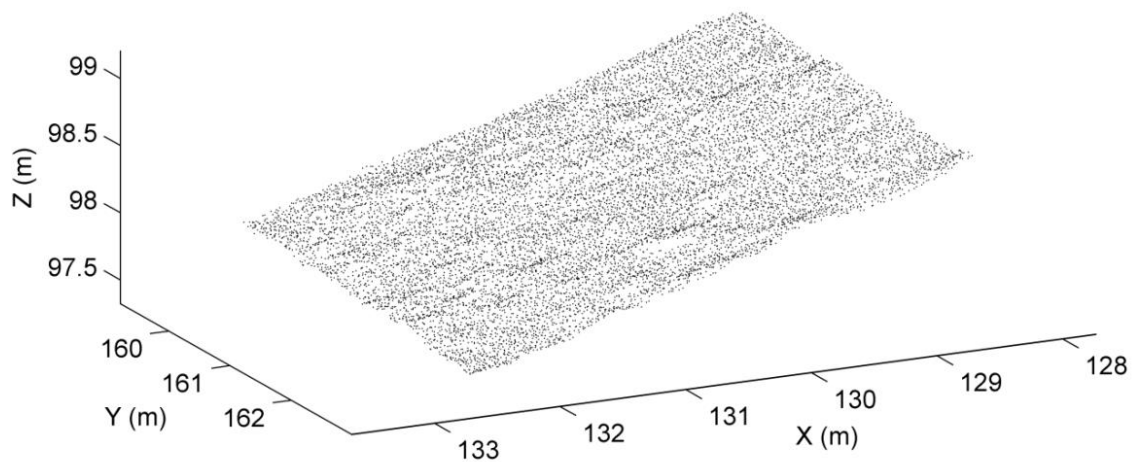
Previous research has usually focused on large sites and survey data of much lower density than that of a TLS dataset. The DEM errors reported were mostly hundreds of millimetres or more. The accuracy of DEMs created with the TLS data representing a local site (e.g. an engineered slope) is not well understood quantitatively; this is the focus of this chapter. As the effects of vegetation on DEM accuracy have been discussed in Chapter 4, only the TLS data representing bare ground surfaces are considered in this chapter.

6.2 Study data

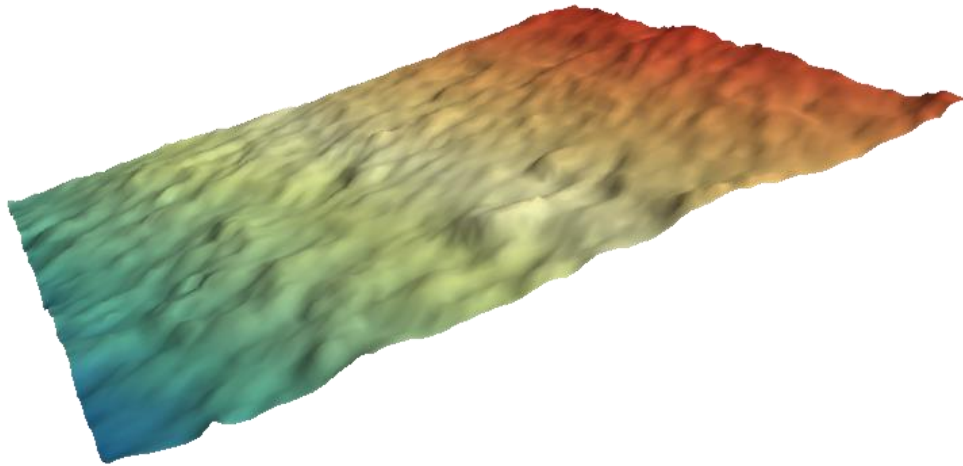
6.2.1 An engineered slope

The slope chosen was a cutting on the A34 Newbury bypass in southern England. The slope is east facing, 8 m high and 28 m long. The cutting was constructed in 1997, and is entirely within the London Clay. The vegetation on the slope was mainly grass of various depths at the time the surveys were carried out. The overwhelming majority of grass in the upper part of the slope was trimmed to the ground level before scans took place. As it was difficult to clear every individual grass leaf, some remained at scattered locations.

The point clouds representing the upper part (3.8 m by 4 m) of the slope were extracted from Cyclone® 7.3 and then imported into MATLAB® (R2012a) where a lowest point filter (introduced in Section 4.3.2) was used to remove any remaining grass leaves at scattered locations. The post-filtered point cloud is shown in Figure 6.1(a), which had an average point density of 870 points per metre square. The characteristics of the surface variation of this subarea are visualised in Figure 6.1(b).



(a)



(b)

Figure 6.1: (a) The point cloud representing the upper part of the Newbury cutting; (b) a visualisation of its surface characteristics.

As a trend existed in the terrain surface (a slope angle of approximately 16°), it was detrended using a bilinear polynomial regression to show the elevation residuals in Figure 6.2(a). The distribution of the elevation residuals was almost normal, with the standard deviation of 20.7 mm (Figure 6.2(b)).

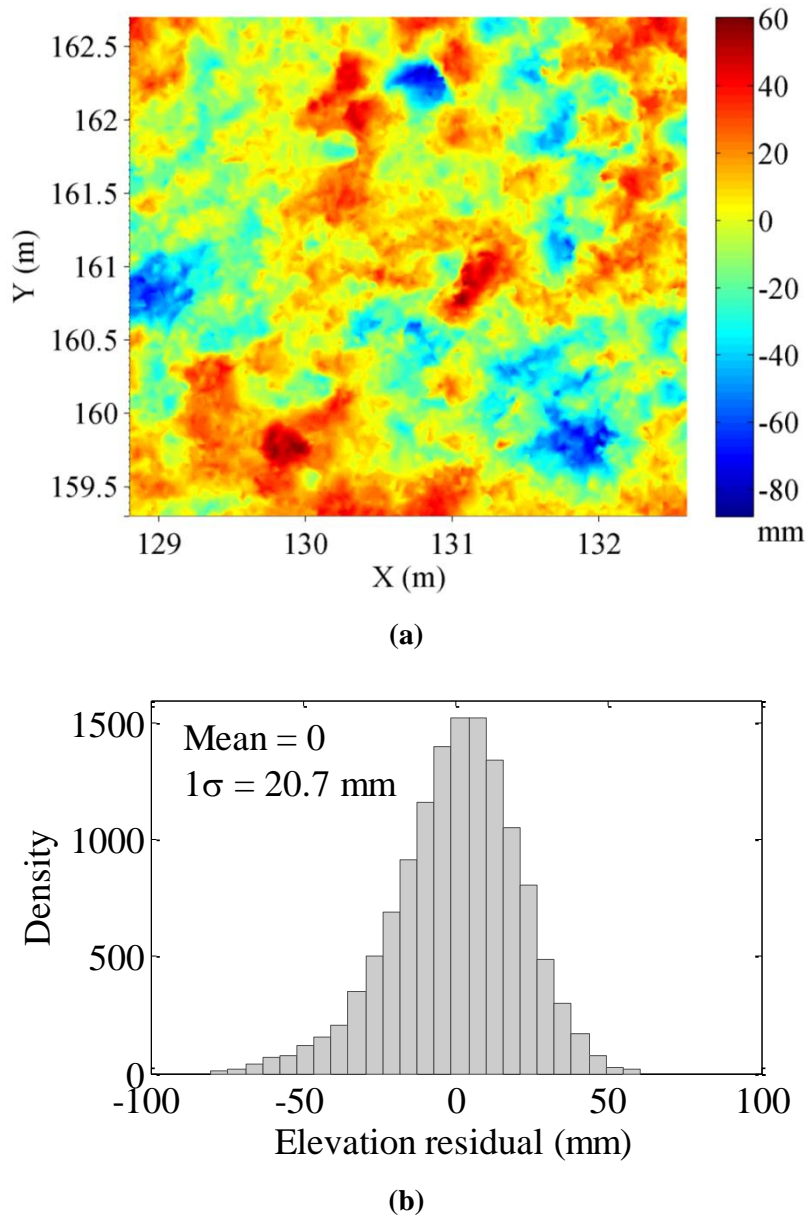


Figure 6.2: (a) The elevation residuals; (b) the histogram of the elevation residuals.

6.2.2 Other types of surfaces

To investigate how the characteristics of local terrain surfaces may affect the DEM accuracy, two additional TLS survey data were considered, representing a subarea (4 m by 4 m) of a smooth and flat sandy surface in a beach environment and a subarea (roughly 15 m²) of a rough coastal landslip surface, located on the South-West coast of the Isle of Wight. The landslide surface scanned is a part of a large landslide complex comprising a series of gently slumped blocks of earth mixed with fine gravels. The Leica ScanStation C10 was used. The scanner was placed in front of the landslide surface from where a high resolution scan was carried out. The TLS data representing these two surfaces are shown in Figure 6.3(a) and Figure 6.3(b), respectively.



(a)



(b)

Figure 6.3: The point clouds representing: (a) a smooth and flat sandy surface; (b) a part of a rough landslip surface.

There may be another type of surface, which is smooth but has a spatial variation signal. As no survey data were available for this, a semi-artificial surface was created. The point cloud representing the Newbury cut was smoothed using a local polynomial regression of order 2. This processing was used to remove the noise of spatial variation and the noise of measurement, and resulted in a new point cloud.

Most terrain surfaces have spatial variations of different scales. The scale of spatial variation that can be detected by a remote sensing technique depends on its spatial resolution of a single measurement (e.g. a few millimetres for a short-range terrestrial laser scanner; a few metres for

interferometric synthetic aperture radar). The spatial variations that can be observed from a remote sensing dataset also depend on the data sampling resolution (Atkinson and Foody, 2002). In this study, the spatial variation of a terrain surface was classed into two categories with the following definitions:

- Signal (of spatial variation): the surface variation that is detectable with TLS.
- Noise (of spatial variation): the small surface variation that is not detectable with TLS.

The signal and noise of spatial variation combine to describe the characteristics of a terrain surface. The observed characteristics of the four surfaces are summarised in Table 6.1.

Surfaces	Signal of spatial variation (comparatively)	Noise of spatial variation (comparatively)
Engineered slope surface	Strong	High level
Smoothed engineered slope surface	Strong	Almost no
Sandy surface	Almost no	Low level
Landslip surface	Strongest	Highest level

Table 6.1: The characteristics of the four surfaces considered.

6.3 Method

The method commonly used for assessing DEM accuracy was briefly presented in Section 6.1.2, in which check points of much higher accuracy are used. As a terrestrial laser scanner is an accurate instrument (discussed in Chapter 3), check points of higher quality are usually not available. Therefore, it would be difficult to use the conventional method for assessing the accuracy of DEMs created from TLS data. In this study, statistical resampling experiments are used as a suitable alternative for DEM quality assessment.

Statistical resampling techniques such as cross validation have been used to evaluate the relative accuracy of different interpolation methods (e.g. Aguilar et al., 2005; Erdogan, 2009; Páquet, 2010). In the simplest form of statistical resampling, subsamples are drawn from the full sample, and then analysed to estimate the standard errors (e.g. the RMSE used in this study) of a population parameter or a prediction.

In the context of DEM accuracy assessment, the subsamples selected are essentially the check points. However, these check points are subject to the same nature of positional error as the data points left for interpolation. Researchers (e.g. Aguilar et al., 2005, 2006; Erdogan, 2009) have assumed that the check points (i.e. subsamples) were free of error, to enable a study on how well different interpolation methods could represent a terrain surface. This assumption is reasonable for the case where the interpolation error is much larger than that of the check points.

Because of the high density of TLS data points, the interpolation error could be as small as the positional error in individual data points. As a result, the assumption stated in the last paragraph may not hold. However, this assumption is not necessary for assessing the accuracy of DEMs created using TLS data points. Errors in DEMs are a combination of the measurement error in source data points and the interpolation error. The former has been investigated in Chapter 5. In resampling experiments, these two error components have been included in a conservative way, because the check points are also contaminated with measurement errors. In this study, it is assumed that the results obtained from the statistical resampling experiments are a reasonable representation of the DEM error in this study.

The point cloud representing the engineered slope was used to demonstrate how to carry out statistical resampling experiments. The procedure of these experiments is illustrated with a flowchart in Figure 6.4, accompanied by a detailed description of the steps.

- Step 1: $N = 100$ check points were randomly selected from the original point cloud ($M = 13045$), constrained with a minimum distance of 300 mm between individual check points to have an even point distribution. The elevations (Z_{REF}) of these check points were used as the reference elevations at the check point locations. These check points were excluded from the original point cloud. The number of data points remaining in the point cloud is 12945.
- Step 2: The data point density was reduced by randomly removing P data points from the point cloud containing 12945 points.
- Step 3: Interpolation methods were used to predict the elevations (Z_{DEM}) at the check point locations, based on the point clouds of reduced density.
- Step 4: Z_{REF} and Z_{DEM} were compared.

The experiments started with an initial reduction of $P = 505$ data points. Steps 1 - 4 were run $i = 25$ times for this initial point reduction. Once completed, another reduction of more data points ($P = 3396$) was carried out. Steps 1 - 4 were repeated 25 times again for the second reduction. This process continued with density reduction steps shown in Table 6.2.

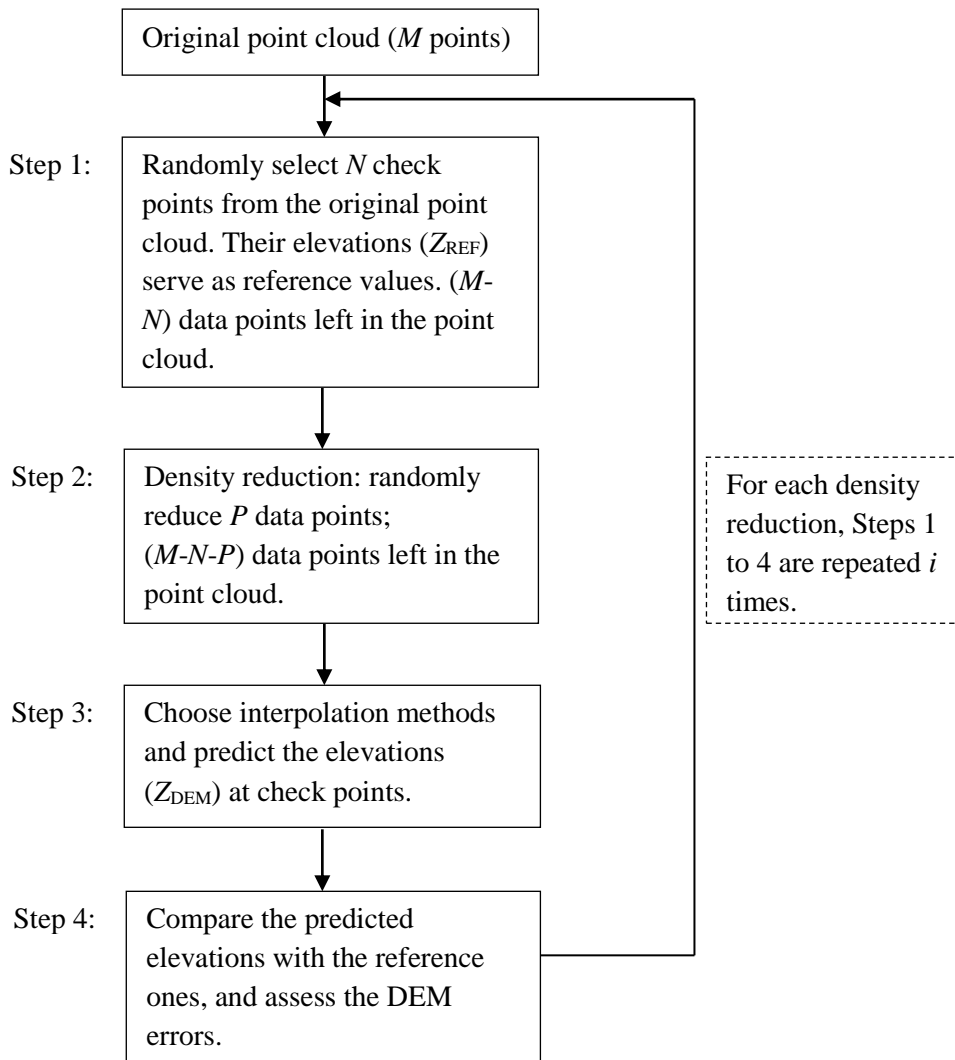


Figure 6.4: Flowchart of the resampling experiments used to assess DEM accuracy.

Six statistical resampling experiments were carried out for the TLS data representing the engineered slope. The interpolation methods and the associated parameters are provided in Table 6.3. Resampling experiments were also carried out for other types of surfaces, in which only the TIN with linear interpolation was used. These experiments were implemented in MATLAB® (R2012a).

Data points to be removed in each reduction (P)	Data points left for interpolation ($M-N-P$)	Data points left in percentage	Number of points left per metre square	Equivalent spacing of data points left (mm)
505	12440	95%	831	35
3396	9549	73%	638	40
5380	7565	58%	505	45
6802	6143	47%	410	50
7855	5090	39%	340	55
8657	4288	33%	286	60
9282	3663	28%	245	65
9778	3167	24%	212	70
10180	2765	21%	185	75
10508	2437	19%	163	80
10781	2164	17%	145	85
11010	1935	15%	129	90
11204	1741	13%	116	95
11369	1576	12%	105	100

Table 6.2: Data density reduction steps.

Experiments	Description
TIN	Triangulated irregular network
MA (8points)	Moving average using 8 closest neighbouring data points
IDWp1 (8points)	Inverse distance weight with a power of $p = 1$ using 8 closest neighbouring data points
IDWp2 (8points)	Inverse distance weight with a power of $p = 2$ using 8 closest neighbouring data points
IDWp2 (20points)	Inverse distance weight with a power of $p = 2$ using 20 closest neighbouring data points
LPR (20points)	Local polynomial regression (quadratic) using 20 closest neighbouring data points

Table 6.3: The interpolation methods and the associated parameters.

6.4 Results

6.4.1 The engineered slope

Figure 6.5 shows that for different experiments the mean errors at various point densities were very small. Hence there was no systematic under- or overestimation of elevations. The RMSE for different experiments is shown in Figure 6.6 and Figure 6.7. The results in these two figures are the same but are plotted against two different means of representing point densities, i.e. the number of data points per metre square and the equivalent point spacing. As the mean error was about zero (Figure 6.5), the RMSE in this case was roughly equal to the standard deviation of the interpolation error. Hence the RMSE reported in Figure 6.6 and Figure 6.7 has a confidence interval of 1σ .

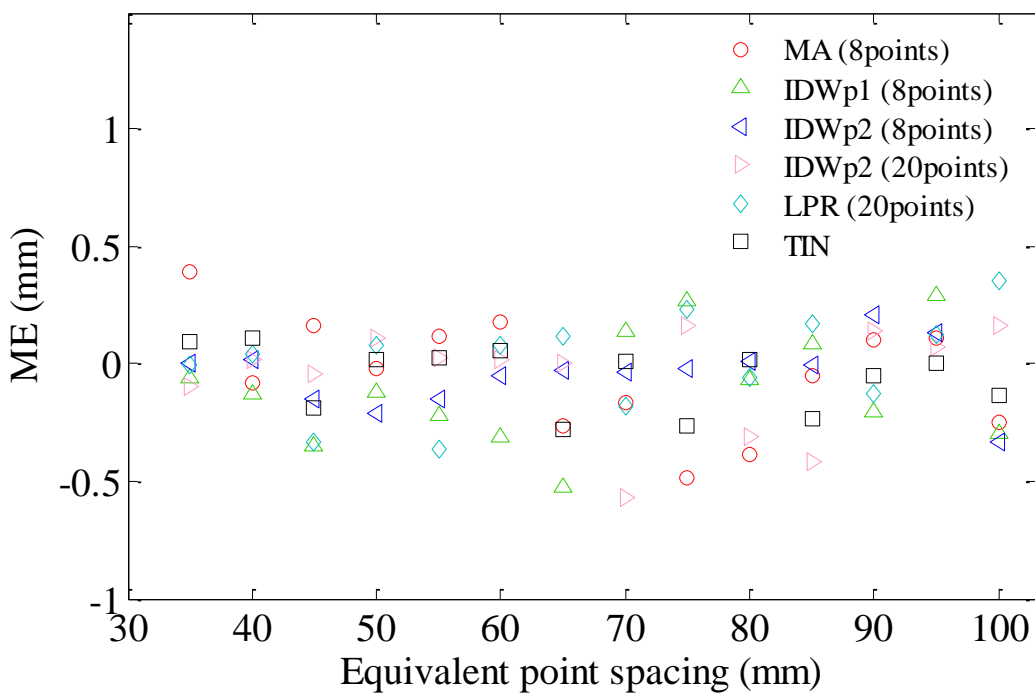


Figure 6.5: The mean errors for different equivalent point spacings and different interpolation methods.

For all the interpolation methods considered, the DEM errors increased as the data point density decreased, consistent with the results of others (Aguilar et al., 2005; Bater and Coops, 2009; Páquet, 2010). Amongst these, the TIN and the local polynomial regression were most accurate while the moving average had the least accurate results. The IDW was not very sensitive to the interpolation parameters used; the differences in RMSE were small when a different power or number of neighbouring points was used. The performance of these interpolation methods started to become more distinct as the point density decreased.

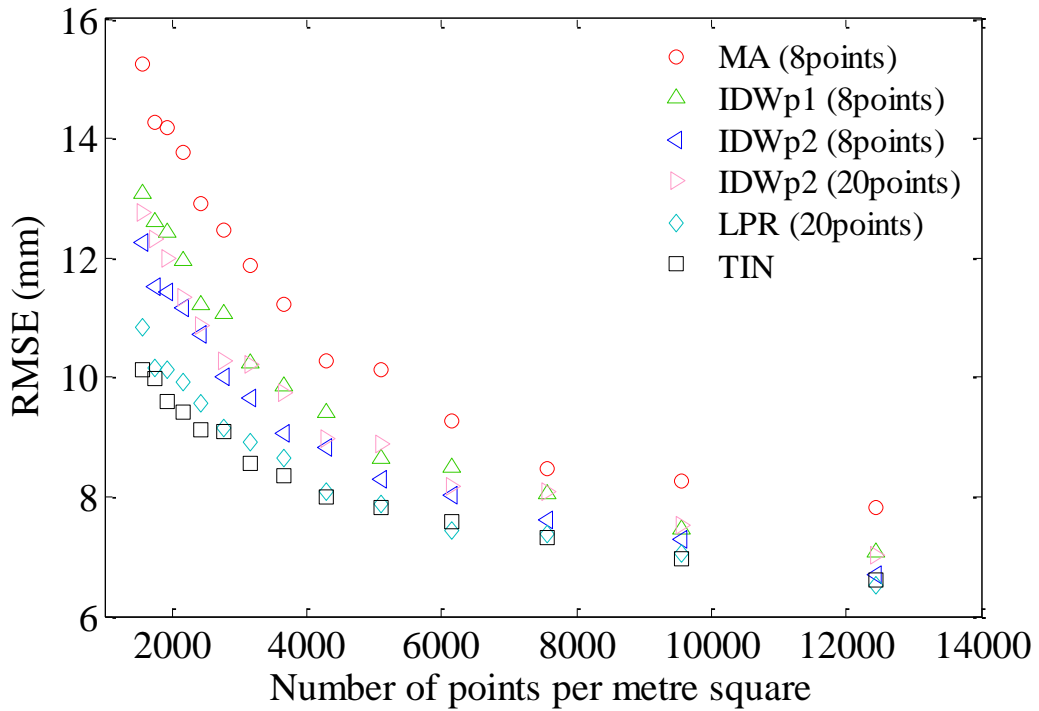


Figure 6.6: The RMSE for various point densities (represented by the number of points per metre square) and different interpolation methods.

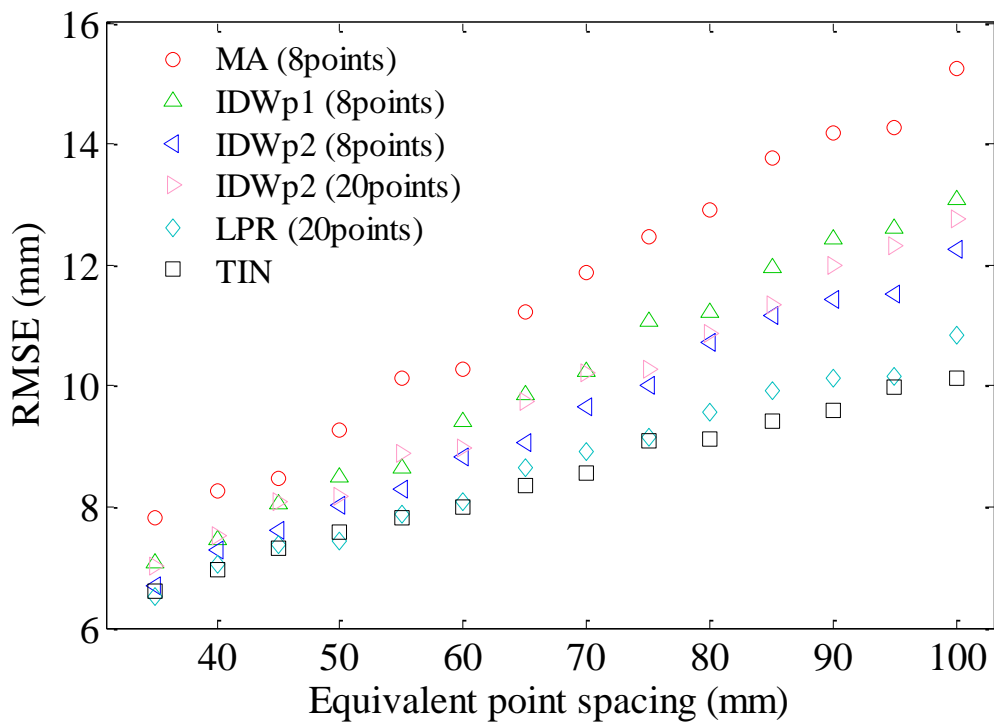


Figure 6.7: The RMSE for different equivalent data point spacings and different interpolation methods.

The TIN with linear interpolation was an accurate interpolator for the engineered slope surface considered, and was chosen for further discussion. A linear regression line (Figure 6.8) was used to fit the RMSE at various data densities, having a slope of 0.054 and an intersection of 4.8 mm with the vertical axis. To better understand this relation, the RMSE were divided into two parts: (i) a point-spacing dependent part (i.e. $0.054 \times \text{spacing}$) and (ii) a constant part (i.e. 4.8 mm). This classification was based on the assumption that the linear relation was still valid for the equivalent point spacings smaller than 30 mm. However, this may not be the case for all types of terrain surfaces. As the point spacing approaches zero, a concavity pattern may occur near the origin, depending on the local smoothness of a terrain surface. The RMSE is likely to plateau when the point spacing becomes very large because it is constrained by the population variance of the detrended elevation residuals shown in Figure 6.2. Nevertheless, the linear fit is reasonable for the range of spacing (35 mm – 100 mm) in this case study.

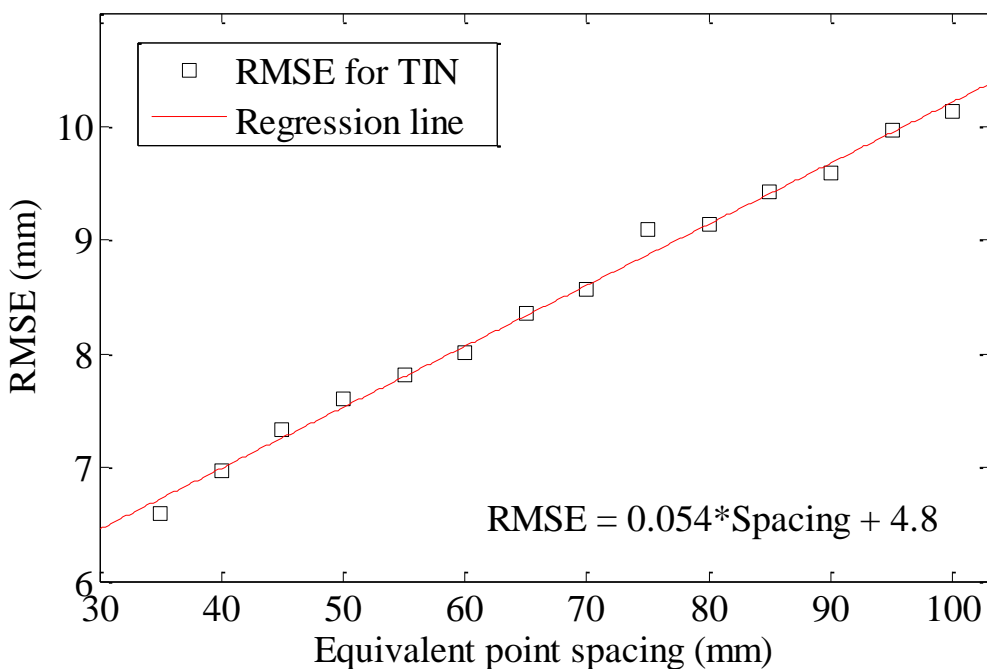


Figure 6.8: The least-square fit of the RMSE at various point spacings for the TIN model.

The point-spacing dependent part depended on the signal of spatial variation (defined in Section 6.2.1). A higher sampling density would capture the signal in more detail and hence reduce the DEM error. The constant part was caused mainly by the noise of spatial variation and the noise of measurement. As these noises were likely to be spatially random, a further increase in sampling resolution would not reduce this part.

6.4.2 Other types of surfaces

The mean errors were also about zero for the other surfaces considered. The DEM accuracy in terms of RMSE is shown in Figure 6.9. The differences in RMSE suggest that the surface characteristics could significantly influence DEM accuracy.

Table 6.1 shows that the rough landslip surface had the strongest signal and the highest level of noise amongst all the surfaces considered. The results shown in Figure 6.9 were consistent with these surface characteristics. The fitted line had the steepest slope (0.091), suggesting that the signal of its spatial variation is stronger than that of the other surfaces. The noise part (6 mm) for the landslip surface was also the largest. The RMSE for the sandy surface was very small (< 2 mm at 1σ) and depended mainly on the noise of measurement. This suggests that TLS can be used to reconstruct a smooth and regular surface with a very high accuracy.

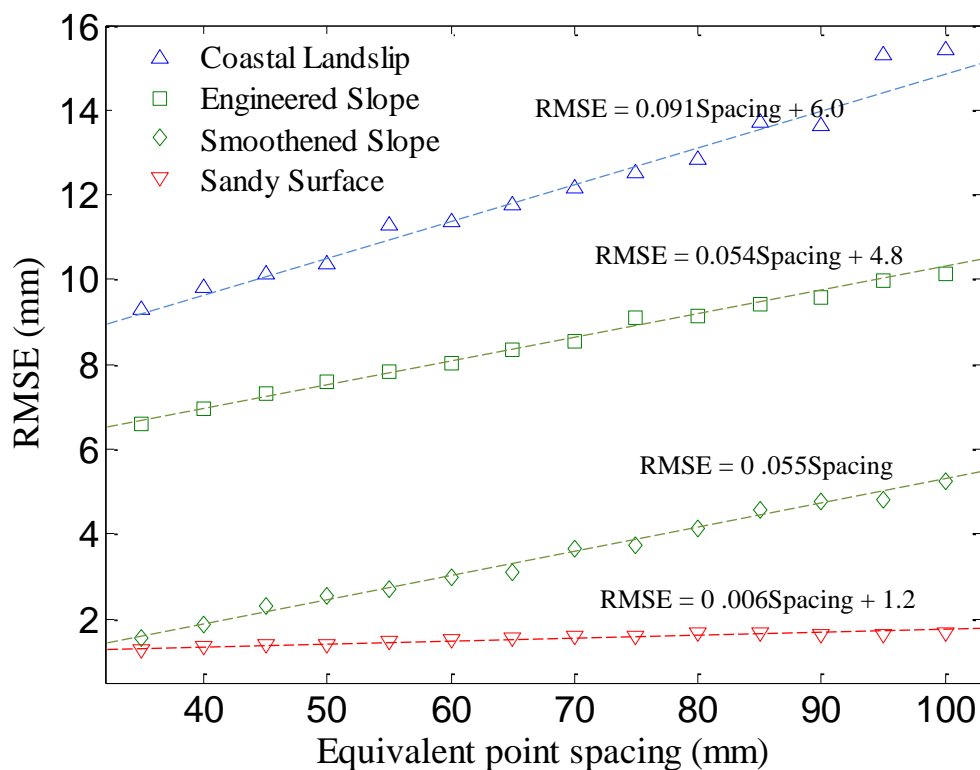


Figure 6.9: The RMSE for terrain surfaces of different characteristics (the TIN with linear interpolation was used).

The increases of RMSE with increasing point spacing for the original and smoothed engineered slope surfaces were parallel, confirming that the signal of spatial variation had been successfully preserved. For the smoothed slope surface, the RMSE was very small (< 2 mm at 1σ) for point spacings smaller than 40 mm, suggesting that it is possible to use high-density TLS data to accurately model a smooth terrain surface of some signals. It also indicates that noises of spatial

variation and measurement were a major contributor to the RMSE for the (original) engineered slope surface, especially when the data density was high.

6.5 Discussion

The point spacing considered in this study varied from 35 mm to 100 mm because it would not be difficult for a close range terrestrial laser scanner to survey a terrain surface with a finer sampling resolution than 100 mm. However, other spacings can also be investigated using the statistical resampling method introduced.

As it would be difficult to obtain benchmark points of higher accuracy than TLS measurements, the assessment of DEM accuracy was based on the check points selected from TLS survey data points. The RMSE obtained from the statistical resampling experiments was likely to be a slightly conservative estimate of the actual DEM error because the random measurement errors existed both in the interpolated points and the check points.

The relation between RMSE and the data point spacing is useful for survey planning and can aid in deciding on the spacing of data sampling. It can also be used to guide the data density reduction. A point cloud may contain a large amount of data points, requiring substantial computer resources to store and process. In some cases, it may be beneficial to reduce the density of an existing point cloud while the accuracy requirement of a certain task is met.

6.6 Summary

DEM accuracy and the factors influencing it, such as data density and surface characteristics, were investigated in this chapter. A statistical resampling technique was introduced, which provided a useful means of evaluating DEM error. This experiment was applied to several interpolation methods to compare their relative accuracy in representing an engineered slope surface. Among these, the TIN with linear interpolation was the most accurate interpolator. For all interpolators, the DEM errors increased linearly with increasing equivalent point spacing in the range 35 mm - 100 mm.

The DEM errors for the four surfaces of different characteristics were quantified. The results suggest that the minimum level of detection for a very smooth ground surface (either flat or of detectable spatial variations) is likely to be at the millimetric level. However, for surfaces that have non-detectable noise from spatial variation, the DEM error is larger. For example, the

DEM error for the engineered slope was about 6.6 mm (1σ) for an equivalent point spacing of 35 mm.

The DEM errors consisted of two parts: a noise-related part and a data-density dependent part. For the engineered slope surface and the landslip surface considered in this study, the noise was a major contributor to the overall DEM errors when the point spacing was smaller than 35 mm. A finer data density would not reduce the noise-related part. Therefore, it was unnecessary to use a very fine scan resolution (e.g. a sampling spacing < 20 mm) for TLS surveying in practice.

Chapter 7 :

Georeferencing-induced positional errors and SDM Uncertainty

7.1 Introduction

For detecting surface deformations over time, repeated TLS surveys of the same object at a certain time interval are required. Attempts had been made to identify an unstable engineered slope suffering relatively large movements with the Highways Agency, but unfortunately such a slope was not available. Instead, multi-temporal TLS surveys of some objects located on the campus of the University of Southampton were carried out. The survey procedure adopted was similar to that would be used for measuring the deformations of engineered slopes.

The objects measured by repeated TLS surveys were fixed in place during the full period of each individual survey experiment. Hence any apparent movements of these objects, derived from the multi-temporal TLS data, are simply errors. On this basis, the georeferencing-induced positional errors are quantified empirically. In this thesis, the georeferencing-induced positional errors refer to the relative positional errors between two sets of TLS data acquired at different times. These errors are caused by the uncertainties involved in the surveying processes of tying multi-temporal TLS data into a common external coordinate system. A combination of the georeferencing-induced positional errors and those discussed in preceding chapters can be used to assess the possible minimum magnitude of deformation that repeated TLS surveys can detect. This is demonstrated in this chapter.

7.2 Multi-temporal TLS surveying

This section reports four empirical experiments, which were carried out to quantify the georeferencing-induced positional errors involved in repeated TLS surveys for detecting surface movements over time. The objects scanned in these experiments were not on the move. In each

of these experiments, two sequential TLS survey campaigns were carried out to measure these unmoved objects. If the multi-temporal TLS surveying was capable of measuring small movements, the point clouds representing the objects surveyed in the first survey campaign should well match those obtained in the subsequent survey. However, there would be positional differences between the multi-temporal point clouds representing the same objects, because of uncertainties in the TLS surveys. These differences form the basis of evaluating the georeferencing-induced positional errors.

7.2.1 Georeferencing

For measuring surface deformations, multi-temporal TLS data need to be georeferenced into a common external coordinate system. Georeferencing strategies for TLS surveying include surface matching, direct georeferencing and target-based ground control.

In surface matching, the data points representing overlapping stable areas in multi-temporal datasets are used to establish the optimal transformation. This method can be based on the iterative closest point (ICP) algorithm (Besl and McKay, 1992; Chen and Medioni, 1992), and has been used for georeferencing multi-temporal TLS data (Prokop and Panholzer, 2009). Gruen and Akca (2005) provided a comprehensive overview of surface matching strategies. Miller et al. (2008a) proposed a surface matching technique for the survey data representing a coastal area. Surface matching can be considered for cases where there are a sufficient number of 3D features of different orientations in the overlap between two point clouds. It can produce an accurate transformation solution especially when the overlapping 3D surfaces are smooth and regular such as those in the built environment. It has also been used in a natural environment such as a coastal area (Miller et al., 2008a) and a debris-flow site (Schürch et al., 2011). A potential problem associated with this method is that the overlapping ‘stable’ surfaces between sequential surveys may have changed over time (Olsen and Stuedlein, 2010; Lague et al., 2013).

In direct georeferencing, a terrestrial laser scanner can be centred over a known point, levelled and orientated to a known backsight (Lichti et al., 2005b). It has been investigated by several researchers (Scaioni, 2004; Reshetyuk, 2009, 2010b; Mohamed and Wikinson, 2009). The uncertainty in directly georeferenced TLS data was investigated by Lichti et al. (2005b). In this method, the locations of the scanner and the backsight target are usually measured using GPS antenna mounted onto the scanner and the backsight target in a special arrangement. Such a non-bespoke arrangement may not be immediately available to many laser scanner users. In addition, relying on a single backsight point for orientation may result in a georeferencing of relatively low quality.

In the target-based ground control method, the locations of targets placed over a scan scene are also measured using a second instrument (e.g. DGPS or total stations). These measurements are used to georeference TLS data into a national grid or a local control system. For TLS surveying in a natural environment, DGPS seems more popular for georeferencing (e.g. Schürch et al., 2011; Coveney and Fotheringham, 2011; Montreuil et al., 2013) than other instruments. The accuracy of georeferencing using a Real Time Kinematic (RTK) DGPS was 17 mm in Montreuil et al. (2013) and 45 mm in Coveney and Fotheringham, (2011).

Georeferencing is a crucial step for surface deformation detection (Barbarella and Fiani, 2013; Prokop and Panholzer, 2009), especially when surface movements are small. For example, some engineered slopes in the UK may experience movements of several centimetres before a catastrophic failure (Cooper et al., 1998; Potts et al., 2000; Ellis and O'Brien, 2007). Detecting such low-magnitude surface displacements places particularly high demand for the quality of survey control and such a requirement may be easily overlooked (Miller et al., 2008b).

Total stations have been widely used in conventional engineering surveying and are well-known for their high precision and accuracy. For monitoring a local site (e.g. an engineered slope), a local control established properly using a total station is likely to result in the most accurate georeferencing solution. This approach was adopted for the study reported in this chapter.

7.2.2 Study site

The experiments were carried out on the campus of the University of Southampton. There was a slope (Figure 7.1) on one edge of the campus's largest open green area where ground control points were established. Three wooden plates were placed on and around the slope, including a horizontal one near its toe, a vertical one at its crest and a third on the slope surface (Figure 7.1). These plates were fixed in place during each experiment. A plate perpendicular to the length of the slope was not placed. A piece of a smooth building facade (referred to as a side plate) was used (Figure 7.1). The vertical plate, the horizontal plate and the side plate can be used to show apparent movements along the cross-section / height / length of the slope, respectively.

The reasons to use these plates: (1) there is no modelling/interpolation error because the planes can be perfectly modelled by some interpolation methods such as TINs and linear polynomial function; (2) least-squares fitting planes can be used to fit the survey data representing these plates and thus the effects of measurement errors can effectively be removed. As the DEM errors (i.e. interpolation errors and propagated measurement errors combined) are not involved

in the analysis of TLS data representing these plates, the errors derived from repeated surveys of these plates are simply the georeferencing-induced positional errors.

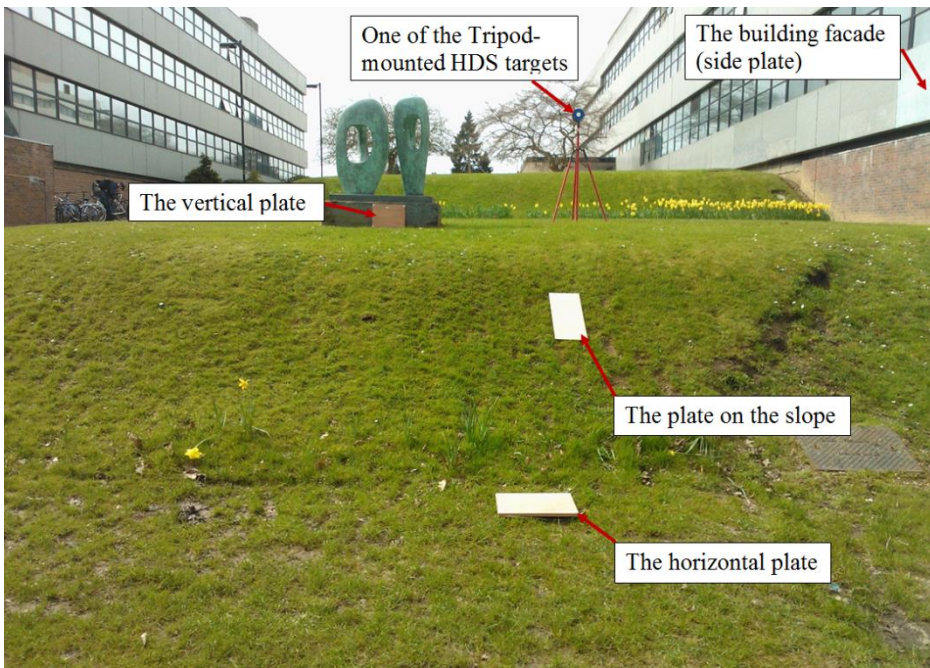


Figure 7.1: Photo of the slope and the plates.

7.2.3 Method

Wooden pegs were installed into the ground at various locations for establishing local controls using a Leica FlexLine TS09 total station (accuracy of angle measurement: 1"; accuracy of distance measurement with and without reflector: 1 mm + 1.5 ppm and 2 mm + 2 ppm, respectively) hired from SCCS Survey. The ScanStation C10 was used for surveying the objects of interest. The HDS targets used in the survey experiments were Leica 6 inch blue & white, tilt & turn circular targets.

Four experiments (Figure 7.2) were carried out and are detailed in this section. In each experiment, it was assumed that there was a stable area (indicated by "Local control" in Figure 7.2). In Experiments 1 and 2, the local controls (stable areas) were relatively close to the monitored area. In Experiments 3 and 4, a transition zone was used, which may be required in TLS surveying in a natural/semi-natural environment for the following reasons: (i) a local control is relatively far from a monitored site (it was found in the survey experiments that it was difficult to use the total station telescope to observe the centre of the HDS targets placed at a distance of larger than 80 m; to reduce pointing (sighting) errors, it is better to place the targets within a distance of 80 m from the total station); (ii) visibility problems (i.e. a monitored site is not visible directly to a local control); (iii) multiple scan locations are required for a relatively

large site. The distances between the local controls and the scanner were about 50 m and 130 m, which reasonably reflect the situations for monitoring many engineered slopes.

In professional surveying, the backsight point should be far from the total station to reduce the orientation error. However, the backsight points (e.g. E1P2) in Experiments 1 and 3 were deliberately made close to the total station to reflect the fact that it is not always possible to identify or create a distant and stable backsight point in a natural/semi-natural environment.

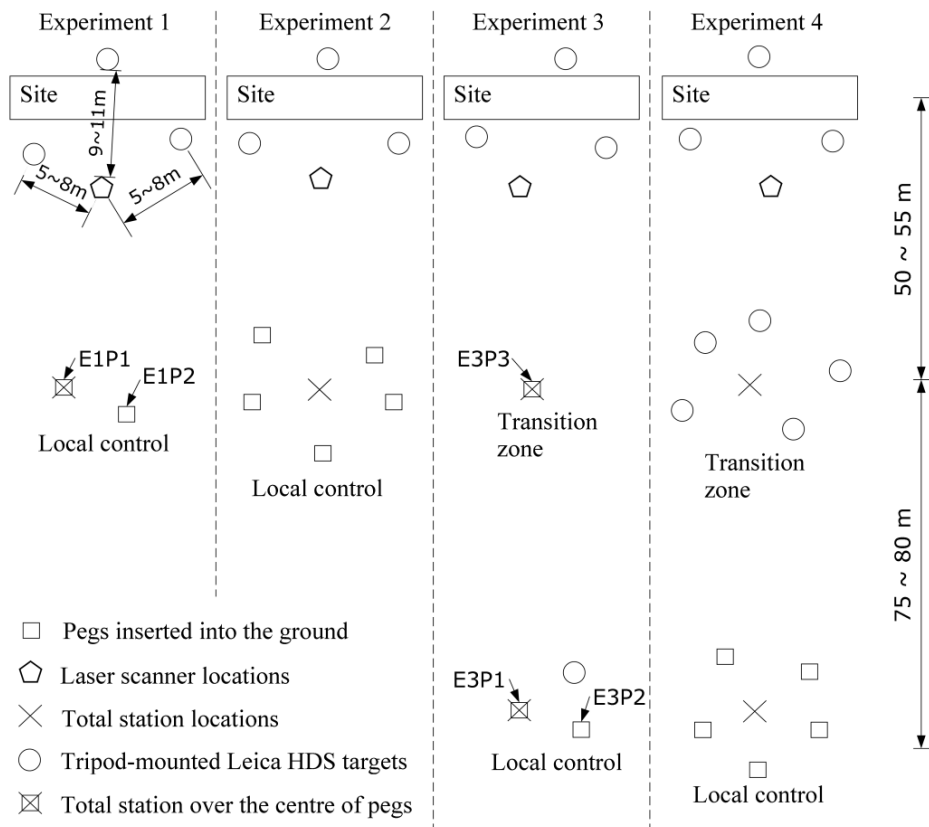


Figure 7.2: Topologies of survey controls.

7.2.3.1 Experiment 1

The survey procedure of the first survey campaign in Experiment 1 is as follows. Pegs E1P1 and E1P2 were installed firmly into the ground. Three tripod-mounted Leica HDS targets were placed around the site accommodating the scan objects. The external bubble and the electronic bubble were used to level the total station and its dual-axis compensator was enabled. The laser plummet of the total station and the tribrach were used to focus the instrument centre above the centre of the peg E1P1. Arbitrary XY coordinates of the peg E1P1 and the height of the total station above an assumed datum plane were assigned. The total station was then aligned north with the centre of the peg E1P2 to define its orientation. Once the total station was set up, it was used to measure the centre of the peg E1P2 and the centre of each HDS target. After the total

Chapter 7. Georeferencing-induced positional errors and SDM Uncertainty

station measurements, the scanner was placed in front of the scan objects and levelled, and its dual-axis compensator was enabled. It recorded the scan objects and the HDS targets.

Once the preceding steps were completed, the first survey campaign ended. All the equipment (scanner, total station, tripod-mounted HDS targets and tripods) was removed and then fully packed (e.g. the scanner was put back into its container) except that the scan objects and the pegs used for the local control system remained at the same locations. This represented the finish of a TLS survey campaign in the field. About 10 - 20 minutes later, the second survey campaign started and followed a similar procedure as the first one, representing a subsequent survey campaign in the field. The actions presented in this paragraph were taken for all the remaining survey experiments (i.e. Experiments 2, 3 and 4) and will not be described repeatedly in the descriptions of Experiments 2, 3 and 4.

In the second survey campaign, the same pegs (i.e. the total station over the peg E1P1 with the backsight to the peg E1P2) were used for the total station setup. The survey steps were the same as those in the first survey campaign except that: (1) the XY coordinates of the peg E1P1 was already known and (2) the total station height above the assumed datum was determined by the elevation (measured in the first survey campaign) of the peg E1P2 and the height difference (to be measured in the second survey campaign) between the total station instrument centre and the peg E1P2. As the mini-tripods (supporting the HDS targets) placed around the scan objects were removed after the first survey campaign, their locations were slightly different in the second survey campaign (this also occurred to Experiments 2, 3 and 4, and will not be stated repeatedly for them).

7.2.3.2 *Experiment 2*

In the first survey campaign, five pegs were installed firmly into the ground and three HDS targets were arranged around the scan objects. The total station was placed at an arbitrary location inside the polygon formed by the pegs, levelled (with the aid of the external and electronic levelling) and aligned north with one of the pegs. Its dual-axis compensator was enabled. It was used to measure the centre of each peg and then the centre of each HDS target. After this step, the scanner was set up in the same way as that in Experiment 1. Laser scanning was then carried out to survey the scan objects and the HDS targets.

In the second survey campaign, the survey procedure was the same as that in the first survey campaign except that the total station was placed at another arbitrary location inside the polygon and a resection was carried out to determine the total station location and orientation.

7.2.3.3 *Experiment 3*

In the first survey campaign, pegs E3P1, E3P2 (at the local control) and E3P3 (in the transition zone) were installed firmly into the ground. The total station was set up over the peg E3P1 in the same way as that in the first survey campaign of Experiment 1. A temporary tripod-mounted HDS target was placed near the local control, and its centre was measured by the total station. A pole supporting a round prism was held vertically by another person over the peg E3P3, and the prism was measured by the total station located above the peg E3P1. The total station was then moved to the transition zone, centred and levelled over the peg E3P3, and then orientated to the temporary HDS target near the local control to finish the setup. After these steps, the HDS targets placed around the scan objects were measured by the total station located in the transition zone. After the total station measurements, the scanner was set up in the same way as that in Experiment 1. Laser scanning survey was then carried out to survey the scan objects and the HDS targets.

In the second survey campaign, the same pegs located at the local control were used to set up the total station, following the same procedure as that in the second survey campaign of Experiment 1. A temporary tripod-mounted HDS target was arranged near the local control, and its centre was measured by the total station. A new peg was installed into the ground in the transition zone. A pole supporting a round prism was held vertically by another person over this peg, and the prism was measured by the total station. The remaining steps were the same as those in the first survey campaign.

7.2.3.4 *Experiment 4*

Successive resection was used in this experiment. In the first survey campaign, the local control was established using the approach described in the first survey campaign of Experiment 2. Five temporary tripod-mounted HDS targets were placed in the transition area, which were measured by the total station located at the local control. The total station was then moved to an arbitrary location surrounded by the temporary HDS targets in the transition zone and a resection was carried out to determine the total station location and orientation. Once the total station was set up in the transition zone, three of the five tripod-mounted HDS targets were moved and placed around the scan objects. These targets were then measured by the total station from the transition zone. After the total station measurements, the scanner was placed in front of the scan objects and levelled, and its dual-axis compensator was enabled. It was to record the scan objects and the HDS targets.

The survey procedure in the second survey campaign was the same as the first one except that a resection was also carried out at the local control to determine the total station location and orientation.

7.2.4 Data processing

Multi-temporal TLS survey data were transformed into the total station coordinate systems (defined by the local controls) using Leica Cyclone[®] 7.3. The data points representing the vertical, horizontal and side plates were separately selected in Cyclone[®] 7.3 and imported into MATLAB[®] (R2012a) where these data points were fitted with least-squares planes. The fitting planes representing the same objects surveyed at different times (i.e. the first and the second survey campaigns) were compared to show the apparent movements of the objects. The vertical plate, the horizontal plate and the side plate were used to derive apparent movements (surveying errors) along the cross-section/height/length of the slope, respectively.

7.2.5 Results

The apparent movements (or surveying errors in repeated TLS surveys) of the scan objects in each experiment are summarised in Table 7.1. The least accurate TLS surveys occurred in Experiment 3, which was not surprising as the pole held by a person would not be perfectly vertical although an attempt was made to hold it as plumb as possible. The apparent movements were very small in all other experiments, suggesting that repeated TLS surveys have the potential in measuring very small deformations. For a local control established at a distance of roughly 130 m in Experiment 4, the apparent movement were less than 3 mm in plan and 1 mm in elevation.

Experiments	Separations (georeferencing error), in mm		
	Side plate	Vertical plate	Horizontal plate
Experiment 1	1.5	0.7	0.5
Experiment 2	2.2	0	1.0
Experiment 3	19.8	9.2	1.4
Experiment 4	2.2	2.9	0.2

Table 7.1: The apparent movements of the scan objects.

The apparent movements in Z direction were very small in all the experiments. This is likely due to the use of the survey-grade dual-axis compensators of the total station and the scanner, which can correct the deviation of the instrument standing axis from the plumb line.

The experiments can be divided into two categories: (i) the total station was aligned with a single fixed / known point (Experiments 1, 3); (ii) the total station was set up using multiple fixed points (Experiments 2 and 4). Although the setup procedure of the former is simple, no redundant measurements are available to enhance the TLS surveying quality. Therefore, it is more vulnerable to errors such as operator errors or blunders. In the latter category, the location and orientation of the total station are determined from five known points using a least squares technique. In this case, the georeferencing-induced positional errors are likely to be smaller.

Experiments 2 and 4 shared the same approach (i.e. resection) for setting up the total station used for georeferencing the multi-temporal TLS data. The apparent movements (i.e. surveying errors) were very small in both experiments. This suggests that the resection using multiple control points (five control targets were used in Experiment 4) is a reliable way of achieving a high georeferencing accuracy. Repeated TLS surveys using this approach can detect millimetric movements of regular and smooth objects.

7.3 Uncertainty in SDMs for a terrain surface

The results reported in Section 7.2 show that the ScanStation C10 coupled with a total station is capable of detecting surface deformations of small magnitude. However, the surfaces surveyed were planes (e.g. wooden plates). Also, the data points representing the planes were fitted with least-squares planes before a comparison was made. These effectively removed both interpolation errors and propagated measurement errors, which often exist in a DEM representing a terrain surface. Therefore, to infer the capability of repeated TLS surveys in measuring the movements of a terrain surface, the DEM errors (already discussed in Chapters 5 and 6) should be added on top of the uncertainty discussed in Section 7.2. This is discussed in the following sections.

7.3.1 Surface deformation models

Multi-temporal laser scanning data can be compared to show surface movements over time. As TLS data consist of scattered topographical points, data processing methods are required to enable the comparison. There are various methods in the literature.

- The cloud-to-cloud method: raw data points in multi-temporal TLS data are compared directly (Girardeau-Montaut et al., 2005). Each point in a point cloud is compared with its closest point in the reference point cloud. The implementation of this method is simple and fast. However, it may be problematic when the TLS data density is coarse. Recently, Lague et al. (2013) and Barnhart and Crosby (2013) reported a new model-based cloud comparison algorithm.
- The cloud-to-surface method: raw data points in a point cloud are compared with a baseline digital elevation model (DEM) (e.g. Abellán et al., 2009, 2010; Olsen et al., 2010). In these methods, surface deformations are calculated at scattered locations. Visualising these deformations as a continuous map requires a visualisation algorithm, which may cause a misunderstanding if not clearly stated.
- The surface-to-surface (DEM-to-DEM) method: a DEM was created for each of the multi-temporal point clouds. The multi-temporal DEMs were then compared to show surface movements. More specifically, a SDM can be derived from the multi-temporal DEMs through a direct subtraction (i.e. $SDM = DEM_2 - DEM_1$).

The DEM-to-DEM method is probably the most commonly used method as it is a standard routine for deformation calculation in the field of remote sensing and geographical information science (e.g. Miller et al., 2008b; Jaboyedoff et al., 2009; Prokop and Panholzer, 2009; Wheaton et al. 2010; Schürch et al, 2011; Montreuil, et al., 2013). This method is adopted for further demonstration.

7.3.2 Propagation of DEM errors into SDMs

A SDM was derived from two grid DEMs through a direct subtraction. In this process, the errors in individual DEMs will be propagated into the SDM, which can be based on the following classic error propagation method.

$$\delta_{SDM} = \sqrt{\delta_{DEM_1}^2 + \delta_{DEM_2}^2} \quad (7.1)$$

where δ_{DEM_1} and δ_{DEM_2} are the errors in the first and the subsequent DEMs, respectively; δ_{SDM} is the propagated errors in the SDM.

This simple method assumes that elevation errors in each individual DEM are random and that a cross-correlation between errors in the two DEMs does not exist. This method has been used by

several researchers (e.g. Brasington et al., 2003; Wheaton et al., 2010) to propagate DEM errors into a SDM. A detailed guide on general error propagation can be found in Taylor (1982).

If the mean errors in DEMs are approximately (or are assumed to be) zero, the RMSE is equal to the standard deviation of elevation errors. In this case, Equation (7.2) can be used to propagate DEM errors.

$$\sigma_{\text{SDM}} = \sqrt{(\text{RMSE}_{\text{DEM}_1})^2 + (\text{RMSE}_{\text{DEM}_2})^2} \quad (7.2)$$

where σ_{SDM} is the standard deviation of errors in the SDM; $\text{RMSE}_{\text{DEM}_1}$ and $\text{RMSE}_{\text{DEM}_2}$ are the RMSEs in the first and the subsequent DEMs, respectively.

In Chapter 6, the DEM errors for four different types of terrain surfaces were investigated. It also introduced a statistical resampling method that can be used to assess the DEM error for a particular terrain surface of interest. For example, the DEM error for the Newbury cutting was 6.6 mm (1σ) when the equivalent point spacing of the data points was roughly 35 mm (Figure 6.8). The mean error for the DEM representing the Newbury cutting was almost zero (Figure 6.5). If the DEM error for a point cloud obtained in a subsequent TLS survey of the same slope was similar (assumed to have the same value in this demonstration). The standard deviation of the error in the SDM due to propagated DEM errors is:

$$\sigma_{\text{SDM}} = \sqrt{(6.6)^2 + (6.6)^2} = 9.3 \text{ mm (at } 1\sigma\text{)}$$

For the case of the Newbury cutting, the SDM error propagated from individual DEMs was much larger than the surveying errors in Experiment 4 reported in Section 7.2.5. For high quality multi-temporal TLS surveying (e.g. Experiments 4), the uncertainty in a SDM depends mainly on the accuracy of individual DEMs used to derive the SDM. For the Newbury cutting, the minimal level of detection is likely to be 20 mm (the 95% confidence interval) (assuming a high georeferencing accuracy is achieved). In this case, the surface deformations greater than 20 mm can be measured with a high level of confidence.

7.4 Discussion

The objects scanned in the empirical survey experiments did not move over time, which enabled an accurate assessment of the georeferencing-induced errors in repeated TLS surveys of the same

Chapter 7. Georeferencing-induced positional errors and SDM Uncertainty

objects. To increase chances of measuring small deformations, it is crucial to choose an appropriate georeferencing method and implement it properly and carefully during surveying. This places high demand for skills of individual surveyors. A resection using multiple known points (for example, five points) does not require manual centring and orientation of a total station and hence reduces the dependence of the surveying quality on the surveyors' operation. It is therefore recommended.

The surveys in this section were designed to reflect the situation where the monitored site was small (e.g. a section of an engineered slope) and there was a stable area at a reasonably distance (50 m - 130 m) from the monitored site. However, if a monitored site is large or far from a stable area where a local control can be built, the georeferencing-induced errors in repeated TLS surveys may be larger than those reported in this section.

When an area of clayey soil or an object founded on clay is chosen for creating a local control, it is also important to appreciate that high plasticity clay is vulnerable to seasonal fluctuations in soil water content and associated shrinking and swelling processes. In these cases, it would be better to install the pegs deeply into a layer below the seasonally affected zone of clayey soil.

7.5 Summary

Four empirical survey experiments have been carried out to evaluate the georeferencing-induced positional errors involved in repeated TLS surveys of some fixed objects. The results indicate that repeated TLS surveys using the ScanStation C10 can measure very small movements of smooth objects if a high georeferencing accuracy is achieved. The resection method of the total station, using five known control points, was found to be an effective method of obtaining a high georeferencing accuracy (the georeferencing-induced positional errors were about 2 - 3 mm in Experiments 2 and 4).

The georeferencing-induced positional errors should be combined with the DEM errors to assess the capability of TLS surveying in measuring the movements of a terrain surface. The method for the propagation of errors in individual DEM into a SDM was introduced, which was used to infer the likely minimum level of detection for the Newbury cutting.

Chapter 8 :

Conclusions

Terrestrial laser scanning has been used increasingly for surveying terrain surfaces and monitoring surface movements such as those caused by slope failures. Yet the capability of this technique in these applications is poorly understood. Put in the context of local-scale monitored sites (e.g. engineered slopes), this research has investigated errors in digital elevation models (DEMs) derived from terrestrial laser scanning (TLS) survey data points. In combination with the georeferencing-induced positional errors, the DEM errors can be used to infer the capability of TLS surveying in detecting surface movements of slopes.

8.1 Key results

8.1.1 Measurement performance of TLS instrument

The measurement performance of the Leica ScanStation C10 used in this research was checked against a total station. The experimental results confirm that its performance met the specification given by Leica, and thus the research objective 1 was fulfilled.

8.1.2 Performance of TLS in vegetated surface

To fulfil the second objective, empirical experiments have been carried out on grass areas. The vegetation effects were found to be a big challenge for TLS surveys of vegetated terrain surfaces, which can cause a significant elevation error if the information desired is the bare ground. For the case studies in this research, the average grass-induced elevation error was 60% - 65% of the grass height. For a monitoring project where high accuracy is crucial, it would be better to remove vegetation before scans are carried out. However, there are ways of reducing vegetation effects if cutting vegetation off is not an option. A finer resolution scan with a smaller incidence angle can reduce vegetation error, as will scanning the same area from multiple locations. A larger search window could further reduce the vegetation error by selecting lower points, but more topographical detail would be lost. Vegetation errors in data from sequential surveys will cancel out to some extent, especially for the multi-temporal

datasets acquired from the same multiple locations and with the same scan parameters. The vegetation effects, and the magnitude and rate of slope surface movement, must be considered together when TLS surveying is used to detect slope movements.

8.1.3 Accuracy of DEMs

To accomplish research objective 3, two pieces of work have been carried out, consisting of (i) a study on the effects of measurement errors in source data points on the accuracy of DEMs (created using a TIN with linear interpolation) in Chapter 5 and (ii) an investigation on the effects of another three factors (densities of survey data points, roughness of terrain surfaces and interpolation methods) on the DEM errors using a statistical resampling technique in Chapter 6. The key contributions are summarized below.

- The research contributes to the literature by setting out an analytical approach to characterize error propagation in a TIN with linear interpolation, which is of use to quantify the DEM error (at any particular location) caused by horizontal and vertical positional errors in source data points (such as TLS, LiDAR or DGPS data points). For the special case of equal and independent errors in source data points, the maximum, average and minimum values of propagated error variance were found to be equal to unity, a half and a third respectively of the error variance in source data points.
- The study has investigated the behaviour of the DEM errors for cases where TLS data points are used to build a DEM. It shows that the DEM errors can be decomposed into two parts: (1) a point spacing dependent part, and (2) a noise-related part. The former depends on the signal of spatial variation of a terrain surface. It increased linearly with increasing point spacing in the range 35 mm - 100 mm for the local terrain surfaces considered in this study. The latter is caused by the noise from spatial variation of the surface and measurement, and is considered independent of data densities. In practice, using a higher sampling density would capture the signal of spatial variation in more detail, which leads to a reduction in the DEM errors and thus an increase in chances of measuring movements of smaller magnitude. However, it is not necessary to use a very fine scan resolution (e.g. a sampling spacing < 20 mm) for TLS surveys of a rough terrain surface, because noise is likely to dominate the DEM errors when data point spacing is small.
- It is found that data point densities and terrain surface roughness considerably affect the accuracy of DEMs created using TLS data points. Terrain surface roughness imposed a

strong influence on the DEM errors by affecting both the point spacing dependent part and the noise related part of the DEM errors. However, a quantitative evaluation of the correlation between terrain surface roughness and the DEM errors was not carried out in this study, which could form the subject of future research.

8.1.4 Uncertainty in georeferencing

To fulfil the research objective 4, repeated TLS surveys of some stable objects have been carried out. The results show that the georeferencing-induced positional errors in repeated TLS surveys can be very small (< 3 mm). To achieve high accuracy TLS surveying, it is essential to tie multi-temporal TLS data accurately into an external coordinate system. The results in this study indicate that using the resection (based on five control points) technique of total stations can accurately georeference successive TLS data into the same external coordinate system. Hence this approach is recommended for TLS surveys of a local terrain surface such as an engineered slope.

8.2 Application of TLS systems to slopes

To evaluate if TLS systems are useful for monitoring a particular slope, it is essential to consider two aspects: (1) the magnitude of slope movement between two TLS surveys carried out at different times and (2) the minimum magnitude of deformation that TLS systems can effectively detect.

8.2.1 Application to vegetated slopes

In the case of vegetated engineered slopes, the vegetation effects are a major limiting factor on TLS measurements. The experimental results presented in Chapter 4 show that the elevation error caused by short vegetation (grass) is much greater than the magnitude of movement that many engineered slopes are likely to experience before first failure (see Chapter 2). Therefore, TLS systems are not considered a suitable technique for providing early warning of incipient failures of many engineered slopes if grass is present. However, in the post-failure stage, some slopes may be on the move actively or occasionally. As the post-failure slope deformations may be relatively large, TLS can be a useful tool for detecting the pattern and the rate of these deformations. In this case, it is recommended that multi-temporal TLS surveys are carried out from the same multiple locations and with the same scan parameters. As illustrated in Chapter 4, this can lead to the vegetation errors being cancelled out to a greater extent when multi-temporal TLS datasets are compared for obtaining slope surface changes, and hence can increase the chance of detecting smaller slope movements.

To measure the deformations of vegetated engineered slopes more accurately, it would be better to remove vegetation before TLS surveys take place when it is practically possible and justifiable. Otherwise, other types of surveying instruments and/or geotechnical sensors can be considered.

8.2.2 Application to non-vegetated slopes

To assess the fitness of TLS surveys for a non-vegetated slope, several factors need to be taken into account. The surveying accuracy is a critical factor, which often determines the success of TLS surveys for deformation measurements, as demonstrated in Chapter 7. As many short-range terrestrial laser scanners such as the ScanStation C10 used in this study can produce high quality measurements, the surveying accuracy is determined mainly by the georeferencing and registration quality. In the survey planning stage, a holistic consideration of the survey controls for a given site is essential for achieving an optimal survey control solution, which can lead to a high surveying accuracy.

For multi-temporal TLS surveys of a very high surveying accuracy, the minimum level of detection depends mainly on the accuracy of individual DEMs used to derive a SDM. The small DEM errors for the smooth surfaces investigated in Chapter 6 suggest that TLS surveying is capable of measuring millimetric movements of smooth slope surfaces. However, the DEM errors for the rough surfaces considered in Chapter 6 were relatively large. For example, the DEM error for the Newbury cutting was 6.6 mm at 1σ for the point spacing of 35 mm. In this case, repeated TLS surveys can detect surface movements of larger than 20 mm (at the 95% confidence level). If the slope experiences surface deformations smaller than this value, TLS surveying would not be a suitable solution.

The pre-failure deformations of many well-constructed engineered slopes are likely to be small (e.g. 20-30 mm for the Selborne cutting reported in Chapter 2) and may occur over a relatively long period (e.g. several years or longer) before first failure occurs. If the surfaces of these slopes are rough (likely to be the case for many engineered slopes in service), TLS is not considered competent in predicting incipient failures of these slopes. However, there may be non-vegetated slopes, the surfaces of which are smooth (thus the DEM errors associated with these surfaces are small), and/or the pre-failure deformations of which are relatively large (e.g. larger than 50 mm). For these slopes, it is possible to use TLS surveys to predict first failure. More generically, the method introduced in Chapter 6 can be used to inform if TLS surveys are useful for a particular site. From an asset management perspective, the pre-failure deformations of many engineered slopes may be so small that no noticeable signs of potential instability can

be identified to justify a monitoring action in the first place (see Chapter 2). In this regard, the prediction of incipient failures of many engineered slopes remains challenging in practice.

The post-failure surface deformations of many engineered slopes are likely to be relatively large compared to the minimum level of detection of TLS for a non-vegetated slope surface. Hence TLS is considered a useful tool for measuring the post-failure slope surface displacements. The fine-resolution scan data provided by TLS systems can aid in our understanding of the spatial behaviour of slope movements over time.

8.2.3 Application of TLS systems to other geohazards

The deformations experienced by other forms of geohazards such as coastal recession and earth surface erosion are often much larger than those caused by instability of engineered slopes. TLS is expected to have more practical use in monitoring these geohazards.

8.3 Future work

Based on the research presented in this thesis, the following suggestions for further work are made.

- In this research, the effects of vegetation on TLS measurements were investigated using a single-return laser scanner. Another type of laser scanning technique is full-waveform laser scanning where the scanner records and processes the entire waveform of a return pulse (Wagner et al., 2004; Mallet and Bretar, 2009). This may allow users to extract the information that can be used to derive data points closest to the bare ground. It would be interesting to investigate how the vegetation effect would manifest itself if a full waveform scanner is used. To this end, some empirical field experiments similar to those reported in Chapter 4 could be carried out.
- The relation between the DEM error and the factors influencing it was studied through statistical resampling experiments. However, this approach may not be straightforward for surveyors or engineers to implement in practice. A mathematical relation may be more useful, which requires a more detailed study on the correlation between the terrain roughness (complexity) and the DEM error. To do this, parameters describing surface roughness are required. A literature review is needed to identify the potential roughness descriptors. The fitness of these parameters can be assessed using numerical simulations, in which the correlations between the roughness descriptors and the DEM

Chapter 8. Conclusions

error can be quantified. Based on the analysis results, a mathematical relation between the surface roughness and the DEM error can be established.

- The ways to arrange control targets to obtain a high georeferencing accuracy are well understood in conventional surveying. However, to the best knowledge of the author, there are no rigorous solutions in the literature for a quantitative estimation of the georeferencing errors. In this research, empirical experiments were carried out to assess the georeferencing-induced positional errors in multi-temporal TLS surveys. As georeferencing is a critical factor for the accuracy of multi-temporal TLS surveying, it is useful to derive a solution for estimating the georeferencing error in any particular scan data points. Error propagation theory can be considered for deriving such a solution. It is expected that the solution can be achieved using analytical and/or numerical approaches.

Appendices

Appendix 1: Highway earthwork failures during 2000/2001

The winter in 2000/2001 is thought to be the wettest in English history by the time the following table was prepared (Feb 2013). During this extreme winter, there were 60 landslips in the highway network (by the mid of April 2001) (Perry, 2001). The total length of slips was approximately 2000 meters. The slips of cuts and embankments in the Area 3 of the UK highway network are listed in Table A1.1 and Table A1.2 respectively.

<i>Site</i>	<i>Type and geometry of slope</i>	<i>Width affected(m)</i>	<i>Category (Table 2.1)</i>	<i>Failure type and position</i>	<i>Main features</i>
M25, Flint Hall Farm, Junction 6 on-slip eastbound	Cut Height: 20m; Angle: 1(v):4(h) to 1(v):5(v)	200	i	Deep compound failure; Entire slope	Steep backscarp and 150mm toe bulge at the motorway hard shoulder; A large soil wedge formed by the intersection of the steep backscarp and a near horizontal main shear surface, which was up to 10m below ground level.
A3(M), Junction 2 off slip, ch 7.8.40 - ch7.8.40	Cut Height: 9m; Angle: 1(v):3(h)	40	ii.3	Shallow compound slide; Mid-slope to slope crest	2m high sub-vertical backscarp; graben area up to 5m wide and a smaller counterscarp; slopes are generally very wet but no seepage presented.
A3(M), Junction 2 off slip, ch7.8.210 - ch7.8.222	Cut Height: 4m; Angle: 1(v): 3 ⁺ (h)	12	ii.3	Shallow rotational slide; Entire slope	0.5-1.0m high sub-vertical backscarp; slopes are very wet and some evidence of seepage in the upper level of slip
A3(M), Junction 2 off slip, ch+74m to ch+90m	Cut Height: 4m; Angle: 1(v):3(h)	16	ii.3	Shallow rotational slid; Entire slope	0.5-1.0m high sub-vertical backscarp; slopes are very wet and some evidence of seepage in the backscarp of slip leading to soft ground and local ponding

A3(M), Junction 2 off slip, ch+30	Cut	5	ii.3	Minor slips	No information provided
A3(M), Junction 2 off slip, ch+50	Cut	10	ii.3	Minor slips	No information provided
A3(M), NB MP 6.0	Cut Height: 6.5m; Angle: 1(v):3(h)	15	i	Mudslide; Lower slope only	0.5m shallow backscarp; shear surfaces evident; slopes are very wet and some evidence of seepage in the backscarp of slip leading to soft ground and local ponding; water running through the failed area
A34, Tothill	Cut	65	i		No information provided

Table A1.1: Known cut failures in UK highway network-Area 3 during the winter of 2000/2001 (a summary based on Perry's survey report, 2001)

<i>Site</i>	<i>Type and geometry of slope</i>	<i>Width affected (m)</i>	<i>Category (Table 8.2)</i>	<i>Failure type and position affected</i>	<i>Main features</i>
M25, Marker Post 40.1	Embankment	75	ii.1		No information provided
M25, Junction 6 On slip	Embankment Height: 9m; Angle: 1(v):3(h)	21	ii.1	Reactivation of pre-existing slip surface; Entire slope (affected)	Wide backscarp and toe bugle. Seepage at several location within toe bugle
M3, Junction 5 Round-about	Embankment Height: 5m; Angle: 1(v):2(h)	10	ii.3	Shallow failure; Entire slope	Two backscarp less than 0.4m high and small toe bulges; the slope is very wet underfoot with some ponding on the sloped ground and in the backscarps. Failed drainage present; the material exposed in the backscarp was soft clay with some gravel

M3, Junction 2-3	Embankment Height: 8m; Angle: 1(v):2(h)	30	ii.1	Shallow failure; Entire slope	1.0-1.2 m high backscarp; tension crack; a broken drain noted; two safety fence posts moved; some material in the backscarp is wet; the exposed material varied from yellowish-grey clayey sand to medium sand with some gravel.
M27, Junction 5 off slip	Embankment Height: 6m; Angle: 1(v):2.1(h)	25	ii.2/ ii.3	Shallow failure; Mid-slope to slope toe	Tension cracks near scarp extending at least 10m; cracks in the mid of the slope; the entire slope was extremely wet and soft; standing water was seen at the toe;
M23, Junction 9 On slip	Embankment Height: 6m; Angle: 1(v):2.25(h)	19	ii.2/ii.3	Shallow failure; Entire slope	The entire slope was extremely wet and soft; a major and some minor scarps; toe bulge present; a tension crack at the position of the slip was present over two years ago.
M23, Junction 9 Gatwick Link	Embankment	16	ii.1		No information

Table A1.2: Known embankment failures in UK highway network-Area 3 during the winter of 2000/2001 (a summary based on Perry's survey report, 2001)

Appendix 2: List of recent railway landslides in press

Appendix 2

- Landslip near Petersfield (27 Dec 2013)

A severe landslide happened between Liss and Liphook and affected train services travelling between Petersfield and Haslemere in Surrey.



Source: <http://www.portsmouth.co.uk/news/local/landslip-near-petersfield-sparks-train-line-closure-1-5774019>

- Colliery landslip (13 Feb 2013)

An active landslide occurred at Hatfield Colliery at Stainforth on 13 February 2013, lifting a section of railway track. The damage was caused by a large spoil heap.



Source: <https://www.networkrailmediacentre.co.uk/News-Releases/Rail-repair-at-Hatfield-Stainforth-1db2.aspx>

- Landslip at Buxworth (5 Feb 2011)

Heavy rain caused a large section of the railway embankment above New Road, Buxworth to slide away and onto the road.



Sources: <http://www.networkrailmediacentre.co.uk/Gallery/Buxworth-landslip-05-Feb-2011-10a4.aspx>; and <http://www.whaleybridge.net/forum/default.aspx?g=posts&t=826>

- Gloucestershire Warwickshire Railway landslides

Chicken Curve collapse, Winchcombe embankment (19 Jan 2011)

A major embankment collapse occurred on the Toddington side of Winchcombe station. Continuous movement of the embankment damaged the culverts that run beneath it, allowing water go soak into the embankment core. Remedial work was carried out but the embankment failed completely.



Source: <http://www.gwsr.com/news/2011/january/chicken-curve-stuffed!.aspx>

Gotherington embankment slip (April – August 2010)

A landslip of an embankment occurred near Gotherington. Minor movement was first noticed during a routine safety inspection in late April 2010 and after two days of monitoring the line was closed as conditions deteriorated. By August there was a drop of over a metre clear under the bottom of the track panels over a 15m length with a further 10 m half supported.



Source: <http://www.gwsr.com/about-us/history/gotherington-slip.aspx>

- Landslide between Glasgow and Inverclyde (14 Jan 2011)

A landslide happened on the railway line between Glasgow and Inverclyde on 14 January 2011. A part of a wall fell on to the line between Langbank and Bishopton.

Source: <http://www.greenocktelegraph.co.uk/news/gourock/articles/2011/01/14/409197-landslide-hits-railway-line/>

- Landslides due to storms at Cornwall (17 Nov 2010)

A landslide on the Newquay branch line during flash floods severed all rail links to the town for up to a month. The severe weather caused mud slides at three locations in the Pontsmill area, creating thousands of tonnes of debris.



Source: Richard Clinnick' report (p68-69) in Railmagazine 660, Dec 2010 – Jan 2011,

- Landslide at Upwey, near Weymouth (1 Dec 2009)

Two landslips on a Dorset railway line within three days disrupted train services. On 28 Nov 2009, a passenger train from London Waterloo to Yeovil Junction line was derailed near Gillingham after a landslide pushed a tree on to the track. About 40 tonnes of debris was washed down onto the track from the cutting because of the bad weather. The second landslide, at Upwey, near Weymouth, happened on 1 Dec 2009.

Source: <http://news.bbc.co.uk/1/hi/england/dorset/8389638.stm>

- Harwich Branch Line (23 Oct 2009)

A landslide occurred near Harwich, one mile east of Wrabness station. Network Rail had been monitoring the embankment in the area using electronic sensors following recent earth movements. The landslide caused the track and overhead power lines to move from their normal position.

Source: <http://www.networkrailmediacentre.co.uk/content/Detail.aspx?ReleaseID=4754&NewsAreaID=2>

- Landslide near Westbury (26 Jan 2009)

A landslide occurred near Westbury and affected train services travelling from Paddington to Exeter St. Davids. The landslide was caused by poor weather conditions in the past few days, when heavy rainfall saturated the embankment.

Source: <http://www.networkrailmediacentre.co.uk/content/detail.aspx?releaseid=4116&newsareaid=2>

- Landslide near Pennines (27 Oct 2008)

A double landslide closed a busy commuter train line through the Pennines. Heavy rain caused mud slips between Sheffield and Stockport.

Source: http://news.bbc.co.uk/1/hi/england/south_yorkshire/7693533.stm

- Landslide closed London-Wales railway (24 Jan 2008)

A landslide blocked the main railway line between London and south Wales. The landslip happened at the Old Sodbury tunnel, near Chipping Sodbury. It was thought the landslide was caused by a build-up of water levels due to wet weather in the area.



Source: <http://www.guardian.co.uk/uk/2008/jan/24/transport.world>

- Landslip at Elland in Yorkshire (21 Jan 2008)

A landslip was recorded at Elland on the Hebden Bridge to Wakefield railway line on 21 January 2008. Around 40 tonnes of trees and earth slipped down the bank following torrential rain.



Source: <http://www.networkrailmediacentre.co.uk/content/detail.aspx?releaseid=3735&newsareaid=2>

References

- Abellán, A., Jaboyedoff, M., Oppikofer, T., and Vilaplana, J. M., 2009. Detection of millimetric deformation using a terrestrial laser scanner: experiment and application to a rockfall event. *Natural Hazards and Earth System Sciences*, 9, 365-372.
- Abellán, A., Calvet, J., Vilaplana, J. and Blanchard, J., 2010. Detection and spatial prediction of rockfalls by means of terrestrial laser scanner monitoring. *Geomorphology*, 119, 162-171.
- Aguilar, F.J., Agüera, F., Aguilar, M.A. and Carvajal F., 2005. Effects of terrain morphology, sampling density, and interpolation methods on grid DEM accuracy. *Photogrammetric Engineering & Remote Sensing*, 71(7), 805-816.
- Aguilar, F.J., Aguilar, M.A., Agüera, F. and Sánchez, J., 2006. The accuracy of grid digital elevation models linearly constructed from scattered sample data. *International Journal of Geographical Information Science*, 20(2), 169-192.
- Atkinson, P.M. and Foody, G.M., 2002. Uncertainty in Remote Sensing and GIS: Fundamentals, Chapter 1 of "Uncertainty in Remote Sensing and GIS", edited by Foody, G.M. and Atkinson, P. M., published by Wiley, England.
- Axelsson, P.E., 1999. Processing of laser scanner data - algorithms and applications. *ISPRS Journal of Photogrammetry and Remote Sensing*, 54(2-3), 138-147.
- Baltsavias, E.P., 1999. Airborne laser scanning: basic relations and formulas. *ISPRS Journal of Photogrammetry and Remote Sensing*, 54, 199-214.
- Barbarella, M. and Fiani, M., 2013. Monitoring of large landslides by terrestrial laser scanning techniques: field data collection and processing. *European Journal of Remote Sensing*, 46, 126-151.
- Barnhart, T.B. and Crosby, B.T., 2013. Comparing two methods of surface change detection on an evolving thermokarst using high-temporal-frequency terrestrial laser scanning, Selawik river, Alaska. *Remote Sensing*, 5(6), 2813-2837
- Bater, C.W. and Coops, N.C., 2009. Evaluating error associated with lidar-derived DEM interpolation. *Computers and Geosciences*, 35, 289-300.
- Beraldin, J.A., Blais, F. and Lohr, U., 2010. Laser scanning technology (Chapter 1), in *Airborne and Terrestrial Laser Scanning*, edited by Vosselman, G. and Maas, H.G., Whittles Publishing, ISBN (190444587X).
- Besl, P.J. and McKay, H.D., 1992. A method for registration of 3-D shapes. *IEEE Transactions on Pattern Analysis and Machine Intelligence*, 14(2), 239-256
- Birch, G.P. and Dewar, A.L., 2002. Earthwork failures in response to extreme weather. In, *Proceedings of the international conference railway engineering 2002*, London, UK.
- Birch, G. and Warren, C., 2006. Technical developments in the monitoring of the Folkestone Warren landslide complex. IAEG 2006, paper no.78, the Geological Society of London.
- Birch, G. and Anderson, I., 2011. LiDAR monitoring for the Folkestone Warren landslide. *Ground Engineering*, May 2011, 26-29
- Boehler, W., Vicent, M.B. and Marbs, A., 2003. Investigating laser scanner accuracy. In, *The International Archives of the Photogrammetry, Remote Sensing and Spatial Information Sciences*, 34(5), 696-701, presented in the XIXth CIPA Symposium at Antalya, Turkey.
- Brasington, J., Langham, J. and Rumsby, B., 2003. Methodological sensitivity of morphometric estimates of coarse fluvial sediment transport. *Geomorphology*, 53(3-4), 299-316.
- British Geological Survey, 2012. Increased incidence of landslides in 2012 [online] <http://www.bgs.ac.uk/science/landUseAndDevelopment/landslides/November2012.html> [accessed 10 July 2013]

References

- Brunori, C.A., Civico, R., Cinti, F.R. and Ventura, G., 2013. Characterization of active fault scarps from LiDAR data: a case study from Central Apennines (Italy). *International Journal of Geographical Information Science*, 27(7), 1405-1416.
- Buckley, S.J., Howell, J.A., Enge, H.D. and Kurz, T.H., 2008. Terrestrial laser scanning in geology: data acquisition, processing and accuracy considerations. *Journal of the Geological Society*, 165(3), 625–638.
- Carder, D.R. and Barker, K.J. 2005. The performance of a single row of spaced bored piles to stabilise a Gault clay slope on the M25. TRL report TRL627. Crowthorne: TRL Limited.
- Centeno, J.A.S., Wutke, J.D., Mitishita, E.A. and Vögtle, T., 2010. Two methods to estimate the spot size of terrestrial laser scanners. *Journal of Surveying Engineering*, 136(3), 126–131.
- Chen, Y., and Medioni, G., 1992. Object modelling by registration of multiple range images. *Image and Vision Computing*, 10(3), 145-155.
- Chen, Y.M. and Zhou, Q.M., 2013. A scale-adaptive DEM for multi-scale terrain analysis, *International Journal of Geographical Information Science*, 27(7), 1329-1348.
- Ciddor, P.E, 1996. Refractive index of air: new equations for the visible and near infrared. *Applied Optics*, 35(9), 1566 – 1573.
- Cooper, M.R., Bromhead, E.N., Petley, D.J., and Grant, D.I., 1998. The Selborne cutting stability experiment. *Géotechnique*, 48, 83–101.
- Coveney, S. and Fotheringham, A.S., 2011. Terrestrial laser scan error in the presence of dense ground vegetation. *The Photogrammetric Record*, 26(135), 307–324.
- Cox, M.G. and Harris, P.M., 2006. Software support for metrology best practice guide no. 6: uncertainty evaluation. National Physical Laboratory UK.
- Davis, J.P., Loveridge, F.A., Perry, J., Patterson, D. and Carder, D., 2003. Stabilization of a landslide on the M25 highway, London's main artery. 12th Pan-American Conference on Soil Mechanics and Geotechnical Engineering, Massachusetts Institute of Technology, Boston, 2003.
- Day, S.S., Gran, K.B., Belmont, P. and Wawrzyniec, T., 2013. Measuring bluff erosion part 1: terrestrial laser scanning methods for change detection. *Earth Surface Processes and Landforms*, 38, 1055–1067.
- Desmet, P.J.J., 1997. Effects of interpolation errors on the analysis of DEMs. *Earth Surface Processes and Landforms*, 22, 563-580.
- Ellis, E.A., and O'Brien, A.S., 2007. Effect of height on delayed collapse of cuttings in stiff clay. *Proceedings of the Institution of Civil Engineers Geotechnical Engineering* 160, issue GE2, 73-84.
- Erdogan, S., 2009. A comparison of interpolation methods for producing digital elevation models at the field scale. *Earth Surface Process and Landforms*, 34, 366 – 376.
- Errington, A.F.C., Daku, B.L.F. and Prugger, A.F., 2011. A model based approach to intensity normalization for terrestrial laser scanners. In, *Proceedings of International Symposium on Lidar and Radar Mapping 2011: Technologies and Applications*, edited by He, X.F., Xu, J. and Ferreira, V.G.
- Fisher, P.F. and Tate, N.J., 2006. Causes and consequences of error in digital elevation models. *Progress in physical geography*, 30(4), 467-489.
- Fonstad, M.A., Dietrich, J.T., Courville, B.C., Jensen, J.L. and Carbonneau, P.E., 2013. Topographic structure from motion: a new development in photogrammetric measurement. *Earth Surface Processes and Landforms*, 38, 421–430.
- Fukuzono, T., 1985. A new method for predicting the failure time of a slope. In, *Proceedings of the 4th International Conference and Field Workshop on Landslides*, Tokyo. Tokyo University Press, 145-150.

- Gallay, M., Lloyd, C.D., McKinley, J. and Barry, L., 2013. Assessing modern ground survey methods and airborne laser scanning for digital terrain modelling: a case study from the Lake District, England. *Computers & Geosciences*, 51, 216-227.
- Gessesse, G.D., Fuchs, H., Mansberger, R., Klik, A. and Rieke-Zapp, D.H., 2010. Assessment of erosion, deposition and rill development on irregular soil surfaces using close range digital photogrammetry. *The Photogrammetric Record*, 25, 299–318.
- Girardeau-Montaut, D., Roux, M., Marc, R. and Thibault, G., 2005. Change detection on point cloud data acquired with a ground laser scanner. *ISPRS Archives*, Volume XXXVI-3/W19, 30-35, presented in *ISPRS Workshop: Laser scanning 2005*, Enschede, Netherlands, 12-14 September, 2005.
- Ground Engineering, 1996. In the limelight. *Ground Engineering*, June 1996, 26–27, Thomas Telford, London.
- Gruen, A. and Akca, D., 2005. Least squares 3D surface and curve matching. *ISPRS Journal of Photogrammetry and Remote Sensing*, 59(3), 151-174.
- Guarnieri, A., Vettore, A., Pirotti, F., Menenti, M. and Marani, M., 2009. Retrieval of small-relief marsh morphology from Terrestrial Laser Scanner, optimal spatial filtering, and laser return intensity. *Geomorphology*, 113, 12-20.
- Hancock, J.A., 1999. Laser Intensity-based obstacle detection and tracking. Doctoral thesis, No. CMU-RI-TR-99-01, The Robotics Institute, Carnegie Mellon University.
- Hall, S.A., Burke, I.C., Box, D.O., Kaufmann, M.R. and Stoker, J.M., 2005. Estimating stand structure using discrete-return lidar: an example from low density, fire prone ponderosa pine forests. *Forest Ecology and Management*, 208 (1-3), 189–209.
- Hebert, M. and Krotkov, E., 1992. 3D measurements from imaging laser radars: how good are they? *Image and Vision Computing*, 10(3), 170-178.
- Heritage, G.L., Milan, D.J., Large, A.R.G. and Fuller, I.C., 2009. Influence of survey strategy and interpolation model on DEM quality. *Geomorphology*, 112(3-4), 334-344.
- Highways Agency, 1993. HA 48/93: Geotechnics and drainage Part 3: Earthworks. Maintenance of highway earthworks and drainage, Design Manual for Roads and Bridges, Highways Agency, UK.
- Hodge, R.A., 2010. Using simulated terrestrial laser scanning to analyse errors in high-resolution scan data of irregular surfaces. *ISPRS Journal of Photogrammetry and Remote Sensing*, 65(2), 227-240.
- Hodgson, M.E. and Bresnahan, P., 2004. Accuracy of airborne lidar-derived elevation: empirical assessment and error budget. *Photogrammetric Engineering & Remote sensing*, 70(3), 331– 340.
- Hofle, B. and Pfeifer, N., 2007. Correction of laser scanning intensity data: data and model-driven approaches. *ISPRS Journal of Photogrammetry and Remote Sensing*, 62(6), 415–433.
- Hopkinson, C., Chasmer, L.E., Sass, G., Creed, I.F., Sitar, M., Kalbfleisch, W. and Treitz, P., 2005. Vegetation class dependent errors in lidar ground elevation and canopy height estimates in a boreal wetland environment. *Canadian Journal of Remote Sensing*, 31(2), 191–206.
- Hu, P., Liu, X.H. and Hu, H., 2009. Accuracy assessment of digital elevation models based on approximation theory. *Photogrammetric Engineering & Remote Sensing*, 75(1), 49–56.
- Huang, Y.D., 2000. Evaluation of information loss in digital elevation models with digital photogrammetric systems. *Photogrammetric Record*, 16(95), 781-791.
- Hughes, D., Sivakumar, V., Glynn, D. and Clarke, G., 2007. A case study: delayed failure of a deep cutting in lodgement till. *Proceedings of the Institution of Civil Engineers Geotechnical Engineering*, 160, issue GE4, 193-202.

References

- Hunter, G.J. and Goodchild, M.F., 1997. Modelling the uncertainty of slope and aspect estimates derived from spatial databases. *Geographical Analysis*, 29, 35-49.
- Hunter, G.J., 2003. The pre- and post-failure deformation behaviour of soil slopes. PhD thesis, The University of New South Wales.
- Jacobs, G., 2006. Understanding spot size for laser scanning. *Professional Surveyor Magazine*, Issue October 2006.
- Jaboyedoff, M., Demers, D., Locat, J., Locat, A., Locat, P., Oppikofer, T., Robitaille, D. and Turmel, D., 2009. Use of terrestrial laser scanning for the characterization of retrogressive landslides in sensitive clay and rotational landslides in river banks. *Canadian Geotechnical Journal*, 46(12), 1379-1390.
- Jelalian, A.V., 1992. *Laser Radar Systems*. Artech House, Boston – London.
- Jutzi, B. and Gross, H., 2009. Normalization of LiDAR intensity data based on range and surface incidence angle. *ISPRS Archives*, Volume XXXVIII-3/W8, 213-218, presented in *ISPRS Workshop: Laser scanning 2009*, Paris, France.
- Kaasalainen, S., Ahokas, E., Hyypä, J., and Suomalainen, J., 2005. Study of surface brightness from backscattered laser intensity: calibration of laser data. *IEEE Geoscience and Remote Sensing Letters*, 2(3), 255–259.
- Kaasalainen, S., Krooks, A., Kukko, A. and Kaartinen, H., 2009. Radiometric calibration of terrestrial laser scanners with external reference targets. *Remote Sensors*, 1(3), 144-158.
- Kersten, T.P., Mechelke, K., Lindstaedt, M. and Sternberg, H., 2008. Geometric accuracy investigations of the latest terrestrial laser scanning systems. *FIG Working Week 2008*, Stockholm, Sweden, 14-19 June 2008
- Kovacevic, K., Potts, D.M. and Vaughan, P.R., 2001. Progressive failure in clay embankments due to seasonal climate changes. In, *Proceedings of the 5th International Conference on Soil Mechanics and Geotechnical Engineering*, Istanbul, 2127-2130
- Kraus, K. and Pfeifer, N., 1998. Determination of terrain models in wooded areas with airborne laser scanner data. *ISPRS Journal of Photogrammetry and Remote Sensing*, 53(4), 193-203.
- Kyriakidis, P.C., Shortridge, A.M., and Goodchild, M.F., 1999. Geostatistics for conflation and accuracy assessment of digital elevation models. *International Journal of Geographical Information Science*, 13(7), 677-707.
- Kyriakidis P.C. and Goodchild M.F., 2006. On the prediction error variance of three common spatial interpolation schemes. *International Journal of Geographical Information Science*, 20(8), 823-855.
- Lague, D., Brodu, N. and Leroux, J., 2013. Accurate 3D comparison of complex topography with terrestrial laser scanner: application to the Rangitikei canyon (N-Z). *ISPRS Journal of Photogrammetry and Remote Sensing*, 82, 10-26.
- Latypov, D., 2002. Estimating relative lidar accuracy information from overlapping flight lines. *ISPRS Journal of Photogrammetry & Remote Sensing*, 56 (4), 236–245.
- Leica Geosystems, 2012a, *Leica ScanStation C10/C5 system field manual*, Version 5.0., Leica Geosystems AG, Switzerland.
- Leica Geosystems, 2012b. *Leica ScanStation C10 Product Specifications* [online], Leica Geosystems AG, Switzerland. http://www.leica-geosystems.co.uk/downloads/123/hds/hds/ScanStation%20C10/brochures-datasheet/Leica_ScanStation_C10_DS_en.pdf [Accessed 16 Oct 2013]
- Leica Geosystems, 2013. *Leica HDS8810 datasheet* [online]: http://www.leica-geosystems.co.uk/downloads/123/zz/hds/HDS8800/brochures/HDS8800_BRO_en.pdf [Accessed 23 Sep 2013].
- Leroueil, S., Vaunat, J., Picarelli, L., Locat, J., Faure, R. and Lee, H., 1996. A geotechnical

- characterization of slope movements. In, Proceedings of the 7th International Symposium on Landslides, Trondheim 1, 53-74, Balkema, Rotterdam.
- Leroueil, S., 2001. Natural slopes and cuts: movement and failure mechanisms. *Géotechnique*, 51(3), 197-243
- Li, Z.L., 1988. On the measure of digital terrain model accuracy. *Photogrammetric Record*, 12, 873-877
- Li, Z.L., 1993. Mathematical models of the accuracy of digital terrain model surfaces linearly constructed from square gridded data. *Photogrammetric Record*, 14(82), 661-674.
- Lichti, D.D. and Franke, J., 2005a. Self-calibration of the iQsun 880 laser scanner. In: Gruen, A., Kahmen, H. (Eds.), *Optical 3-D Measurement Techniques VII*, vol. I, Vienna, Austria, 3-5 October, 112-122.
- Lichti, D.D., Gordon, S., and Tipdecho, T., 2005b. Error models and propagation in directly georeferenced terrestrial laser scanner networks. *Journal of Surveying Engineering*, 131(4), 135-142.
- Lichti, D.D. and Licht, M.G., 2006. Experiences with terrestrial laser scanner modeling and accuracy assessment. *ISPRS Archives*, Volume XXXVI Part 5, 155-160, presented in the *ISPRS Commission V Symposium: 'Image Engineering and Vision Metrology'*, Dresden Germany, 25-27 September, 2006.
- Lichti, D.D., 2007. Error modelling, calibration and analysis of an AM-CW terrestrial laser scanner system. *ISPRS Journal of Photogrammetry and Remote Sensing*, 61 (5), 307-324.
- Lichti, D.D., 2008. A method to test differences between additional parameter sets with a case study in terrestrial laser scanner self-calibration stability analysis. *ISPRS Journal of Photogrammetry and Remote Sensing*, 63 (2), 169-180.
- Lichti, D.D., 2010. Terrestrial laser scanner self-calibration: correlation sources and their mitigation. *ISPRS Journal of Photogrammetry and Remote Sensing*, 65 (1), 93-102
- Lim, K., Treitz, P., Wulder, M., St-Onge, B. and Flood, M., 2003. LiDAR remote sensing of forest structure. *Progress in Physical Geography*, 27(1), 88-106.
- Lloyd, C.D. and Atkinson, P.M., 2002. Non-stationary approaches for mapping terrain and assessing prediction uncertainty. *Transactions in GIS*, 6(1) 17-30.
- Lloyd, C.D. and Atkinson, P.M., 2006. Deriving ground surface digital elevation models from LiDAR data with geostatistics. *International Journal of Geographical Information Science*, 20(5), 535-563.
- Määttä, K., Kostamovaara, J. and Myllylä, R., 1993. Profiling of hot surfaces by pulsed time-of-flight laser range finder techniques. *Applied Optics*, 32(27), 5324 - 5347.
- Mallet, C. and Bretar, F., 2009. Full-waveform topographic lidar: state-of-the-art. *ISPRS Journal of Photogrammetry and Remote Sensing*, 64, 1-16.
- Miller, P.E., Mills, J.P., Edwards, S., Bryan, P., Marsh, S., Mitchell, H. and Hobbs, P., 2008a. A robust surface matching technique for coastal geohazard assessment and management. *ISPRS Journal of Photogrammetry and Remote Sensing*, 63(5), 529-542.
- Miller, P.E., Mills, J.P., Barr, S.L., Lim, M., Barber, D., Parkin, G., Clarke, B., Glendinning, S. and Hall, J., 2008b. Terrestrial laser scanning for assessing the risk of slope instability along transport corridors. *ISPRS Archives*, Volume XXXVII Part B5, 495-500, presented in the *XXIst ISPRS Congress: Commission V, WG 3*, Beijing, China, 2008.
- Mohamed, A. and Wikinson, B., 2009. Direct georeferencing of stationary LiDAR. *Remote Sensing*, 1, 1321-1337.
- Montreuil, A.L., Bullard, J.E., Chandler, J.H. and Millett, J., 2013. Decadal and seasonal development of embryo dunes on an accreting macrotidal beach: North Lincolnshire, UK. *Earth Surface Processes and Landforms*, 38(15), 1851-1868.

References

- Negishi, J.N., Sagawa, S., Sanada, S., Kume, M., Ohmori, T., Miyashita, T. and Kayaba, Y., 2012. Using airborne scanning laser altimetry (LiDAR) to estimate surface connectivity of floodplain water bodies. *River Research and Applications*, 28, 258–267.
- Nield, J.M., Wiggs, G.F.S. and Squirrell, R.S., 2011. Aeolian sand strip mobility and protodune development on a drying beach: examining surface moisture and surface roughness patterns measured by terrestrial laser scanning. *Earth Surface Processes and Landforms*, 36(4), 513–522.
- Oksanen, J. and Sarjakoski, T., 2005. Error propagation of DEM-based surface derivatives. *Computers and Geosciences*, 31, 1015-1027.
- Olsen, M.J. and Stuedlein, A.W., 2010. Discussion of “Use of terrestrial laser scanning for the characterization of retrogressive landslides in sensitive clay and rotational landslides in river banks”. *Canadian Geotechnical Journal*, 47, 1164-1168.
- Olsen, M.J., Kuester, F., Chang, B.J. and Hutchinson, T.C., 2010. Terrestrial laser scanning-based structural damage assessment. *Journal of Computing in Civil Engineering*, 24, 264–272.
- Páquet, R., 2010. Estimation of interpolation error in DEMs using statistical methods. FIG Congress 2010: Facing the challenges – building the capacity, Sydney, Australia.
- Petley, D.N., Bulmer, M.H. and Murphy, W., 2002. Patterns of movement in rotational and translational landslides. *Geology*, 30(8), 719-722.
- Petley, D.N., 2004. The evolution of slope failures: mechanisms of rupture propagation. *Natural Hazards and Earth System Sciences*, 4, 147–152.
- Perry, J., 1989. A survey of slope condition on motorway earthworks in England and Wales. Research Report 199. Crowthorne: TRL Limited.
- Perry, J., Pedley, M. and Reid, M., 2009. CIRIA Report C592: Infrastructure embankments - condition appraisal and remedial treatment.
- Perry, J., 2001. Slope failure reports prepared by Perry for Highways Agency. Source: HA GDMS Geotechnical Data Management System: <http://www.hagdms.com/> [downloaded in 2011].
- Pfeifer, N., Stadler, P. and Briese, C., 2001. Derivation of digital terrain models in the SCOP++ environment. In, Proceedings of OEEPE Workshop on Airborne Laser Scanning and Interferometric SAR for Digital Elevation Models, Stockholm, Sweden, 2001
- Pfeifer, N., Gorte, B. and Vosselman, G., 2003. Laser altimetry and vegetation. Technical Report AGI-GAP-2003-56, Adviesdienst Geo-Informatie en ICT, Rijkswaterstaat, The Netherlands.
- Pfeifer, N., Gorte, B. and Elberink, E.O., 2004. Influences of vegetation on laser altimetry – analysis and correction approaches. In, the International Archives of Photogrammetry and Remote Sensing, Vol. XXXVI, 8/W2, Freiburg, Germany.
- Pfeifer, N., Dorninger, P., Haring, A. and Fan, H., 2007. Investigating terrestrial laser scanning intensity data: quality and functional relations. In, Proceedings of VIII conference on Optical 3D measurement techniques, ETH Zurich, Switzerland , 328–337.
- Pfeifer, N., Hofle, B., Briese, C., Rutzinger, M. and Haring, A., 2008. Analysis of the Backscattered Energy in Terrestrial Laser Scanning Data. In, The International Archives of the Photogrammetry, Remote Sensing and Spatial Information Sciences, Volume XXXVII, Part B5, 1045–1051.
- Potts, D.M., Kovacevic, N. and Vaughan, P.R., 1997. Delayed collapse of slopes in stiff clay. *Géotechnique*, 47(5), 953–982.
- Potts, D.M., Kovacevic, N. and Vaughan, P.R., 2000. Delayed collapse of cut slopes in stiff clay. *Géotechnique*, 50(2), 203–205.

- Prokop, A. and Panholzer, H., 2009. Assessing the capability of terrestrial laser scanning for monitoring slow moving landslides. *Natural Hazards and Earth System Sciences*, 9, 1921–1928
- Ready, J.F., 1978. *Industrial applications of lasers*. Academic Press, New York – San Francisco – London.
- Reshetyuk, Y., 2006. Calibration of terrestrial laser scanners for the purpose of geodetic engineering. 3rd IAG / 12th FIG Symposium, Baden, May 22-24, 2006
- Reshetyuk, Y., 2009. Self-calibration and direct georeferencing in terrestrial laser scanning. Doctoral thesis in Infrastructure, Geodesy Royal Institute of Technology, Stockholm, Sweden; TRITA-TEC-PHD 09–005; ISBN (978–91–85539–34–5).
- Reshetyuk, Y., 2010a. A unified approach to self-calibration of terrestrial laser scanners. *ISPRS Journal of Photogrammetry and Remote Sensing*, 65, 445–456.
- Reshetyuk, Y., 2010b. Direct georeferencing with GPS in terrestrial laser scanning. *zfv*, 151-159
- Ridley, A., McGinnity, B. and Vaughan, P., 2004. Role of pore water pressures in embankment stability. *Proceedings of the Institution of Civil Engineers Geotechnical Engineering*, 157(4), 193–198.
- RIEGEL, 2013. RIEGEL VZ-6000 datasheet [online]: http://www.riegl.com/uploads/tx_pxprigldownloads/DataSheet_VZ-6000_23-09-2013_PRELIMINARY.pdf [Accessed 23 Sep 2013].
- Rosser, N.J., Petley, D.N., Lim, M., Dunning, S.A., and Allison, R.J., 2005. Terrestrial laser scanning for monitoring the process of hard rock coastal cliff erosion, *Quarterly Journal of Engineering Geology and Hydrogeology*, 38(4), 363–375.
- Rüeger, J.M., 1996. *Electronic distance measurement - an introduction*, reprint of the original (4th edition), Springer Verlag Berlin Heideberg.
- Rumsby, B.T., Brasington, J., Langham, J.A., McLelland, S.J., Middleton, R. and Rollinson, G., 2008. Monitoring and modelling particle and reach-scale morphological change in gravel-bed rivers: applications and challenges. *Geomorphology*, 93, 40–54
- Saito, M., 1965. Forecasting the time of occurrence of slope failure. In, *Proceedings of the 6th International Conference on Soil Mechanics and Foundation Engineering*, Montréal, Que., University of Toronto Press, Toronto, Ont. Vol. 2, 537-542.
- Scaioni, M., 2004. Direct georeferencing of TLS in surveying of complex sites. In, *Proceedings of 3D-ARCH, Virtual Reconstruction and Visualization of Complex Architectures*, International Society of Photogrammetry and Remote Sensing (ISPRS), Mestre-Venice, Italy.
- Schäfer, T., Weber, T., Kyrinovič P. and Zámečnicková M., 2004. Deformation measurement using terrestrial laser scanning at the hydropower station of Gabčíkovo. In, *Proceedings of INGEO 2004 and FIG Regional Central and Eastern European Conference on Engineering Surveying*, Bratislava, Slovakia, November 11-13, 2004
- Schürch, P., Densmore, A.L., Rosser, N.J., Lim, M. and McArdell, B.W., 2011. Detection of surface change in complex topography using terrestrial laser scanning: application to the Illgraben debris-flow channel. *Earth Surface Processes and Landforms*, 36(14), 1847–1859.
- Schofield, W. and Breach, M., 2007. *Engineering Surveying (the sixth edition)*, published by Butterworth-Heinemann (an imprint of Elsevier), Linacre House, Jordan Hill, Oxford, UK.
- Schulz, T., 2007. Calibration of a terrestrial laser scanner for engineering geodesy. Doctoral thesis to ETH Zurich, DISS.ETH NO. 17036.
- Scott, J., Loveridge, F. and O'Brien A.S., 2007. Influence of climate and vegetation on railway embankments. In, *Proceedings of the 14th European Conference on Soil Mechanics and*

References

- Geotechnical Engineering (Madrid), Vol. 2, 659-664
- Shi, W.Z., Li, Q.Q. and Zhu, C.Q., 2005. Estimating the propagation error of DEM from higher-order interpolation algorithms. *International Journal of Remote Sensing*, 26(14), 3069-3084.
- Shortridge, A., 2001. Characterizing uncertainty in digital elevation models. In Hunsaker, C.T., Goodchild, M.F., Friedl, M.F. and Case, T.J., editors, *Spatial uncertainty in ecology: implications for remote sensing and GIS applications*, New York: Springer, 238–257.
- Sibson, R., 1981. A brief description of natural neighbour interpolation (Chapter 2). In V. Barnett. *Interpreting Multivariate Data*. Chichester: John Wiley. 21–36.
- Singh, A. and Mitchell, J.K., 1968. General stress-strain-time function for soil. *Journal of the Soil Mechanics and Foundations Division, ASCE*, Vol 94, (SM1), 21-46.
- Skempton, A.W., 1964. Long term stability of clay slopes. *Géotechnique*, 14, 77–101.
- Smethurst, J., Clarke, D. and Powrie, W., 2006. Seasonal changes in pore water pressure in a grass covered cut slope in London clay. *Géotechnique*, 56(8), 523-537
- Smethurst, J.A. and Powrie, W., 2007. Monitoring and analysis of the bending behaviour of discrete piles used to stabilise a railway embankment. *Geotechnique*, 57(8), 663–677.
- Smethurst, J., Clarke, D. and Powrie, W., 2012. Factors controlling the seasonal variation in soil water content and pore water pressures within a lightly vegetated clay slope. *Géotechnique*, 62(5), 429-446.
- Soudarissanane, S., Lindenbergh, R., Menenti, M. and Teunissen, P., 2011. Scanning geometry: influencing factor on the quality of terrestrial laser scanning points. *ISPRS Journal of Photogrammetry and Remote Sensing*, 66(4), 389-399.
- Spaete L.P., Glenn N.F., Derryberry D.R., Sankey T.T., Mitchell J.J. and Hardegree S.P., 2011. Vegetation and slope effects on accuracy of a LiDAR-derived DEM in the sagebrush steppe. *Remote Sensing Letters*, 2(4), 317-326.
- Su, J. and Bork, E., 2006. Influence of vegetation, slope and lidar sampling angle on DEM accuracy. *Photogrammetric Engineering & Remote Sensing*, 72(11), 1265-1274.
- Take, W.A. and Bolton, M.D., 2011. Seasonal retching and softening in clay slopes, leading to first-time failure. *Géotechnique*, 61(9), 757-769.
- Tang, P., Akinci, B. and Huber, D., 2009. Quantification of edge loss of laser scanned data at spatial discontinuities. *Automation in Construction*, 18, 1070-1083
- Taylor, J.R., 1982. *An introduction to error analysis: the study of uncertainties in physical measurements*, published by University Science Books.
- Terzaghi, K. and Peck, R.B., 1948. *Soil mechanics in engineering practice*, published by Wiley, New York.
- Teza, G., Galgaro, A., Zaltron, N. and Genevois, R., 2007. Terrestrial laser scanner to detect landslide displacement fields a new approach. *International Journal of Remote Sensing*, 28(16), 3425-3446.
- Töyrä, J., Pietroniro, A., Hopkinson, C. and Kalbfleisch, W., 2003. Assessment of airborne scanning laser altimetry (LiDAR) in a deltaic wetland environment. *Canadian Journal of Remote Sensing*, 29(6), 679-690.
- Vaughan, P.R. and Walbancke, H.J., 1973. Pore pressure changes and the delayed failure of cutting slopes in over-consolidated clay. *Géotechnique*, 23(4), 531-539
- Vežočnik, R., Ambrožič, T., Sterle, O., Bilban, G., Pfeifer, N. and Stopar, B., 2009. Use of terrestrial laser scanning technology for long term high precision deformation monitoring. *Sensors*, 9, 9873-9895.
- Voisin, S., Foufou, S., Truchetet, F., Page, D. and Abidi, M., 2007. Study of ambient light influence for three-dimensional scanners based on structured light. *Optical Engineering Letters*, 46 (3), 030502-1 – 030502-3.

- Wagner, W., Ullrich, A., Melzer, T., Briese, C. and Kraus K., 2004. From single-pulse to full-waveform airborne laser scanners: potential and practical challenges. ISPRS Archives, Volume XXXV Part B3, presented in the XXth ISPRS Congress, Technical Commission III, July 12-23, 2004, Istanbul, Turkey.
- Wang, C., Menenti, M., Stoll, M., Feola, A., Belluco, E. and Marani, M., 2009. Separation of ground and low vegetation signatures in LiDAR measurements of salt marsh environments. *IEEE Transactions on Geoscience and Remote Sensing*, 47 (7), 2014-2023.
- Wang, G., Philips, D., Joyce, J. and Rivera, F.O., 2011. The integration of TLS and continuous GPS to study landslide deformation: a case study in Puerto Rico. *Journal of Geodetic Science*, 1(1), 25-34.
- Webster, T.L., Forbes, D.L., MacKinnon, E. and Roberts, D., 2006. Flood-risk mapping for storm-surge events and sea-level rise using lidar for southeast New Brunswick. *Canadian Journal of Remote Sensing*, 32(2), 194-211.
- Wechsler, S.P. and Kroll C.N., 2006. Quantifying DEM uncertainty and its effect on topographic parameters. *Photogrammetric Engineering & Remote Sensing*, 72(9), 1081-1090.
- Wehr, A. and Lohr, U., 1999. Airborne laser scanning - an introduction and overview. *ISPRS Journal of Photogrammetry and Remote Sensing*, 54, 68-82
- Wheaton, J.M., Brasington, J., Darby, S.E. and Sear, D.A., 2010. Accounting for uncertainty in DEMs from repeat topographic surveys: improved sediment budgets. *Earth Surface Processes and Landforms*, 35, 136–156.
- Wieczorek, G.F., and Snyder, J.B., 2009. Monitoring slope movements, in Young, R., and Norby, L., *Geological Monitoring: Boulder, Colorado*, Geological Society of America, 245–271.
- Zhu, C., Shi, W., Li, Q., Wang, G., Cheung, T.C.K., Dai, E. and Shea, G.Y.K., 2005. Estimation of average DEM accuracy under linear interpolation considering random errors at the nodes of TIN model. *International Journal of Remote Sensing*, 26(24), 5509-5523.

Bibliography

(Bibliography that did not appear in the list of Reference is listed here)

- Arras, K.O., 1998. An introduction to error propagation: derivation, meaning and examples of equation. Technical report EPFL-ASL-TR-98-01(R3) of the Autonomous Systems Lab, Institute of Robotic Systems, Swiss Federal Institute of Technology Lausanne (EPFL).
- Bennett, J.M., 1992. Recent developments in surface roughness characterization. *Measurement Science and Technology*, 3(12), 1119-1127
- Bolton, M., 1979. *A Guide to Soil Mechanics*, first published by Macmillan Education Ltd.
- Bromhead, E.N., 1992. *The stability of slopes* (2nd edition), published by Taylor&Francis.
- Efron, B. and Tibshirani, R.J. 1993. *An introduction to the Bootstrap*. Published by Chapman & Hall, London.
- Hani, A.F.M., Sathyamoorthy, D. and Asirvadam, V.S., 2011. A method for computation of surface roughness of digital elevation model terrains via multiscale analysis. *Computers & Geosciences*, 37, 177-192.
- Heuvelink, G.B.M., 1998. *Error Propagation in Environmental Modelling with GIS*, published Taylor&Francis Ltd.
- Jaboyedoff, M., Oppikofer, T., Abellán, A., Derron, M.H., Loye, A., Metzger, R. and Pedrazzini, A., 2012. Use of LIDAR in landslide investigations: a review. *Natural Hazards*, 61(1), 5-28
- Jacobs, G., 2009. 3D scanning: accuracy of scan points. *Professional Surveyor Magazine*, Issue August 2009.
- Leica Geosystems, 2010. *HDS and Cyclone Traning Course Manual*.
- Li, Z.L., Zhu, Q. and Gold, C., 2005. *Digital Terrain Modelling Principles and Methodology*, publised by CRC Press.
- MathWorks, 2011. *MATLAB Fundamentals and Programming Techniques Training Manual*.
- Middleton, G.V., 2000. *Data Analysis in the Earth Sciences Using MATLAB®*, publised by Prentice-Hall, Inc.
- Perry, J., Pedley, M. and Reid, M., 2009. *CIRIA Report C591: Infrastructure Cuttings - condition appraisal and remedial treatment*.
- Powrie, W., 2004. *Soil Mechanics: Concepts & Applications* (2nd edition), published by Spon Press.
- Trauth., M.H., 2010. *MATLAB® Recipes for Earth Sciences* (3rd edition), publised by Springer.

Publications

Conference proceedings:

Fan, L., Smethurst, J.A., Powrie, W. and Sellaiya, A., 2014. Seasonal slope surface deformation measured with terrestrial laser scanning. IOP Conference Series: Earth and Environmental Science, 17, 012264, the 35th International Symposium on Remote Sensing of Environment, Beijing, China, 22 - 26 Apr 2013,

Journal articles:

Fan, L., Smethurst, J.A., Atkinson, P. and Powrie, W., 2014. Propagation of vertical and horizontal source data errors into a TIN with linear interpolation. International Journal of Geographical Information Science, 28(7), 1378-1400.

Fan, L., Powrie, W., Smethurst, J.A., Atkinson, P. and Einstein, H., 2014. The effect of short vegetation on terrestrial laser scans at a local scale. ISPRS Journal of Photogrammetry and Remote Sensing, 95, 42-52.